Study of the Origins of Toughness in Amorphous Metals

A Thesis by
Glenn Robert Garrett

In Partial Fulfillment of the Requirements for
the Degree of
Doctor of Philosophy

CALIFORNIA INSTITUTE OF TECHNOLOGY
Pasadena, California
2013
(Defended September 27, 2012)

To my loving family,

Ronald, Linda, Allison, Brad, Evan, Anna

ACKNOWLEDGEMENTS

I would like to thank Professor W. L. Johnson for accepting me as a graduate student at Caltech and giving me the opportunity to travel the winding path of research. The journey can often be confusing, and it is easy to get disoriented, but he was always there, a constant reminder that science is ultimately fun and the process of discovery should be enjoyed wholeheartedly. We are lucky to solve puzzles for a living. Take a stroll on the roof, the truth shall make you free. Yes, it can, it does, it will. However, the truth does not come easy. You have to hunt for it, with great skill and even greater persistence. For this truth, I must thank Dr. M. D. Demetriou. He has been an unparalleled motivator and a fantastic collaborator. I will always be indebted to him for the help and encouragement he has given me. I feel extremely lucky to have been advised by such a great team.

Next, I would like to thank Professor B. Fultz for encouraging me to attend Caltech and giving me great advice on navigating the first two years of graduate school. I also want to thank him for participating in both my candidacy and thesis committee. It was a pleasure to be his teaching assistant and even more fun to chat in the hallway. I also want to thank Professor G. Ravichandran for taking time out of his schedule to encourage me to attend Caltech, as well as participating in both my candidacy and thesis committee. He is also extremely kind to allow the Johnson group to use his lab, we are very grateful. I want to thank Professor W. A. Goddard III for a crash course in how to do the best science possible with computer simulations. His clarity, strategic thinking, and passion for science made the weekly meetings for cavitation research thrilling. I also want to thank him for participating on my thesis committee. I also want to thank Professor S. Haile for participating on my candidacy committee; her interesting questions and kindness that day are deeply appreciated. While Professor K. Samwer will not be able to make my thesis defense, I cannot blame him for it, it is my own fault for taking so long to graduate. I will consider him there in spirit (or maybe Skype). I want to thank him for all the enlightening, encouraging, and lively discussions during his work-cations at Caltech, both scientifically and personally.

I want to thank Jin-Yoo Suh for patiently getting me started on annealing and fracture toughness measurements. I also want to thank Dr. Mary Laura Lind for her friendship and indomitable spirit, as well as transferring her ultrasonic measurement knowledge to me. I must thank Joseph Schramm for being my long time officemate and a great friend. I especially appreciate his support through the fallow years, and am thrilled to have him here for the fertile ones. He also knew where everything was in lab. I could not have asked for a better follow-up officemate and collaborator than Dr. Jyong-Hun Na, his fantastic work, great knowledge, and kind words are especially appreciated. I also want to thank Georg Kaltenboeck for his friendship and all of his support and expertise whenever I was having trouble, not to mention the cookies. I want to express my gratitude to Qi An for all the hard work he did bringing the cavitation simulations to fruition. I am extremely grateful to him for breathing new life into a project that I thought was finished.

I want to acknowledge all of the fun conversations and assistance that I have enjoyed with Dr. Dale Conner and Pamela Albertson; they are a big part of the Johnson group and are greatly appreciated. I want to acknowledge my senior Johnson group collaborators, Dr. Douglas Hofmann, Scott Roberts, Xiao Liu, and Henry Kozachkov for their hard work and support in making this a great lab. I also want to mention just a few of the people that have made Keck Labs a fun place to work: Dr. Channing Ahn, B. Lohwangwatana, Aaron Wiest, Lisa Mauger, Hillary Smith, Matthew Lucas, Alexander Papandrew, Mike Vondrus, Allison Kunz, and Andrew Hoff.

I want to recognize the great contributions of Professor Robert Ritchie, Dr. Maximillien Launey, and Dr. Bernd Gludovatz on expanding the state of knowledge of fracture toughness in metallic glass. Their expertise on the subject is critical, and I am thankful to have them as collaborators. I also want to recognize the contributions of several people who helped me immensely, either through collaborations or advice: Jason Chen, Kaitlyn Fritz, Julie Monohan, Petros Arakelian, Rick Gerhart, Mike Roy, Dr. Chi Ma, Michael Floyd, and Chase Crewdson. I would also like to acknowledge my two most influential advisors at the Georgia Institute of Technology, Professor Naresh Thadhani and Professor Robert Speyer. Their encouragement and support at a crucial time in my academic development has brought me to where I am now, thank you.

Of course, none of this would have been possible without the love and support of my family. I love you all dearly and am eternally grateful for your wonderful support when I decided to move across the country. I have dedicated this thesis to you as a show of my appreciation. I promise I will have more time to visit after I graduate. I especially want to thank Oksana for her caring and support; our time together has been my happiest.

There are many wonderful people that I am lucky to have been part of my Caltech community. I attempt an incomplete list as a miniscule token of my appreciation: Andy Downard, Drew May, Justus Brevik, Vanessa Jönsson, John Delacruz, Anne Dekas, Ken Diest, Krista Langeland, Nick Heinz, Mike Shearn, Leslie O'Leary, Jane Khudyakov, Marcos Costa, Mary Louie, Elitza Tocheva, Liliya Kharevych, Morgan Putnam, Russ Ernst, Will Ford, Ronnie Bryan, Evans Boney, Agatha Hodsman, Drew Kennedy.

ABSTRACT

Amorphous metals that form fully glassy parts over a few millimeters in thickness are still relatively new materials. Their glassy structure gives them particularly high strengths, high yield strains, high hardness values, high resilience, and low damping losses, but this can also result in an extremely low tolerance to the presence of flaws in the material. Since this glassy structure lacks the ordered crystal structure, it also lacks the crystalline defect (dislocations) that provides the micromechanism of toughening and flaw insensitivity in conventional metals. Without a sufficient and reliable toughness that results in a large tolerance of damage in the material, metallic glasses will struggle to be adopted commercially. Here, we identify the origin of toughness in metallic glass as the competition between the intrinsic toughening mechanism of shear banding ahead of a crack and crack propagation by the cavitation of the liquid inside the shear bands. We present a detailed study over the first three chapters mainly focusing on the process of shear banding; its crucial role in giving rise to one of the most damage-tolerant materials known, its extreme sensitivity to the configurational state of a glass with moderate toughness, and how the configurational state can be changed with the addition of minor elements. The last chapter is a novel investigation into the cavitation barrier in glass-forming liquids, the competing process to shear banding. The combination of our results represents an increased understanding of the major influences on the fracture toughness of metallic glasses and thus provides a path for the improvement and development of tougher metallic glasses.

TABLE OF CONTENTS

LIST OF FIGURES AND TABLES

Chapter 2: An Exceptionally Damage Tolerant Glass

Chapter 3: Influence of Configurational Disorder on the Intrinsic Fracture Toughness of Metallic Glasses

Chapter 4: Effect of Microalloying on the Toughness of Metallic Glass

Chapter 5: Investigation of Cavitation in Glass-Forming Liquids

Appendix A: Debye-Grüneisen Thermal Expansion Effect of $Zr_{35}Ti_{30}Cu_{8.25}Be_{26.7}$

Appendix B: Bulk Modulus, Poisson Ratio, and
Fracture Toughness of $Zr_{35}Ti_{30}Cu_{8.25}Be_{26.75}$

Appendix C: Determination of Enthalpy Recovery by Differential
Scanning Calorimetry for $Zr_{35}Ti_{30}Cu_{8.25}Be_{26.75}$

Chapter 1

INTRODUCTION

When engineers choose materials and design components for bridges, airplanes, and other applications where human lives are at risk, they no longer use the static strength of the material as the sole criteria for safety. Advances in fracture mechanics have shown that the best way to ensure the safety of a critical component is to design around the damage tolerance (the combination of yield strength and fracture toughness) of the material. Materials in the real world will always contain some potential flaw or crack, introduced during processing, regular use, or even mishandling. The important question to ask of a material is how much stress can this material withstand before any potential flaws cause it to fail quickly and catastrophically. This idea is the essence of fracture toughness, the measurement of a material's resistance to fracture. For metallic glass, even with an impressive strength, a lack of confidence in its fracture toughness, it will prevent it from being used for any but the least strenuous of applications (e.g., as excellent soft magnets).

M. F. Ashby and A. L. Greer have assessed both the strengths and weaknesses of metallic glasses as structural materials [1]. Naturally, the lack of a crystalline structure and its associated defects, i.e., dislocations and grain boundaries, is the source of both the most interesting advantages (high strength, high yield strain, high elastic energy storage, low damping, soft-magnetic properties, forming of the supercooled liquid) and deeply consternating disadvantages (zero tensile ductility, toughness values that can be as low as 5 MPa·m$^{1/2}$ [2] and sometimes as high as 100 MPa·m$^{1/2}$ [3], plastic zone sizes that range from microns [2] to a millimeter [3], and sometimes severe annealing embrittlement [4]) when comparing metallic glass to conventional crystalline engineering metals [1]. Ashby and Greer correctly conclude that given the circumstances one must identify applications where the disadvantages of metallic glass can be marginalized and the strengths can be maximized. However, the fracture toughness is such a crucial parameter for the wider adoption of metallic glass that we seek to shed light on the origins of its fracture toughness and identify the salient properties that control this important material parameter.

Specifically, in chapter 2 we address the fundamental source of toughness and thus damage tolerance in metallic glass, the development of the plastic zone in front of the crack tip. We introduce a Pd-based glass of excellent damage tolerance and show that the competition between extensive shear band growth and crack propagation via cavitation in the shear band lies at the heart of fracture toughness. In chapter 3 we explore the variability in the as-cast state of a highly processable Zr-based glass, and demonstrate that the fracture process of a pre-cracked specimen is a local process that is sensitive to the local environment of the crack. We show how annealing reduces the variability in toughness, and that toughness can be increased by increasing the potential energy of the glass. In chapter 4 we investigate the effect of minor alloying additions (≤2%) on the configurational state and notch toughness of a Cu-based glass. In chapter 5 we present a study on the nucleation of cavities in glass-forming liquids due to the dynamic application of negative hydrostatic pressure. Glass-forming liquids are metastable to negative pressure on laboratory timescales, giving insight to the cavitation process that opposes shear band growth in metallic glass and thus plays an important role in limiting fracture toughness.

BIBLIOGRAPHY

[1] M. F. Ashby and A. L. Greer, Scripta Materialia **54**, 321 (2006).

[2] A. Shamimi Nouri, X. J. Gu, S. J. Poon, G. J. Shiflet, and J. J. Lewandowski, Philosophical Magazine Letters **88**, 853 (2008).

[3] J.Y. Suh, R. D. Conner, C. P. Kim, M. D. Demetriou, and W. L. Johnson, Journal of Materials Research **25**, 982 (2010).

[4] P. Murali and U. Ramamurty, Acta Materialia **53**, 1467 (2005).

Chapter 2

AN EXCEPTIONALLY DAMAGE-TOLERANT GLASS

ABSTRACT

Owing to a lack of microstructure, glassy materials are inherently strong but brittle, and often demonstrate extreme sensitivity to flaws. Accordingly, their macroscopic failure is often not initiated by plastic yielding, and almost always terminated by brittle fracture. Unlike conventional brittle glasses, metallic glasses are generally capable of limited plastic yielding by shear-band sliding in the vicinity of a flaw, and thus exhibit toughness–strength relationships that lie between brittle ceramics and marginally tough metals. Here, a bulk glassy Pd-alloy is introduced demonstrating an unusual capacity for shielding an opening crack accommodated by an extensive shear-band sliding process, which promotes a fracture toughness comparable to the toughest materials known. This result demonstrates that the combination of toughness and strength (i.e., damage tolerance) accessible to amorphous materials extends beyond the benchmark ranges established by the toughest and strongest materials known, thereby pushing the envelope of damage tolerance accessible to a structural metal.

INTRODUCTION

Crystalline materials exhibit ordered structures with morphological features (e.g., grains) that usually extend to the microscopic level. The defects associated with those microstructural features (e.g., dislocations) become mobile under stress, enabling extensive plastic shielding ahead of an opening crack, which promotes high fracture toughness. The elastic energy threshold for those defects to become active, however, is often low, resulting in rather low yield strengths. For example, ductile metals (e.g., low-carbon steels) have very high fracture toughness (>200 MPa·m$^{1/2}$), but fairly low plastic yield strength (<500 MPa). By contrast, a material with an amorphous atomic structure that lacks microstructural defects has the potential to yield plastically at much higher strengths. Because of the absence of those defects, however, the attainable plasticity ahead of an opening crack tip is limited, and consequently, an opening flaw is often accommodated by unstable crack propagation resulting in low fracture toughness. For example, oxide glasses such as silicates have very high estimated yield strengths (up to 3 GPa) but lack any substantial toughness (<1 MPa·m$^{1/2}$), and consequently, their failure is accommodated by brittle fracture occurring well below the theoretical yield strength (<100 MPa). In this regard, the properties of toughness and strength are invariably mutually exclusive in essentially all classes of materials [1]. This inherent trade-off between strength and toughness is the fundamental challenge in the quest for highly damage-tolerant materials [2]. To date, some success has been achieved through development of composite microstructures, which typically combine a strong glassy matrix with ductile crystalline reinforcements at structural length scales that suppress fracture while maintaining high strength [3]. Achieving combinations of strength and toughness that fall outside the benchmarks of traditional structural metals, however, remains an outstanding challenge. In this work, a monolithic metallic glass alloy is introduced demonstrating a level of damage tolerance previously inaccessible to the toughest and strongest engineering materials known.

Unlike brittle oxide glasses, metallic glasses are more likely to yield plastically under an opening stress. Consequently, most metallic glasses demonstrate substantial fracture toughness, and strengths consistent with the limit of elasticity of the amorphous structure (~2% of Young's modulus). Toughness–strength data reported to date for metallic glasses bridge the gap between brittle ceramics and marginally tough metals [4-6]. Specifically, reported fracture toughness values range from just over 1 $\text{MPa}\cdot\text{m}^{1/2}$ (for brittle rare-earth and ferrous metal glasses) [7,8] to about 100 $\text{MPa}\cdot\text{m}^{1/2}$ (for tougher noble and early-transition metal glasses) [9-11]. Reported strengths vary from about 0.5 GPa (for weak rare-earth metal glasses) [7] to as high as 5 GPa (for strong ferrous metal glasses) [12]. As demonstrated here, the toughness potentially accessible to an amorphous metal in fact extends much further, approaching values characteristic of the toughest materials known, while strengths consistent with the elasticity of the amorphous structure are retained.

Mechanistically, when an opening stress on the order of the material yield strength is applied, plastic shear sliding ensues confined within nanoscopic bands (shear bands) oriented along planes of maximum resolved shear stress. Such shear bands propagate by slip under negative pressure up to some critical shear strain, beyond which they open into emerging cracks. Under uniform negative pressure, as in quasi-static uniaxial tension, shear band opening in bulk samples becomes unstable and a crack propagates rapidly across the glassy structure resulting in essentially zero macroscopic plastic strain. In a quasi-stable loading geometry, however, as in bending, shear sliding initiated at the tensile surface can be arrested if propagated to the neutral axis without opening, such that stable plastic deformation can be achieved [13].

On the atomic scale, local shear sliding in the shear band is accommodated by cooperative inelastic rearrangements of local clusters of ~100 atoms [14]. Shearing can be sustained under negative pressure until low-density configurations develop and critical cavities eventually emerge. Upon the intervention of cavitation, plastic shearing is terminated and mechanical energy is dissipated via crack extension [15]. One can therefore expect that the extent to which a glass can undergo shear sliding under negative pressure prior to forming critical cavities should be proportional to its capacity to plastically shield an opening crack, and by extension, to its overall fracture toughness. It is therefore conceivable that very large fracture toughness values are theoretically possible for glasses with a capacity to undergo multiple configurational shear rearrangements prior to forming critical cavities, or equivalently, with activation barriers for shear flow much smaller than the activation barriers for cavitation. The glassy metal introduced here appears to exhibit such capacity, as it demonstrates an unusual propensity for shear flow without cavitation, which promotes very high fracture toughness.

GLASS DEVELOPMENT AND PROCESSING

Bulk-glass formation in Pd-rich metal/metalloid composition space was explored in the current work. The glass forming ability of Pd/metalloid systems was first recognized by Duwez *et al*. in 1965 [16]. Early Pd-rich metal/metalloid systems demonstrated only marginal glass-forming ability, but exhibited a very high Poisson's ratio (approaching 0.42) [17] together with a high glass-transition temperature (in excess of 600 K) [18]; high values for these two properties, as we argue later in the article, designate a high glass toughness. Indeed, a fairly robust fracture resistance was noted for those early marginal glass formers [19,20]. In the present study, Pd-rich metal/metalloid compositions were sought capable of forming bulk glasses while exhibiting Poisson ratios and glass-transition temperatures comparable to those of the early glass formers.

Pd-rich metal/metalloid alloys were prepared by inductively melting the pure elements in quartz tubes under an inert atmosphere. Alloy ingots were fluxed in quartz tubes with anhydrous B_2O_3 at ~1200 K for ~1000 s [21]. To form glassy samples, the fluxed ingots were melted in quartz tubes with 0.5 mm wall thickness and then rapidly quenched in a water bath. The quartz-tube water quenching method was found to be more efficient in terms of glass formation than copper-mold casting. The combination of Pd with P, Si, and Ge at composition $Pd_{82.5}P_6Si_{9.5}Ge_2$ (at%) was found capable of forming glassy rods 1 mm in diameter. Microalloying this composition with Ag was found to dramatically enhance glass formation. Specifically, the alloy $Pd_{79}Ag_{3.5}P_6Si_{9.5}Ge_2$ was found capable of forming glassy rods 6 mm in diameter, a dramatic increase in glass-forming ability.

GLASS CHARACTERIZATION

X-ray diffraction, high-resolution transmission electron microscopy (TEM), and differential scanning calorimetry (DSC) analyses verifying the amorphous structure of the $Pd_{79}Ag_{3.5}P_6Si_{9.5}Ge_2$ glass are presented in figure 2.1. Figure 2.1(a) shows the amorphous X-ray diffraction pattern taken by a Panalytical X'Pert Pro X-ray diffractometer with Cu K_α radiation. The high-resolution TEM image shown in figure 2.1(b) displays the lack of long-range order expected in a fully amorphous sample. The inset of figure 2.1(b) is the selected area diffraction pattern, confirming the amorphous nature with a fully amorphous diffuse ring diffraction pattern. Both images were taken with a field-emission FEI Tecnai F30UT TEM. The DSC scan shown in figure 2.1(c) was performed using a Netzsch Pegasus 404C DSC at a scanning rate of 0.333 °C s^{-1}. The arrows in figure 2.1(c) indicate the glass-transition temperature $T_g = 613$ K, the crystallization temperature $T_x = 644$ K, the solidus temperature $T_s = 967$ K, and the liquidus temperature $T_l = 1065$ K. The difference between T_g and T_x, termed ΔT, is 31 K and the critical casting diameter is 6 mm. The density of the glass $\rho = 10.7$ g/cm^3 was measured using the Archimedes buoyancy technique. The shear and longitudinal wave speeds were measured with a 25 MHz transducer via the pulse-echo overlap technique. The wave speeds and density were combined to calculate a shear modulus of 31 GPa and a bulk modulus of 172 GPa, resulting in a satisfactorily high Poisson's ratio of ~0.42.

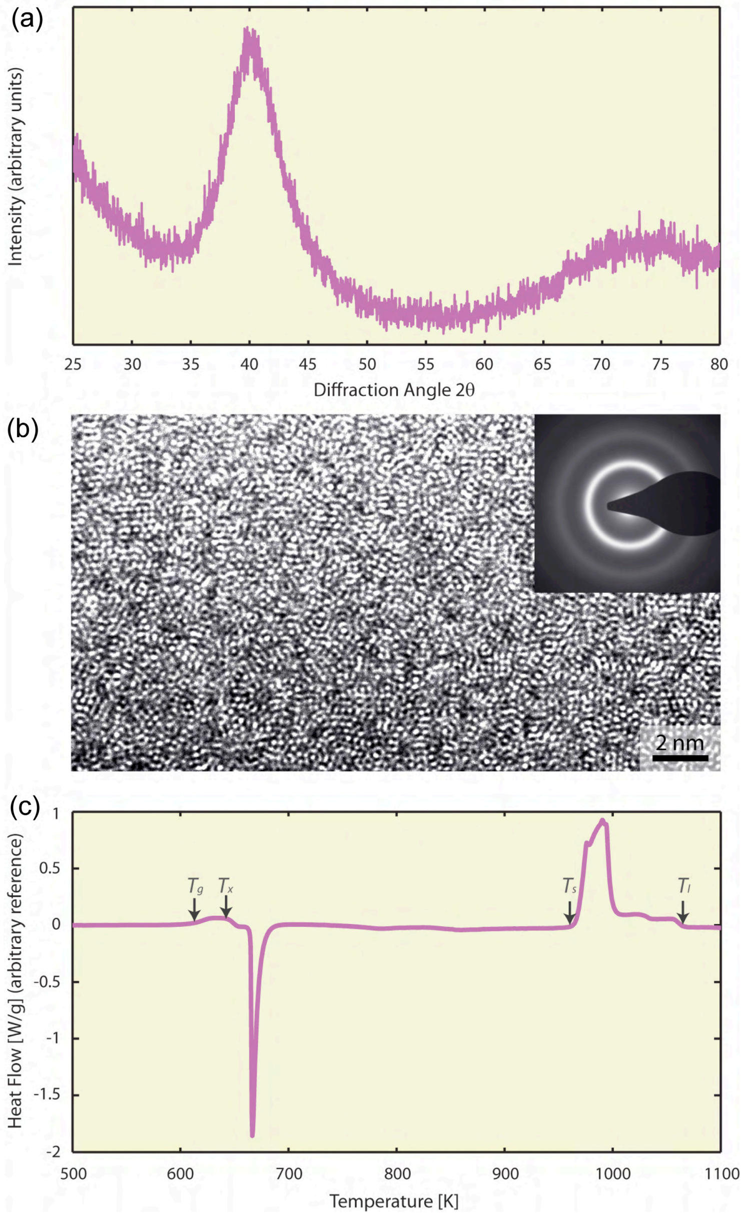

Figure 2.1 Amorphous structure of the Pd$_{79}$Ag$_{3.5}$P$_6$Si$_{9.5}$Ge$_2$ glass. (a) X-ray diffraction analysis, (b) high-resolution transmission electron microscopy, and (c) differential scanning calorimetry of a bulk Pd$_{79}$Ag$_{3.5}$P$_6$Si$_{9.5}$Ge$_2$ glassy sample. Arrows in (c) indicate the glass-transition temperature T_g = 613 K, the crystallization temperature T_x = 644 K, the solidus temperature T_s = 967 K, and the liquidus temperature T_l = 1065 K.

UNIAXIAL TENSION TESTING

The amorphous $Pd_{79}Ag_{3.5}P_6Si_{9.5}Ge_2$ tensile-test specimens were produced by water-quenching round tensile-bar-shaped quartz tubes containing the molten alloy. The specimen gauge sections were 1.5 mm in diameter and 20 mm in length. Tests were performed at room temperature with a strain rate of 5×10^{-4} s^{-1} on a screw-driven Instron 5500R testing machine (Instron, Norwood, MA), and strain was recorded using an Epsilon 3448 extensometer. The stress vs. strain loading curve for the bulk glassy sample pulled quasi-statically in uniaxial tension is presented in figure 2.2(a), with corresponding micrographs of the fracture surface in figure 2.2(b). The tensile loading response appears to depart from linear elasticity, and upon yielding, several slip events are evident, see inset in figure 2.2(a). The stress of 1490 MPa marking the first slip event is taken to represent the material plastic yield strength σ_y. Interestingly, a small total plastic strain of ~0.15% was recorded. The corresponding fracture surface figure 2.2(b) is not planar, revealing multiple failure planes (facets), and a large crack offset that did not extend across the gauge section. A ~50 μm wide shear offset is apparent, revealing evidence of extensive "stair like" plastic sliding prior to fracture. These features, which are unusual for tensile failure of a monolithic glass, are consistent with the evidence of limited plasticity recorded in the loading curve. In the absence of a microstructural stabilizing mechanism, however, the attained plasticity cannot properly be termed "ductility"; rather, this extensive multiple plane sliding activity is a demonstration of very high glass toughness.

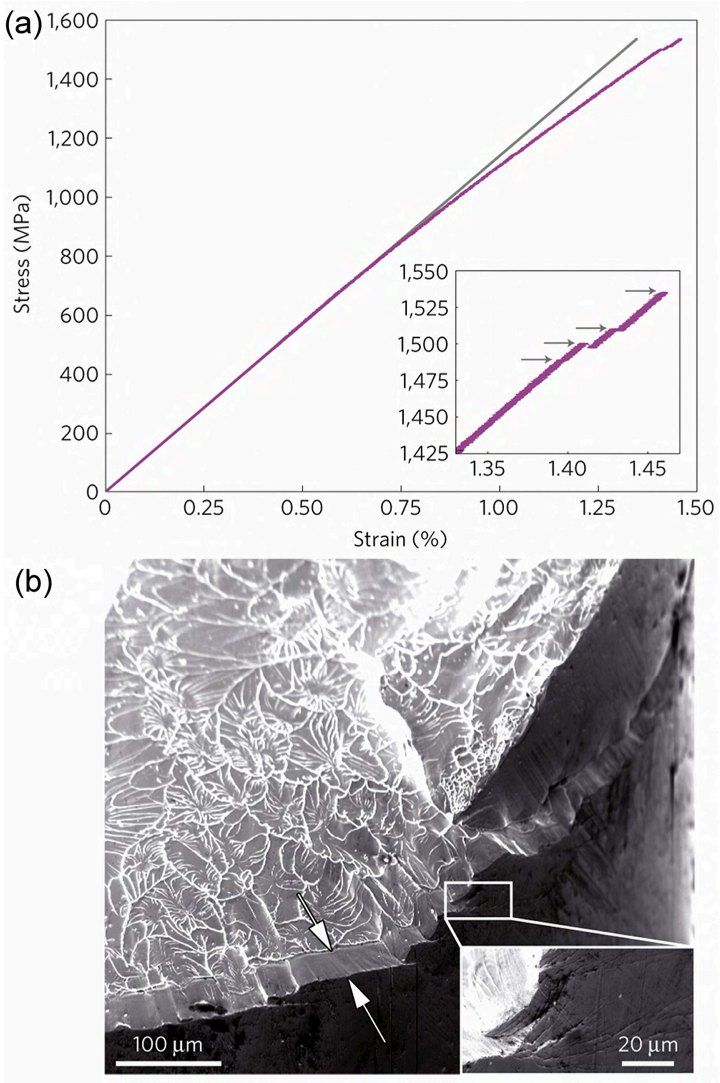

Figure 2.2 Tensile test of the $Pd_{79}Ag_{3.5}P_6Si_{9.5}Ge_2$ glass. (a) Tensile loading curve of a bulk glassy $Pd_{79}Ag_{3.5}P_6Si_{9.5}Ge_2$ specimen. The grey line is a guide for linear elastic response. Inset: Magnified view of the loading curve in the vicinity of yielding. Arrows indicate multiple slip events recorded prior to fracture. (b) Micrograph of the fracture-surface morphology. White arrows designate the shear-sliding offset width. Inset: Magnified view in the vicinity of a shear step revealing dense shear band activity.

FRACTURE TOUGHNESS CHARACTERIZATION

Assessing the fracture toughness of metallic glasses showing extensive plasticity can be extremely challenging, because meeting the fracture-mechanics requirements for linear-elastic *K*–field dominance and the development of plane-strain conditions demands specimen sizes that often exceed the critical thickness for glass formation. For example, measurement of a linear-elastic K_{IC} value of 200 MPa·m$^{1/2}$ requires sample dimensions (in terms of crack size, ligament depth, and thickness; see ASTM Standard E399 [22]) in excess of 45 mm to be considered valid; such dimensions exceed the critical casting thickness of even robust metallic bulk-glass formers. While single-value toughness measurements such as K_{IC} properly define the toughness for crack initiation in brittle materials, they are not always sufficient to characterize the toughness of glassy metals demonstrating extensive plastic yielding, or exhibiting toughening mechanisms that result in significant subcritical crack growth prior to unstable fracture [23]. The nonlinear elastic *J* measurement, which is the appropriate testing method for elastic-plastic materials, has much less restrictive specimen size validity criteria (in terms of crack size, ligament depth, and thickness; see ASTM Standard E1820 [24]) than K_{IC} measurements. A J_C value of 450 kJ/m^2 and yield strength value of 1500 MPa has a thickness and uncracked ligament requirement of 3 mm, but that is still slightly larger than is experimentally convenient. To overcome the large sample size constraints for meeting the small-scale yielding conditions while still properly accounting for the extension of the crack, we here implement a crack-tip opening displacement (CTOD) approach. This method allows us to test even smaller bending bars but still attain valid fracture toughness measurements. Specifically, this is a nonlinear-elastic fracture mechanics methodology where measurements of CTOD, δ_t, can be related to the J-integral by [25]

$$J = d_n \sigma_0 \delta_t, \tag{1}$$

where σ_0 is defined as the flow stress (the average of the yield and ultimate stresses), and d_n is a constant tabulated from the strain-hardening exponent, n, of the material [25]. A finite n is essential for the J-field to dominate over some finite region. It is well established that metallic glasses strain soften locally on yielding (i.e., within an operating shear band). When metallic glass is subjected to pure tension, the glass typically fails along a single shear band by unconstrained slipping, and no global strain hardening is generally detectable. However, when metallic glass is subjected to a quasi-stable loading geometry such as bending, there is a stress gradient from tension to compression across the sample where generated shear bands can propagate from the tensile surface to the neutral axis, multiply in number, and intersect with each other. The intersection and multiplication of shear bands generally gives rise to compatibility stresses between deformed and undeformed regions, which induces a small global hardening effect that is detectable in the true stress-strain response. For the toughness measurements, this limited degree of strain hardening occurring at the continuum scale is essentially sufficient to ensure “CTOD dominance” at the crack tip.

To determine the hardening exponent n of the $Pd_{79}Ag_{3.5}P_6Si_{9.5}Ge_2$ glass in bending, a 2.1 mm by 2.1 mm square bar sample was mechanically ground from a 3 mm diameter rod. The bar was not notched prior to testing. The three-point bending test was performed on a servo-hydraulic testing machine (MTS, Eden Prairie, MN) at a displacement rate of 10 μm·s^{-1} with a support span of 15 mm. At this sample size and strain rate, we can calculate a n from quantitative stress-strain information that is appropriate and valid for use in our CTOD fracture toughness measurements, thus ensuring that the J-field crack-tip uniqueness is preserved. Post test secondary-electron images of the unnotched bending sample are shown in figure 2.3. A great deal of shear banding can be seen in figure 2.3, both on the compression and tension side of the sample. Shear offsets of up to 200 μm can be seen in figure 2.3(d) (shown by the arrow). A crack propagated from the tension side all the way to the center of the beam, but the sample did not fracture catastrophically even after undergoing 14% bending strain. The bending fixture actually ran out of travel distance and was unable to apply any more strain. The engineering stress vs. strain curve is shown in figure 2.4 and it appears that there is no strain hardening response, only a serration at 11% strain where the crack emerges and propagates to the neutral axis of the beam. However, when inspecting the true stress vs. strain curve also in figure 2.4, it is apparent that there is a slight strain hardening response in the region before the crack emerges. The strain-hardening exponent n was measured by fitting the true stress with the relationship $\sigma_T = C\varepsilon_T^n$, where σ_T is the true stress, ε_T is the true strain, and C is a constant. The glassy $Pd_{79}Ag_{3.5}P_6Si_{9.5}Ge_2$ unnotched bending sample displays a small degree of apparent hardening in bending such that $n \approx 0.13$, ensuring dominance of CTOD at the crack tip and the appropriateness in using equation 1.

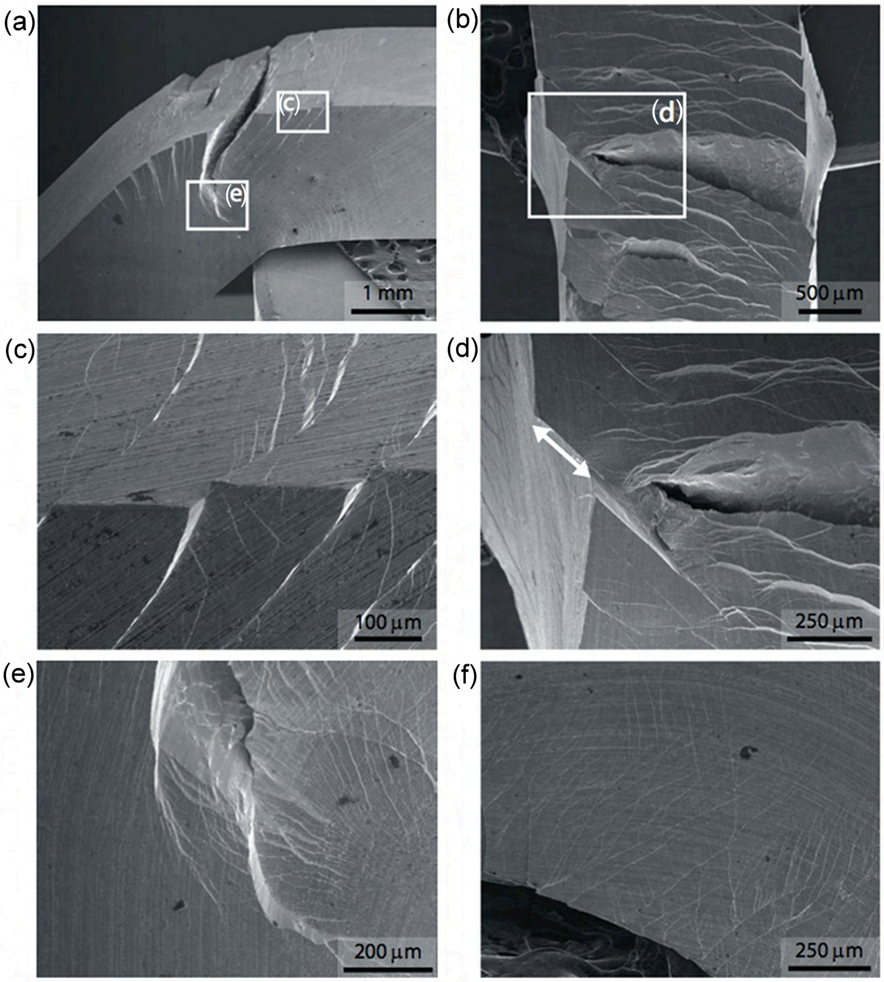

Figure 2.3 Secondary electron micrographs taken after a three-point bending test on an unnotched $Pd_{79}Ag_{3.5}P_6Si_{9.5}Ge_2$ glassy specimen. (a, b) A dense network of shear bands is observed in the tension side of the specimen along with an open crack that propagated in a stable fashion toward the center of the beam. The sample did not fracture catastrophically after undergoing the entire bending strain applicable by the fixture; (c, d) Shear offsets in the tension side are shown, that appear to be as long as 200 μm (see arrow in d). (e) Plastic-flow stabilization at the crack tip promoting stable crack growth, and (f) plastic flow in the compression side.

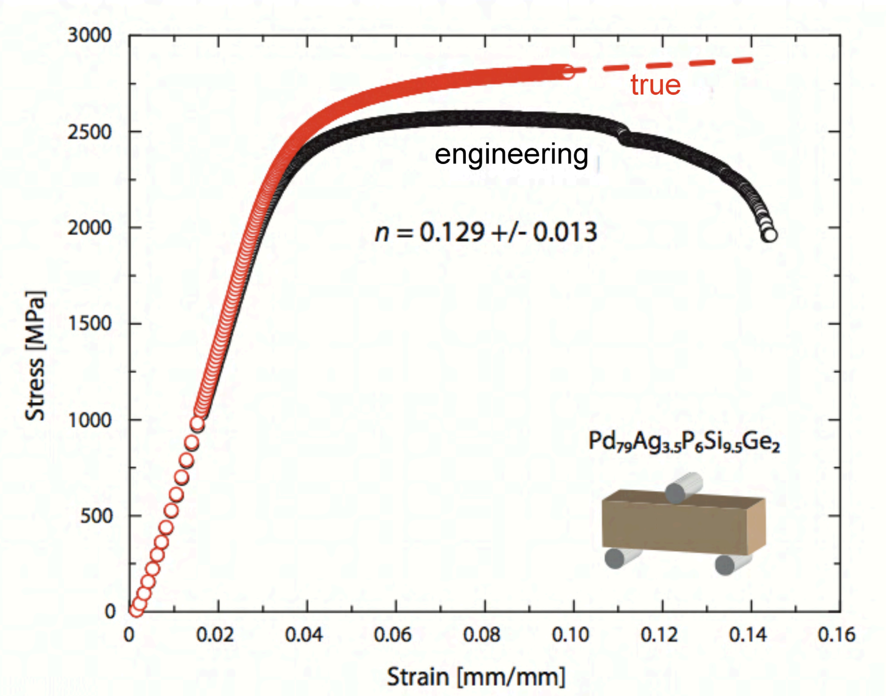

Figure 2.4 Engineering and true stress-strain curve for an unnotched $Pd_{79}Ag_{3.5}P_6Si_{9.5}Ge_2$ glassy specimen tested in a three-point bending configuration. The serration at ~11% strain (engineering curve) marks the development of the crack seen in figure 2.3, and the decreasing loading response following the serration reflects the loss of rigidity due to crack extension. The sample did not fracture catastrophically after undergoing 14% bending strain (see figure 2.3). A slight hardening response is evident in the true stress-strain curve, which can be attributed to multiplication and intersection of shear bands giving rise to local compatibility stresses.

Now that we have determined glassy $Pd_{79}Ag_{3.5}P_6Si_{9.5}Ge_2$ has a finite strain-hardening exponent, we can look at the CTOD testing method in more detail. During a fracture toughness test CTOD δ_t, crack extension Δa, and applied load are measured at regular intervals. The crack-tip opening displacement, δ_t, was measured graphically as the opening distance between the intercept of two 45° lines drawn back from the tip with the deformed profile, shown in figure 2.5, as derived by Shih [25] from the Hutchinson-Rice-Rosengren (HRR) singularity [25-28]. At each interval i, δ_t is defined as:

$$\delta_t = \delta_i - \delta_o, \tag{2}$$

where δ_i is the actual crack-tip opening displacement and δ_o is the initial crack-tip opening displacement before loading. J values were then calculated using Eq. 1 for each crack increment and converted to equivalent K values through the J-K equivalence relationship for nominally mode I fracture in plane stress:

$$K_J = (JE)^{1/2}, \tag{3}$$

with E = 88 GPa the Young's modulus of the $Pd_{79}Ag_{3.5}P_6Si_{9.5}Ge_2$ glass.

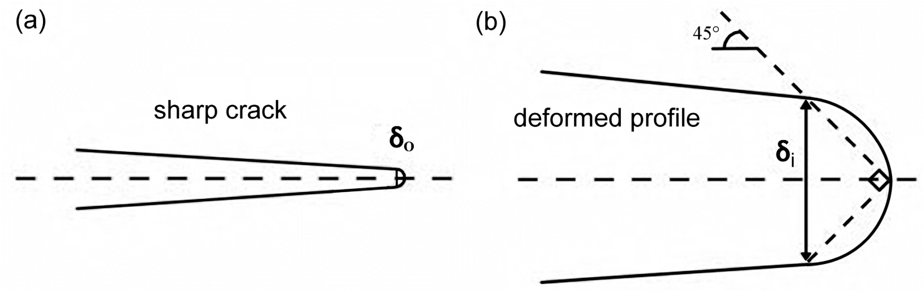

Figure 2.5 Procedure for defining the crack-tip opening displacement. (a) The initially sharp crack and (b) the deformed crack profile illustrating the 45° technique for CTOD.

It is important to note that equation (1) is valid for both plane strain and plane stress conditions, and as long as the HRR fields dominate. In the large-scale yielding regime (as in the present case), the size of the region dominated by the singularity fields is dependent on specimen geometry [26]; in this regime, Shih [25] shows that the relationship between J and δ_t, as expressed in equation (1), holds under large-scale plasticity for a hardening material when the uncracked ligament is subjected primarily to bending.

To verify that this CTOD approach is suitable for metallic glasses that undergo extensive plastic yielding, we compared the CTOD estimated K_J value against the K_J value obtained using direct J-integral measurements. It is necessary to do this comparison on a glassy material with a well-known toughness that has extensive plastic yielding in the large-scale yielding regime. Since most monolithic bulk metallic glasses fail catastrophically soon after yielding by unstable crack extension (other than the Pd-based glass of this paper), they do not exhibit rising R-curves (fracture toughness *vs.* crack extension). As an alternative, we use the well-documented R-curve [23] of the ductile-phase-reinforced metallic glass ($Zr_{39.6}Ti_{33.9}Nb_{7.6}Cu_{6.4}Be_{12.5}$) [3]. The comparison between the two methods on $Zr_{39.6}Ti_{33.9}Nb_{7.6}Cu_{6.4}Be_{12.5}$ is shown in figure 2.6. Good agreement was obtained between the two measurement techniques. More importantly, the CTOD method is shown to provide a *conservative* estimate of the toughness (i.e., it slightly underestimates the toughness).

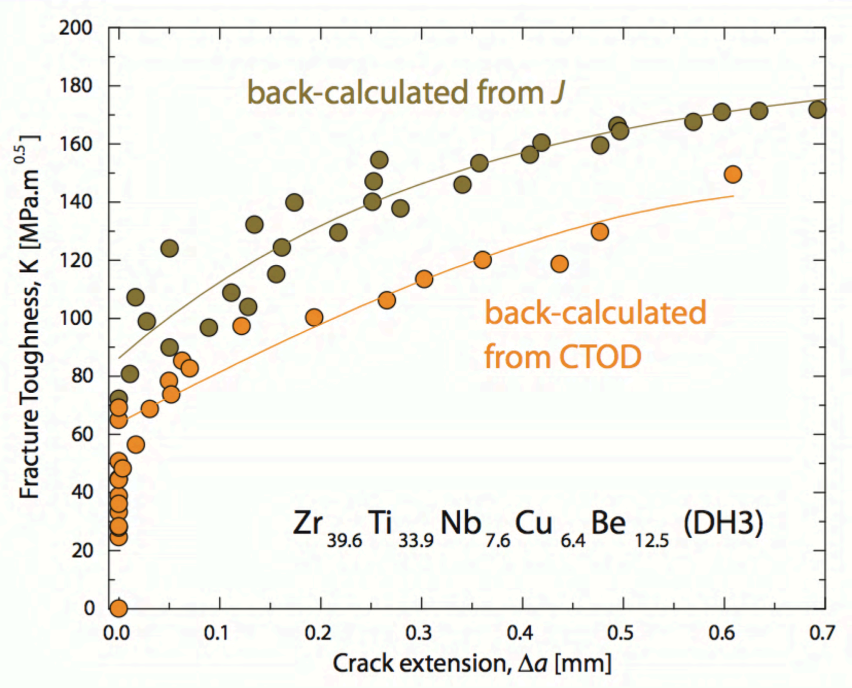

Figure 2.6 Comparison of R-curves derived using direct *J*-integral and CTOD methods for ductile-phase-reinforced metallic glass $Zr_{39.3}Ti_{33.9}Nb_{7.6}Cu_{6.4}Be_{12.5}$. Good agreement between the two measurements techniques is shown. The CTOD approach utilized in the present work can be seen to provide a conservative estimate of the fracture toughness.

Having established the appropriateness and validity of the CTOD testing method for small bending specimens of bulk metallic glass that undergo extensive plastic yielding, we will describe the CTOD testing results for the $Pd_{79}Ag_{3.5}P_6Si_{9.5}Ge_2$ glass. Single-edge notched beam SE(B) rectangular beam specimens were prepared by mechanically grinding 3 mm diameter rods of glass to square beam specimens with a cross section of 2.1 mm by 2.1 mm, and length of 20 mm. Fatigue precracking was rendered impractical here due to the small size of the samples. Instead, a razor-micronotching technique was employed to generate a sharp crack within an acceptable range [29]. The notches were first introduced using a low-speed diamond saw, and then sharpened using a razor-micronotching technique. Micro-notches with a root radius of ~5 to 10 μm were obtained by repeatedly sliding a razor blade over the saw-cut notch using a custom-made rig, while continually irrigating with a 1 μm diamond slurry. Sharp cracks with an initial crack length a of ~1.0 mm were generated in general accordance with ASTM standard E1820 [24]. Prior to testing, both specimen faces were polished to a 1 μm surface finish with a diamond suspension. In the fracture toughness tests, δ_t vs. Δa fracture toughness resistance curves (R-curves) were measured on three micronotched specimens *in situ* in a Hitachi S-4300SE/N environmental scanning electron microscope (Hitachi America, Pleasanton, CA) using a Gatan Microtest three-point bending stage (Gatan, Abington, UK) with a support span of 15 mm. The crosshead displacement was measured with a linear variable displacement transducer, while the load was recorded using a 2000 N load cell. The CTOD and crack extension were monitored at regular intervals in secondary electron mode *in vacuo* (10^{-4} Pa) at a 20 kV excitation voltage.

Using the CTOD method and experimental setup described above, we have used the CTOD approach to determine the fracture toughness of a metallic glass with critical casting thickness below the width required for direct J-integral toughness measurements. The mode I (tensile opening) fracture toughness R-curve of glassy $Pd_{79}Ag_{3.5}P_6Si_{9.5}Ge_2$ is shown in figure 2.7(a). Results for the stress intensity K_J back-calculated from the J measurements are shown in figure 2.7(b). The glass demonstrates extensive rising R-curve behavior indicative of stable crack growth over hundreds of micrometers. A near steady state K_{Jc} of ~200 MPa·m$^{1/2}$ (J_C ~460 kJ/m^2) is attained. This is an exceptionally high value for any material, but especially for an inherently non-ductile solid with an entirely amorphous structure. More interestingly, the rising R-curve in figure 2.7(b) indicates that the glass toughens as a crack extends; an attribute of ductile crystalline metals not previously thought possible for an amorphous material.

Mechanistically, we identified the salient sources of toughening in the glass by performing the fracture toughness tests *in situ* in the scanning electron microscope. This technique allows the quantitative measurement of the R-curve while simultaneously monitoring the evolution of damage ahead of the crack tip and the toughening mechanisms in the crack wake. The high toughness value is achieved by stabilizing the plastic flow processes at the opening crack tip to form a distributed damage zone accompanied by significant plastic shielding, see figure 2.7(c–k). The specific mechanisms contributing to the toughness of the $Pd_{79}Ag_{3.5}P_6Si_{9.5}Ge_2$ glass can be described in terms of a three-step process. First, shear bands form along the fan-shaped (Prandtl field) slip lines [30,31] that bend back toward the crack plane, figure 2.7(d–f). Accompanying the development of the Prandtl field, extensive localized shear sliding occurs along the evolved slip planes leading to very large shear offsets shown in figure 2.7(f). When a critical sliding strain is reached with increasing load, the extended shear bands open at the crack tip and then evolve as cracks like in figure 2.7(g). As the slip bands bend back to the crack plane enabling substantial shear sliding, the crack remains stable on its plane such that stable crack extension is attained during fracture, figure 2.7(g–k). It should be noted that outright catastrophic fracture did not occur in any of the specimens under the geometry and conditions considered here.

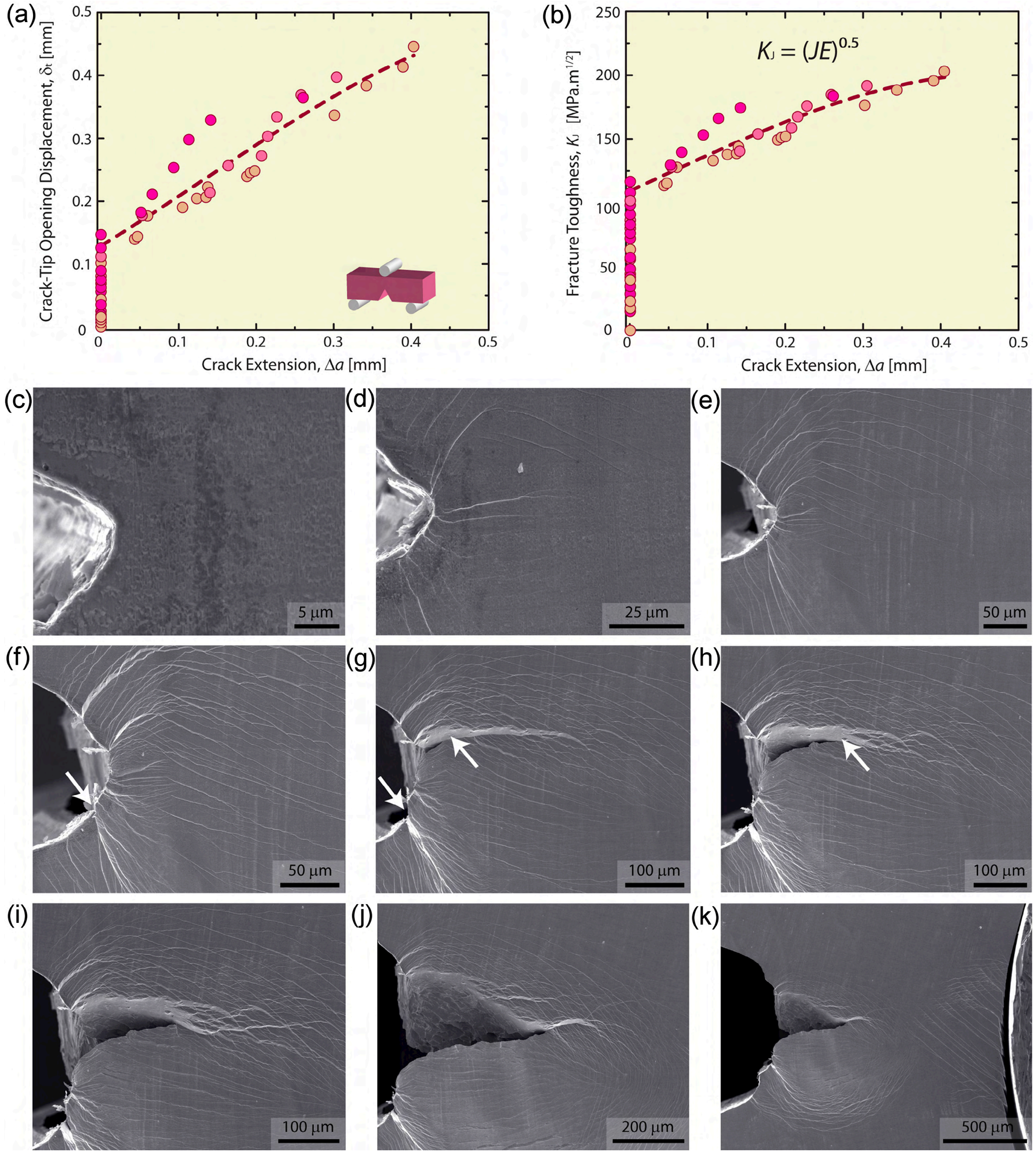

Figure 2.7 Fracture toughness measurements of the $Pd_{79}Ag_{3.5}P_6Si_{9.5}Ge_2$ glass. (a) The crack-tip opening displacement, δ_t, determined graphically, is plotted against the crack extension, Δa. (b) Fracture toughness, K_{Jc}, back-calculated from the J–integral, plotted against the crack extension, Δa. The red and orange dots in (a) and (b) represent two different fracture toughness measurements. (c-k) Scanning electron micrographs taken

during an *in situ* R-curve measurement of a SE(B) specimen. The specimen initially contained a sharp notch with a root radius of ~5 μm [25]. The crack-tip opening displacement was measured graphically at regular intervals. The corresponding fracture toughness K values are (c) 0 MPa·m$^{1/2}$ (d) 25 MPa·m$^{1/2}$, (e) 44 MPa·m$^{1/2}$, (f) 63 MPa·m$^{1/2}$, (g) 115 MPa·m$^{1/2}$, (h) 133 MPa·m$^{1/2}$, (i) 144 MPa·m$^{1/2}$, (j) 196 MPa·m$^{1/2}$, (k) 203MPa·m$^{1/2}$. (d,e) Shear bands initiate at relatively low stress intensity values along the Prandtl slip lines. (f,g) An increase in K_J is recorded associated with extensive shear sliding (indicated by arrows) that generates significant crack tip blunting. (h–k) At high stress, a crack initiates by opening of a shear band and subsequently extends at stable rate. Image (k) depicts the state of the specimen at the end of the test, showing that the sample did not fracture catastrophically after undergoing the entire strain applicable by the fixture.

Even though the mechanisms controlling the plastic zone development in the present glass are not fundamentally different than in other metallic glasses, the characteristic length scales associated with such development are considerably larger. The shear sliding process under an opening stress, which constitutes the key mechanism of plastic zone development, is illustrated schematically in figure 2.8(a). Although all metallic glasses are generally capable of undergoing limited shear band sliding in the presence of a flaw, the extent of shear sliding and observed shear offsets seen in the present glass are unprecedented. As shown in figure 2.8(b), shear offsets as large as 50 μm are attained prior to crack opening. These extended offsets enable the buildup of a very large plastic zone prior to cavitation and crack extension. The homogeneous plane-stress plastic zone radius of the $Pd_{79}Ag_{3.5}P_6Si_{9.5}Ge_2$ glass can be estimated to be as large as $r_p = K_c^2/\pi\sigma_y^2$ ≈ 6 mm. This value is the largest measured in monolithic metallic glass and rivals that of the ductile-phase-reinforced metallic glasses [3]. It also compares well with plastic zone sizes of common crystalline engineering metals.

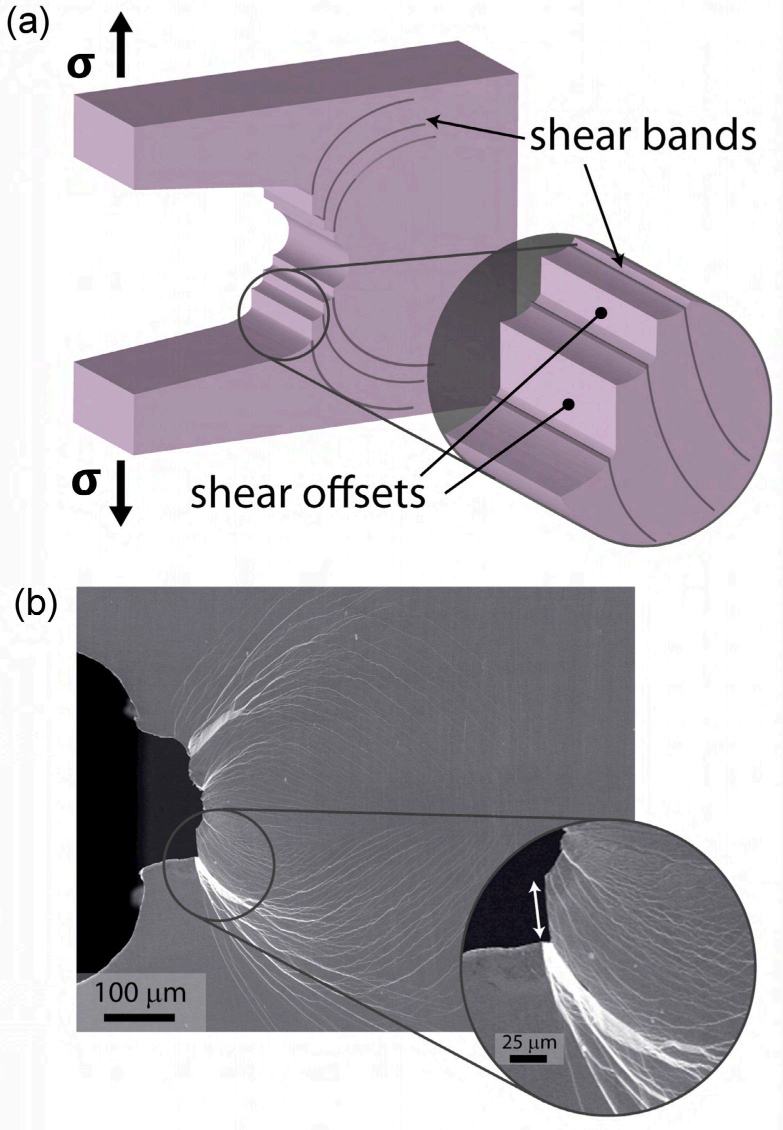

Figure 2.8 Shear-sliding mechanism governing metallic glass toughness. (a) Schematic illustrating the process of crack blunting through shear sliding in the vicinity of a flaw

under opening stress. (b) Micrograph of a deformed notch in a glassy $Pd_{79}Ag_{3.5}P_6Si_{9.5}Ge_2$ specimen showing extensive plastic shielding of an initially sharp crack. Inset: Magnified view revealing a 50 μm shear offset (arrow) developed during plastic sliding prior to the onset of crack opening

TOUGHNESS CORRELATION

To investigate the self-similarity in plastic zone development extending over several orders of magnitude in size for the various metallic glass systems, a scaling law is introduced. The number of net activated shear transformation events prior to a cavitation event in the core of an operating shear band is described here by a dimensionless parameter f, defined as $f = \exp[-(W_s - W_c)/k_BT]$, where W_s and W_c are the activation energy barriers for shear flow and cavitation respectively, and T is a reference temperature. The glass-transition temperature of the amorphous material is recognized to be a good measure of the shear flow barrier; specifically, $W_s \approx 37k_BT_g$ [14,32,33]. By further assuming that the ratio of the barrier heights W_c/W_s is dominated by the ratio of the respective elastic curvatures B/G, where B and G are the bulk and shear modulus respectively, one can arrive at the following relation for f:

$$\log\left(\frac{K_C^2}{\pi\sigma_y^2}\right) \sim \log(f) \sim \frac{W_S}{k_BT}\left(\frac{W_C}{W_S}-1\right) \approx \frac{T_g}{T}\left(\frac{B}{G}-1\right). \qquad (4)$$

In the above expression, T_g is the glass transition temperature, T is a reference temperature (here taken to be the test temperature, i.e., $T = 300$ K), G the shear modulus, B the bulk modulus, and $K_c^2/\pi\sigma_y^2$ is the plastic zone radius r_p. Interestingly, the ratio of bulk to shear modulus B/G (or equivalently, the Poisson's ratio) has been previously identified to be a key parameter associated with the toughness of a metallic glass [5,9]. This ratio alone, however, is not adequate to describe the number of net activated shear events, as it does not take into account the absolute magnitude of the activation barriers (here approximated as $\sim k_BT_g$). Using equation (1), f is estimated for a set of ten metallic glass alloys (including the present one) with toughness values that vary over two orders of magnitude, see Table 1 for the complete set of data [7,9,14,34-44]. The estimated f for the present glass is found to be higher than the other glasses, consistent with its larger plastic zone and higher toughness. In fact f, which is formulated to describe the capacity for shear flow prior to cavitation, is found to display a one-to-one correspondence with r_p. As shown in figure 2.9, parameter f correlates with r_p reasonably well, thereby describing the plastic zone development of plastically yielding glasses over four orders of magnitude in size. Based on the correlation in figure 2.9, one may conclude that the very high fracture resistance demonstrated by the present glass is attributed to a large absolute difference between W_s and W_c, as quantified by the high B/G and T_g values for this glass used equation (4). Correspondingly, we believe that this scaling law with B, G, and T_g as design variables (all of which are experimentally accessible) can serve as a viable guide for the development of a new generation of highly fracture-resistant structural glasses.

Glass-Forming Alloy	***G*** **[GPa]**	***B*** **[GPa]**	**T_g** **[K]**	**s_y** **[MPa]**	**K_c** **[MPa.m$^{1/2}$]**	**References**
$Mg_{65}Cu_{25}Tb_{10}$	19.6	44.71	415	660	2	*7,34*
$La_{55}Al_{25}Ni_5Cu_{10}Co_5$	15.6	44.2	430	700	5	*7,14,35*
$Fe_{58}Co_{6.5}Mo_{14}C_{15}B_6Er_{0.5}$	74.0	177.0	790	3700	26.5	*36,37*
$Fe_{66}Cr_3Mo_{10}C_{10}B_3P_8$	66.5	172.0	721	3100	39.3	*36,38*
$Fe_{70}Ni_5Mo_5C_5B_{2.5}P_{12.5}$	57.3	150.1	696	2670	49.8	*39*
$Zr_{55}Cu_{30}Ni_5Al_{10}$	34.7	117.9	684	1650	43.3	*40-42*
$Zr_{41.2}Ti_{13.8}Cu_{12.5}Ni_{10}Be_{22.5}$	34.1	114.1	618	1850	55	*7,43*
$Cu_{60}Zr_{20}Hf_{10}Ti_{10}$	36.9	128.2	754	1950	67.6	*44*
$Pt_{57.5}Cu_{14.7}Ni_{5.3}P_{22.5}$	33.3	198.7	508	1400	81.5	*9*
$Pd_{79}Ag_{3.5}P_6Si_{9.5}Ge_2$	31.1	171.6	613	1490	203	Present

Table 1: Data for ten metallic glass systems used in the correlation given by equation (4).

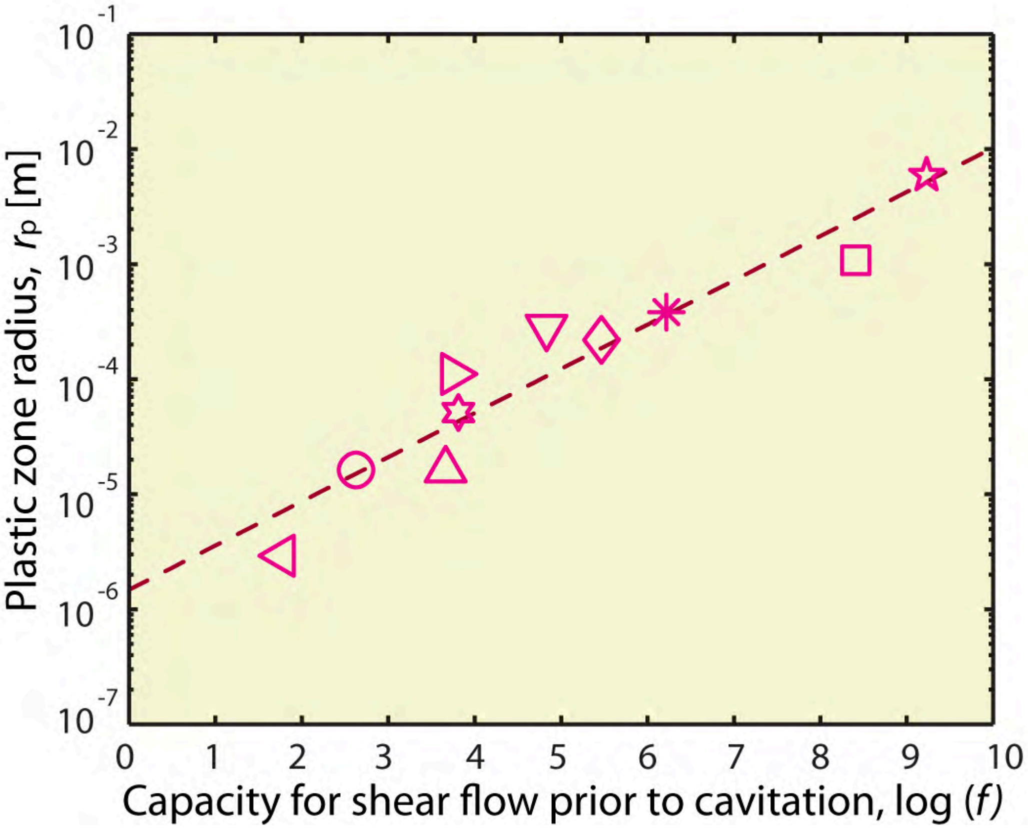

Figure 2.9 Logarithm of the plastic zone radius, defined as $K_c^2/\pi\sigma_y^2$, plotted against the estimated capacity for shear flow prior to cavitation, approximated by $-(W_s - W_c)/K_BT$ from

equation (4). Data for ten metallic glass alloys listed in Table 1 are plotted. Symbols designate the following alloys: (◁) $Mg_{65}Cu_{25}Tb_{10}$; (○) $La_{55}Al_{25}Ni_5Cu_{10}Co_5$; (△) $Fe_{58}Co_{6.5}Mo_{14}C_{15}B_6Er_{0.5}$; (✡) $Fe_{66}Cr_3Mo_{10}C_{10}B_3P_8$; (▷) $Fe_{70}Ni_5Mo_5C_5B_{2.5}P_{12.5}$; (◊) $Zr_{55}Cu_{30}Ni_5Al_{10}$; (▽) $Zr_{41.2}Ti_{13.8}Cu_{12.5}Ni_{10}Be_{22.5}$; (✱) $Cu_{60}Zr_{20}Hf_{10}Ti_{10}$; (□) $Pt_{57.5}Cu_{14.7}Ni_{5.3}P_{22.5}$; (☆) $Pd_{79}Ag_{3.5}P_6Si_{9.5}Ge_2$. Line is a regression to the data.

ASHBY DAMAGE TOLERANCE MAP

The values of fracture energy and toughness presented here for glassy $Pd_{79}Ag_{3.5}P_6Si_{9.5}Ge_2$ are comparable to values for the toughest engineering metals known (e.g., low-carbon steels). Considering that a glass lacks microstructural defects like dislocations, which rearrange to shield stress and suppress crack opening, achieving such high fracture resistance is quite remarkable. Moreover, in sharp contrast to tough crystalline metals, the absence of defects enables the very high strength associated with the amorphous structure. Thus, an unusual combination of very high strength and toughness (i.e., very high damage tolerance) is possible, a feature perhaps unparalleled by any known monolithic material. In figure 2.10 we present an Ashby map [45] showing toughness vs. strength ranges for oxide glasses, engineering ceramics, engineering polymers, and engineering metals, along with data for monolithic metallic glasses (including the present glass) and ductile-phase reinforced metallic glasses. As shown in the map, the toughness vs. strength data for the present glass lies outside the benchmarks established by the strongest and toughest steels. In summary, the present results demonstrate that the combination of toughness and strength (i.e., the level of damage tolerance) potentially accessible to amorphous materials extends beyond the traditional limiting ranges toward levels previously inaccessible to any material.

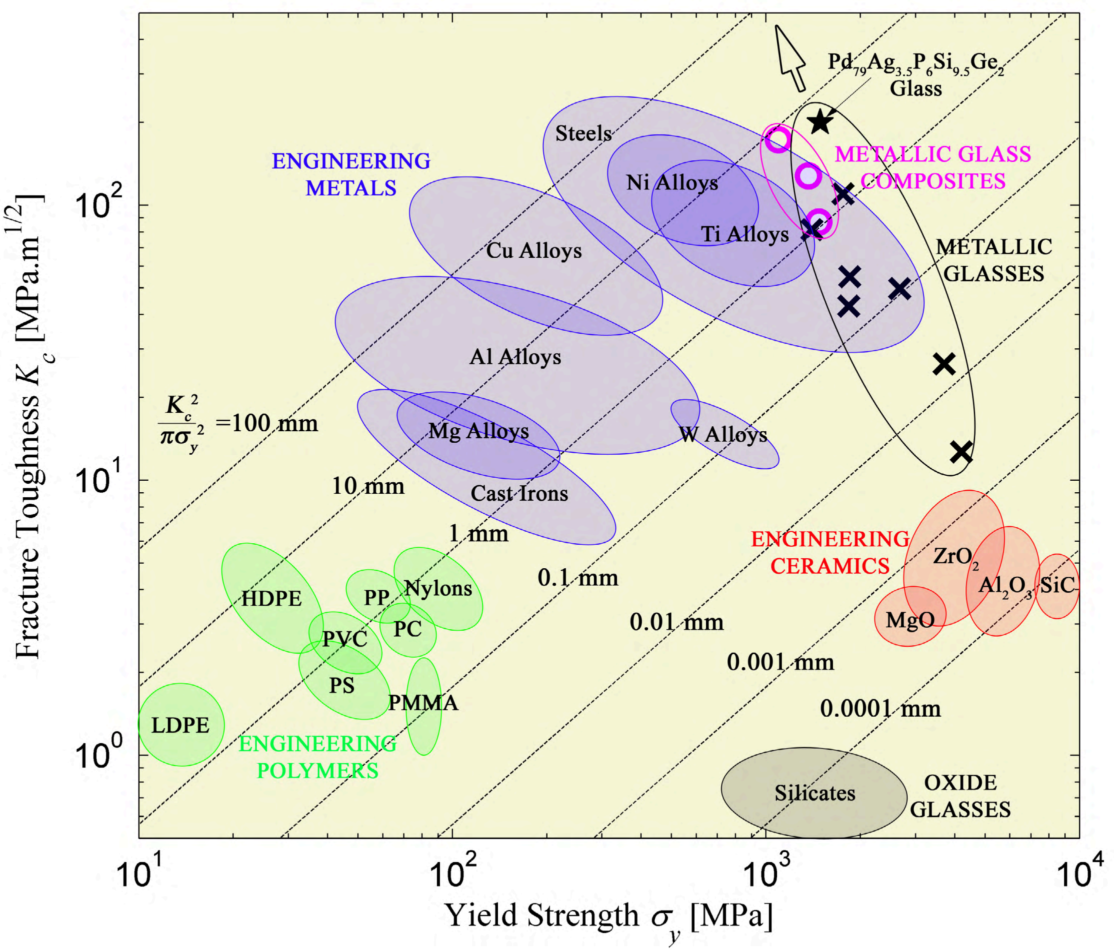

Figure 2.10 Ashby map of the damage-tolerance (toughness vs. strength) of materials. Ranges of fracture toughness vs. yield strength are shown for oxide glasses [45], engineering ceramics [45], engineering polymers [45], and engineering metals [45], along with data for the $Pd_{79}Ag_{3.5}P_6Si_{9.5}Ge_2$ glass designated by symbol (★), data for other metallic glasses: three Fe-based glasses [36,39], two Zr-based glasses [40,43], a Ti-based glass [11], and a Pt-based glass [9] all designated by symbol (×). Data for ductile-phase-

reinforced metallic glasses [3] is designated by symbol (○). Yield strength data shown for oxide glasses and ceramics represent ideal limits. Contours correspond to values for the plastic zone radius, $K_c^2/\pi\sigma_y^2$, in mm. As indicated by the arrow, the combination of toughness and strength (i.e., damage tolerance) potentially accessible to metallic glasses extends beyond the traditional limiting ranges toward levels previously inaccessible to any material.

BIBLIOGRAPHY

[1] M. E. Launey and R. O. Ritchie, Adv Mater **21**, 2103 (2009).

[2] R. O. Ritchie, Science **320**, 448 (2008).

[3] D. C. Hofmann, J.-Y. Suh, A. Wiest, G. Duan, M. L. Lind, M. D. Demetriou, and W. L. Johnson, Nature **451**, 1085 (2008).

[4] M. F. Ashby and A. L. Greer, Scripta Materialia **54**, 321 (2006).

[5] J. J. Lewandowski, W. H. Wang, and A. L. Greer, Philosophical Magazine Letters **85**, 77 (2005).

[6] J. Xu, U. Ramamurty, and E. Ma, Jom-Us **62**, 10 (2010).

[7] X. K. Xi, D. Q. Zhao, M. X. Pan, W. H. Wang, Y. Wu, and J. J. Lewandowski, Phys Rev Lett **94**, 125510 EP (2005).

[8] P. A. Hess, S. J. Poon, G. J. Shiflet, and R. H. Dauskardt, Journal of Materials Research **20**, 783 (2005).

[9] J. Schroers and W. Johnson, Phys Rev Lett **93**, (2004).

[10] J.-Y. Suh, R. D. Conner, C. P. Kim, M. D. Demetriou, and W. L. Johnson, Journal of Materials Research **25**, 982 (2010).

[11] X. J. Gu, S. J. Poon, G. J. Shiflet, and J. J. Lewandowski, Acta Mater **58**, 1708 (2010).

[12] A. Inoue, B. Shen, H. Koshiba, H. Kato, and A. R. Yavari, Nat Mater **2**, 661 (2003).

[13] R. Conner, W. Johnson, N. Paton, and W. Nix, J Appl Phys **94**, 904 (2003).

[14] W. Johnson and K. Samwer, Phys Rev Lett **95**, 195501 (2005).

[15] E. Bouchaud, D. Boivin, J. L. Pouchou, D. Bonamy, B. Poon, and G. Ravichandran, Epl-Europhys Lett **83**, (2008).

[16] P. Duwez, R. H. Willens, and R. C. Crewdson, J Appl Phys **36**, 2267 (1965).

[17] H. S. Chen, J. T. Krause, and E. Coleman, J Non-Cryst Solids **18**, 157 (1975).

[18] H. S. Chen and D. Turnbull, Acta Metallurgica **17**, 1021 (1969).

[19] H. Kimura and T. Masumoto, Acta Metallurgica **28**, 1663 (1980).

[20] H. Kimura and T. Masumoto, Acta Metallurgica **28**, 1677 (1980).

[21] H. W. Kui, A. L. Greer, and D. Turnbull, Appl Phys Lett **45**, 615 (1984).

[22] *ASTM Standard E399* (ASTM International, West Conshohocken, PA, 2012).

[23] M. E. Launey, D. C. Hofmann, J. Y. Suh, H. Kozachkov, W. L. Johnson, and R. O. Ritchie, Appl Phys Lett **94**, 241910 (2009).

[24] *ASTM Standard E1820* (ASTM International, West Conshohocken, PA, 2011).

[25] C. F. Shih, J Mech Phys Solids **29**, 305 (1981).

[26] C. F. Shih and M. D. German, International Journal of Fracture **17**, 27 (1981).

[27] J. W. Hutchinson, Acta Mater **16**, 337 (1968).

[28] J. R. Rice and G. F. Rosengren, Acta Mater **16**, 1 (1968).

[29] P. Lowhaphandu and J. J. Lewandowski, Scripta Materialia **38**, 1811 (1998).

[30] A. Alpas, L. Edwards, and C. Reid, Metall and Mat Trans A **20**, 1395 (1989).

[31] K. M. Flores and R. H. Dauskardt, Scripta Materialia **41**, 937 (1999).

[32] M. D. Demetriou, J. S. Harmon, M. Tao, G. Duan, K. Samwer, and W. L. Johnson, Phys Rev Lett **97**, (2006).

[33] W. L. Johnson, M. D. Demetriou, J. S. Harmon, M. L. Lind, and K. Samwer, Mrs Bull **32**, 644 (2007).

[34] X. Xi, D. Zhao, M. Pan, and W. Wang, J Non-Cryst Solids **344**, 189 (2004).

[35] N. Nagendra, U. Ramamurty, T. T. Goh, and Y. Li, Acta Mater **48**, 2603 (2000).

[36] A. Shamimi Nouri, X. J. Gu, S. J. Poon, G. J. Shiflet, and J. J. Lewandowski, Philosophical Magazine Letters **88**, 853 (2008).

[37] X. J. Gu, S. J. Poon, and G. J. Shiflet, Journal of Materials Research **22**, 344

(2007).

[38] X. J. Gu, S. J. Poon, G. J. Shiflet, and M. Widom, Appl Phys Lett **92**, 161910 (2008).

[39] M. D. Demetriou, G. Kaltenboeck, J.-Y. Suh, G. Garrett, M. Floyd, C. Crewdson, D. C. Hofmann, H. Kozachkov, A. Wiest, J. P. Schramm, and W. L. Johnson, Appl Phys Lett **95**, 041907 (2009).

[40] A. Kawashima, H. Kurishita, H. Kimura, and T. Zhang, Materials Transactions **46**, 1725 (2005).

[41] J. Luo, H. Duan, C. Ma, S. Pang, and T. Zhang, Materials Transactions **47**, 450 (2006).

[42] M. L. Vaillant, V. Keryvin, T. Rouxel, and Y. Kawamura, Scripta Materialia **47**, 19 (2002).

[43] C. J. Gilbert, R. O. Ritchie, and W. L. Johnson, Appl Phys Lett **71**, 476 (1997).

[44] P. Wesseling, T. G. Nieh, W. H. Wang, and J. J. Lewandowski, Scripta Materialia **51**, 151 (2004).

[45] M. F. Ashby, *Materials Selection in Mechanical Design* (Pergamon Press, Oxford; New York, 1992).

Chapter 3

INFLUENCE OF CONFIGURATIONAL DISORDER ON THE INTRINSIC FRACTURE TOUGHNESS OF METALLIC GLASSES

ABSTRACT

The effect of the configurational disorder of the glass structure on the intrinsic fracture toughness of metallic glasses is explored. The fracture toughness measured in as-quenched and well-defined relaxed configurations is correlated with measured elastic constants and recovered enthalpy in an effort to quantify the influence of configurational disorder on toughness. The as-quenched glass is found to exhibit a broadly varying toughness that cannot be correlated to the average configurational properties, and is thought to arise from a large configurational disorder captured in the as-quenched state. In contrast, the glass equilibrated at well-defined configurations demonstrates a consistent toughness that is systematic and correlatable to the average configurational properties. The large configurational disorder in the as-quenched state responsible for the wide toughness variance is attributed to a dynamic vitrification process capturing a broad spectrum of unrelaxed modes; the spectrum narrows significantly following relaxation of the glass, promoting more consistent toughness.

INTRODUCTION

Toughness in metallic glasses is accommodated by a mechanism of highly localized plastic flow, known as shear banding, originating at the crack tip. Shear bands blunt the crack tip and shield it from the applied opening stress, and in instances when extensive shear banding is enabled, crack growth may be entirely arrested [1]. Shear banding is an intrinsic toughening mechanism taking place solely in the material ahead of the crack tip [2]. Specifically, energy is dissipated when the local elastic stress in front of the crack tip is large enough to overcome the activation barrier for shear flow (i.e., the stress reaches the plastic yield strength) such that shear bands are nucleated inside the region called the "plastic zone." The larger the density of shear bands and the longer those shear bands slide within the plastic zone before cavitation intervenes to facilitate crack extension, the larger the plastic zone and the greater the toughness of the material. The extent to which the glass can undergo shear banding in the absence of cavitation ahead of the crack tip is intimately related to the local configurational properties of the glass in the immediate vicinity of the crack tip.

The toughness of metallic glasses is known to vary greatly between the different compositional families, ranging from very high for noble-metal glasses (up to 200 $\mathrm{MPa \cdot m^{1/2}}$) [1], to moderately high for early-transition metal glasses (~100 $\mathrm{MPa \cdot m^{1/2}}$) [3], to very low for ferrous metal glasses (under 10 $\mathrm{MPa \cdot m^{1/2}}$) [4]. But considerable variability in toughness is often reported for the same metallic glass composition. For example, a thorough investigation by Kawashima et al. [5] using 35 specimens revealed a significant variation in the fracture toughness of $Zr_{55}Ni_5Cu_{30}Al_{10}$ ranging from 36 to

76 MPa·m$^{1/2}$. A comparable scatter was also reported for $Zr_{52.5}Ti_5Ni_{14.6}Cu_{17.9}Al_{10}$ [6]. In both of these studies, the scatter was attributed to extrinsic factors such as partial crystallinity or inclusions. These inhomogeneities tend to precipitously drop toughness when intersected by a propagating crack, thus widening the scatter in the measured toughness. Their intersection with a crack is typically associated with a change in fracture mode, displaying a cleavage fracture region in the crack wake. In brittle metallic glasses the effect of oxide inclusions is much more profound, as it essentially dominates the fracture resistance of those glasses [7,8]. Yet a large variability in toughness is often reported for glasses that are relatively tough and expected to be generally insensitive to inclusions. Even when processed under near-ideal conditions (high-purity and low-oxygen content elements, highly-inert atmosphere) that restrict the formation of oxide inclusions, and are fully amorphous as verified by careful X-ray diffractometry, such tougher glasses still often display a large variation in toughness. For example, the fracture toughness of pristine $Zr_{41.2}Ti_{13.8}Ni_{10}Cu_{12.5}Be_{22.5}$ samples processed under essentially identical conditions was found to vary from a low value of 25 MPa·m$^{1/2}$ to a high value of 75 MPa·m$^{1/2}$, while no visible inhomogeneities could be detected in the fracture morphology to suggest influence by extrinsic factors [9]. This suggests that significant variability in toughness may also be caused by intrinsic factors at much shorter length scales associated with local inhomogeneities in the glassy structure.

Structural relaxation is known to profoundly affect the toughness of metallic glass. Gradually relaxing the glass from the highly-disordered as-quenched state to a well-defined equilibrium state at a temperature lower than the fictive temperature associated with the as-quenched state is found to severely compromise toughness [10,11]. This is understood to be a consequence of relaxing at a lower level in the potential energy landscape, associated with a higher barrier for shear flow as compared to the as-quenched state [12]. As those previous investigations always involve a change in the fictive temperature, any effects of the decrease in the degree of disorder on going from the highly disordered as-quenched state to a less disordered equilibrium state are not addressed. A recent computational work suggests that the degree of disorder can have quite a significant effect on toughness, perhaps as significant as the effect of varying the fictive temperature [13]. In the present study, we experimentally isolate the effect of varying glass disorder from the effect of changing the fictive temperature and attempt to independently examine their respective effects on toughness.

The average configurational properties and fracture toughness are measured for several specimens in the as-quenched state as well as in states relaxed at various temperatures around the glass transition. A relaxation temperature that closely approximates the fictive temperature of the as-quenched state is determined by correlating the respective configurational properties. Comparing the toughness for relaxed and as-quenched states at approximately the same fictive temperature enables, for the first time, assessment of the effects of glass disorder on fracture toughness. In order to obtain an accurate representation of the average configurational properties ahead of the crack tip plane such that valid correlations with fracture toughness are enabled, ultrasound measurements were taken just ahead of the crack tip through the thickness of each sample. In order to circumvent the unpredictable adverse effects on toughness of either crystallinity or inclusions, each tested sample was prepared with diligent care and was thoroughly inspected. The fully amorphous nature of the tested samples was carefully inspected by X-ray diffraction and differential scanning calorimetry. The alloy ingots were prepared using high-purity elements with low oxygen content, alloyed under ultra-pure inert atmosphere. The amorphous rods were prepared by overheating the melt at a controlled temperature substantially higher than the alloy liquidus temperature prior to quenching. Long-range residual stresses arising in as-quenched samples, that could substantially influence toughness, were eliminated during the extensive grinding of the rods in to rectangular shaped beams. The cracks were also generated near the centerline of the rods where residual stresses are essentially zero. Lastly, in order to eliminate the influence of any spatial or compositional variability that could be introduced by testing individually cast samples, several cast rods were produced and several specimens were extracted from each cast rod from various locations along the rod.

SAMPLE PREPARATION AND CONFIGURATIONAL STATE CHARACTERIZATION

Three ingots of $Zr_{35}Ti_{30}Cu_{8.25}Be_{26.75}$ were prepared by weighing appropriate amounts of Zr (single crystal, 99.92% purity), Ti (single crystal, 99.99% purity), Cu (99.999% purity), and Be (99.9% purity). Each ingot was alloyed by arc melting in a Ti-gettered Argon atmosphere on a water-cooled copper hearth, and flipped at least four times to ensure chemical homogeneity. Three rods 8 mm in diameter with lengths varying between 5 and 13 cm were produced by injection casting in a copper mold from the molten liquid state at 1100°C. Controlled melt heating was performed with RF induction power under argon atmosphere, and with the melt temperature being monitored by an infrared pyrometer. Four specimens extracted from a single rod were annealed and relaxed at different temperatures around the glass transition in order to investigate several relaxed states of the glass. Three specimens extracted from a single rod, and one more specimens extracted from another cast rod were investigated in their as-quenched state. The amorphous nature of all specimens was verified by X-ray diffraction with Cu Kα radiation. The cylindrical rod segments were mechanically ground into ASTM E399 [14] single-edge-notch-bend rectangular bars that were 7 mm wide, 3.5 mm thick, and slightly longer than the testing span length of 28 mm. The specimen faces perpendicular to the crack were mirror polished with 0.02 μm colloidal silica. Notches having a length of 1 to 1.5 mm and a root radius of 125 μm were created on all samples using a wire saw with a 1 μm diamond slurry. Fatigue precracks were then created using a servo-hydraulic Materials Testing System MTS at a sinusoidal loading frequency of 10 Hz, R ratio of 0.1 and ΔK of ~11 MPa·m$^{1/2}$ while also never exceeding 60% of even the most brittle K_Q result. The combined length of the notch and fatigue precrack was ~3.5 mm on all samples, equal to the sample thickness in accordance with ASTM E399 [14]. Densities were measured using the Archimedes technique according to the ASTM standard C693 [15]. The room temperature shear and longitudinal wave speeds were measured using the pulse-echo overlap technique with 25 MHz ultrasound transducers. We note that the ultrasound measurements were taken right at the tip of the crack through the thickness of the sample in order for the measurements to represent the average properties ahead of the crack tip plane. Using the data for the shear wave speed, longitudinal wave speed, and density ρ, the shear modulus G, bulk modulus B, and Poisson's ratio v of the samples were calculated. Differential scanning calorimetry (DSC) using a Netzsch 404C calorimeter at a scan rate of 0.16 $°C \cdot s^{-1}$ was performed using a small segment from each specimen to evaluate the glass transition temperature T_g and the associated recovered enthalpy ΔH at T_g.

The samples were relaxed by sealing them inside a quartz tube under an Argon atmosphere and annealing them for a sufficient amount of time for the glass to relax to a well-defined equilibrium liquid state. The four samples were annealed at the relaxation temperatures T_R of 280 °C, 300 °C, 320 °C, and 340 °C, which are just above and below the reported glass transition temperature T_g of 305 ºC for $Zr_{35}Ti_{30}Cu_{8.25}Be_{26.7}$ [16]. The total annealing time for the 280 °C, 300 °C, 320 °C, and 340 °C samples at their respective temperatures is 520, 170, 41, and 15 minutes, respectively. The annealing of each sample was broken in to at least three annealing steps to ensure the samples do not crystallize and reach full equilibrium. The ρ, G, and B of each sample was measured after each annealing step, and equilibration was assessed by monitoring the relaxation of these variables [17]. X-ray diffraction was also performed after each annealing step to verify that the samples remain amorphous. The vibrational component (Debye-Grüneisen effect) of the moduli was not included in the reported moduli, as it is understood from prior work [12,17-19] that the configurational component of the moduli mostly controls the irreversible response of the liquid. However, we have included the calculation of the Debye-Grüneisen effect on the shear modulus and bulk modulus in appendix A, which contains the calculation of the coefficient of thermal expansion and the measurement of the shear and longitudinal wave speeds at, and below, room temperature.

The measured ρ, G, B, and ν for the equilibrated and as-quenched states are listed in table 3.1. Across the relaxed states, G is shown to decrease very systematically with temperature, as expected by relaxing to increasingly higher and shallower potential energy wells in the glass landscape [12,17-19]. The decrease in G is by ~4%, considerably outside the measurement error. On the other hand, B decreases by just ~0.3%, well within the measurement error. Therefore, across the relaxed states where substantial configurational rearrangements take place, G more closely tracks these configurational rearrangements as compared to B. In this chapter, G will be regarded as the state variable quantifying the configurational state of the glass, as is widely understood to be directly proportional to the activation barrier to shear flow [12]. By plotting G vs. T_R in figure 3.1(a), a near linear relationship is observed, as expected from the work of Lind et al [17], we show the poor fitting of B vs. T_R in appendix B for contrast. The slope of the linear fit to the relaxed G vs. T_R is -23.1 MPa·°C^{-1}. On the other hand, the data for the as-quenched specimens, which are superimposed in figure 3.1(a) as dashed lines extending across the entire temperature range, appear to be considerably less systematic and less consistent. Three of the samples display a G around 35 GPa with a rather small variance that is within the measurement error, suggesting a unique fictive temperature around 345 °C. The other sample displays a G that is appreciably higher than 35 GPa by a margin outside the measurement error, representing a higher fictive temperature, which is probably a consequence of spatially varying cooling conditions associated with the copper mold casting process.

The recovered enthalpy ΔH, which is understood to be directly related to the configurational energy of the metallic glass [18] will be used here as an independent variable quantifying the configurational state of the glass. The recovered enthalpies were calculated in reference to the as-quenched sample that displayed the lowest value of ΔH. The DSC scans performed at 0.16 $°\mathrm{C}\cdot\mathrm{s}^{-1}$ that were used in determining the relative values of ΔH are shown in appendix C. The ΔH data are listed in table 3.1 and plotted vs. T_R in figure 3.1(b). Like with G, the ΔH values for the relaxed states decrease very systematically and consistently with T_R over a rather broad range. A linear fit to the data reveals a slope of -6.6 J/(mol·°C). On the other hand, the ΔH data for the as-quenched states closely resemble the behavior displayed by the G data, with three of the data suggesting a rather unique fictive temperature along with an outlying data point. By plotting G vs. ΔH in figure 3.1(c), a good correlation between G and ΔH is found, which even extends through the anomalous as-quenched data point. The near linear relationship reflects the one-to-one correspondence between G and ΔH independent of the fictive temperature. The linear fit to all samples reveals a slope of $\mathrm{d}G/\mathrm{d}\Delta H = 3.07 \times 10^{-7}\ \mathrm{m}^3/\mathrm{mol}$. The tight G vs. ΔH correlation confirms that the average measured shear modulus accurately reflects the configurational enthalpy of the associated glass state, a concept that forms the basis for the cooperative shear model describing shear flow activation in metallic glass [12].

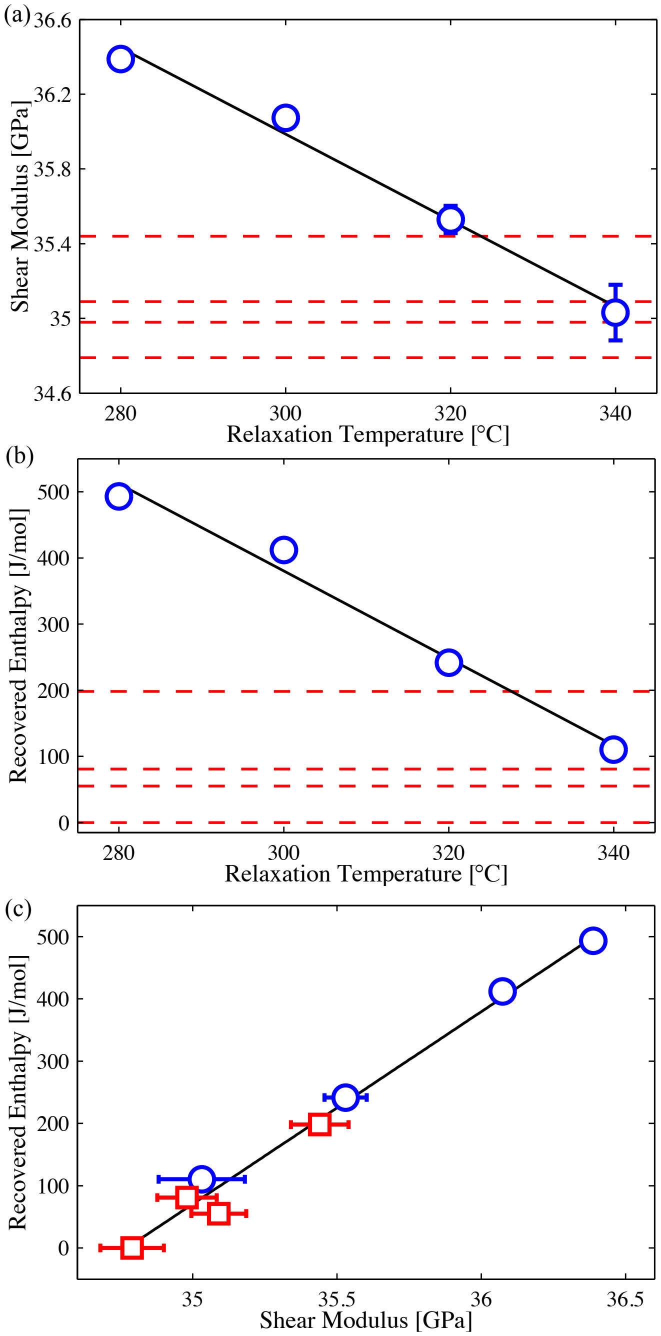

Figure 3.1 (a) Shear modulus G (with associated measurement error) vs. relaxation temperature T_R and (b) recovered enthalpy ΔH vs. relaxation temperature T_R for equilibrated $Zr_{35}Ti_{30}Cu_{8.25}Be_{26.75}$ samples (blue circles). The lines are linear fits through the data, and the extended dashed lines correspond to the values for the three as-quenched

$Zr_{35}Ti_{30}Cu_{8.25}Be_{26.75}$ samples. (c) Shear modulus G (with associated measurement error) vs. recovered enthalpy ΔH for both equilibrated (blue circles) and as-quenched (red squares) $Zr_{35}Ti_{30}Cu_{8.25}Be_{26.75}$ samples.

FRACTURE TOUGHNESS TESTING

Square beams with a side length of ~3.5 mm and an aspect ratio of ~2 were sectioned from the fracture toughness specimens post fracture within millimeters of the notch and were polished plane parallel for compression testing. The stress vs. strain response was measured at a strain rate of 10^{-3} s^{-1} in an Instron load frame, and the yield strength σ_y was assessed. The measured σ_y values, shown in table 1, show practically no variation. While this is not particularly useful in terms of revealing a correlating tendency, we can use the average σ_y to calculate the limiting value that can be considered as valid plane strain fracture toughness, K_{IC}, according to ASTM E399 [14]. Plane strain and small-scale yielding conditions are ensured when certain sample dimensions (total crack length, uncracked ligament length, and the out-of-crack-plane thickness) are greater than or equal to $5K_Q^2/2\sigma_y^2$. We estimate that for the present samples, any fracture toughness less than or equal to 64 $MPa\cdot m^{1/2}$ can be considered a valid K_{IC} measurement.

The fracture toughness tests were carried out in three-point bending mode on a MTS load frame at a constant displacement rate of 0.3 mm/min. The critical stress intensity K_Q was calculated from the critical load according to ASTM E399 [14], and is listed in table 1 for each sample. Three of the eight K_Q values slightly exceeded the K_{IC}

valid cutoff of 64 MPa·m$^{1/2}$. The fracture toughness values in the relaxed states are found to vary broadly from 26 to 74 MPa·m$^{1/2}$ over the T_R range considered. More interestingly, the fracture toughness in the as-quenched states are found to vary even more broadly, ranging from 31 to 110 MPa·m$^{1/2}$ between the five tests, with an average of 75 MPa·m$^{1/2}$ and a standard deviation of 35 MPa·m$^{1/2}$. Images of the fracture surfaces were taken with a LEO 1550VP field emission scanning electron microscope SEM. The relaxed states fracture surfaces are shown in figure 3.2 and the as-quenched fracture surfaces are shown in figure 3.3. The LEO SEM was also used to investigate compositional contrast in the samples with backscattered electron images and energy dispersive X-ray spectroscopy EDS. No evidence of contrast was found with either technique. This, together with the absence of any cleavage fracture region in the vicinity of the pre-crack, suggest that fracture was likely not triggered by entrained oxide inclusions in any of the samples tested here [8]. Therefore it appears that fracture has been accommodated entirely by a shear process, even in the most brittle cases. During fracture, the shear banding process produces a jagged and rough fracture surface zone ahead of the crack tip, whose degree and extent is expected to correlate with the associated plastic zone radius determined by $K_Q^2/\pi\sigma_y^2$ [9]. The sample fracture toughness and surface roughness in both figure 3.2 and figure 3.3 increases as the images go from top to bottom.

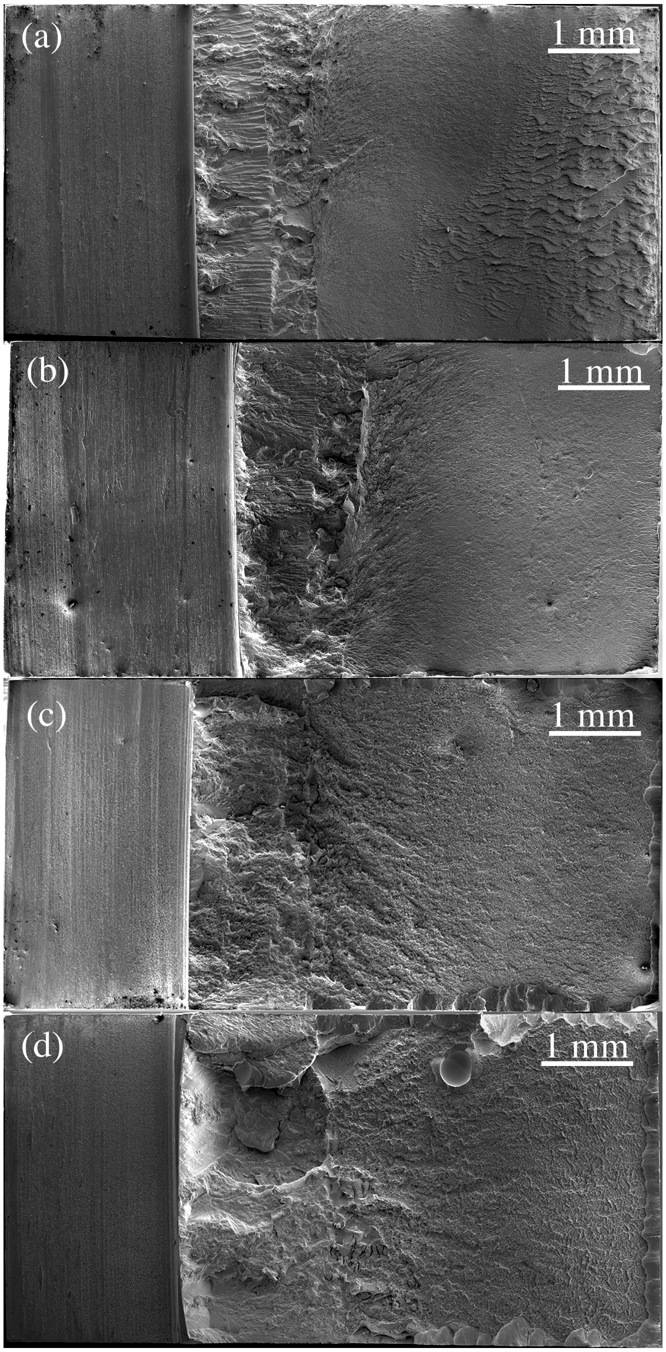

Figure 3.2 Scanning electron micrographs of the fracture surfaces from $Zr_{35}Ti_{30}Cu_{8.25}Be_{26.75}$ fracture toughness samples relaxed, prior to fracture, at (a) 280 °C $K_Q = 26$ MPa·m$^{1/2}$, (b) 300 °C $K_Q = 36$ MPa·m$^{1/2}$, (c) 320 °C $K_Q = 61$ MPa·m$^{1/2}$, and (d) 340 °C $K_Q = 74$ MPa·m$^{1/2}$.

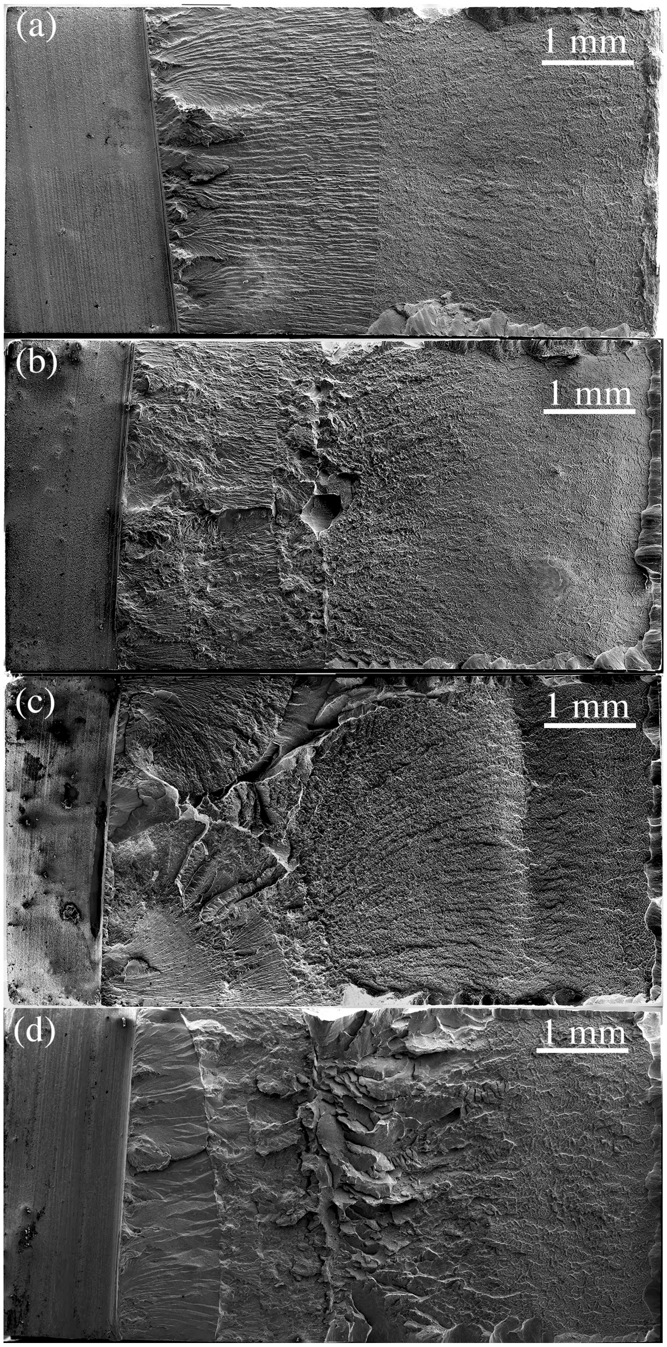

Figure 3.3 Scanning electron micrographs of the fracture surfaces from $Zr_{35}Ti_{30}Cu_{8.25}Be_{26.75}$ fracture toughness samples tested in their as-quenched state: (a) K_Q = 62 MPa·m$^{1/2}$, (b) K_Q = 96 MPa·m$^{1/2}$, (c) K_Q = 31 MPa·m$^{1/2}$, and (d) K_Q = 110 MPa·m$^{1/2}$.

Table 3.1 Data for the density ρ, shear modulus G, bulk modulus B, Poisson's ratio v, recovered enthalpy ΔH, yield strength σ_y, glass-transition temperature T_g, and fracture toughness K_Q for the $Zr_{35}Ti_{30}Cu_{8.25}Be_{26.75}$ samples in various relaxed states at temperatures T_R as well as in their as-quenched state.

Sample State	ρ [g/cm^3]	G [GPa]	B [GPa]	v [—]	ΔH [J/mol]	σ_y [MPa]	T_g [°C]	K_Q [MPa·m$^{1/2}$]
280°C Relaxed	5.378	36.39	105.8	0.3457	493	1700	303	26
300°C Relaxed	5.376	36.07	105.8	0.3469	412	1680	300	36
320°C Relaxed	5.373	35.53	105.6	0.3488	242	1710	298	61
340°C Relaxed	5.367	35.03	105.4	0.3505	110	1700	298	74
As-quenched	5.366	35.44	104.9	0.3482	198	1690	301	62
As-quenched	5.368	34.98	104.6	0.3495	81	1630	304	96
As-quenched	5.379	35.09	106.0	0.3509	55	1680	304	31
As-quenched	5.396	34.79	104.9	0.3507	0	1700	309	110

In figure 3.4(a) and 3.4(b) we plot K_Q vs. G and ΔH respectively. The fracture toughness of the relaxed samples varies very systematically with both G and ΔH, displaying a near linear relationship. A linear fit to the K_Q vs. G data reveals a slope of -37.1 MPa·m$^{1/2}$/GPa, suggesting that for each gigapascal the shear modulus is lowered, the fracture toughness is increased by ~37 MPa·m$^{1/2}$. A linear fit to the K_Q vs. ΔH data reveals a slope of -0.13 MPa·m$^{1/2}$·mol/J and implies that for each 100 J/mol the configurational enthalpy is increased, the fracture toughness is increased by ~13 MPa·m$^{1/2}$. On the other hand, the fracture toughness values corresponding to the as-quenched samples display no correlating tendency with either G or ΔH. In fact, none of the measured properties listed in table 3.1 had any correlating tendency with the fracture toughness of the as-quenched glass. We plot K_Q vs. bulk modulus B and Poisson ratio v in appendix B to show that there is indeed no correlating tendency for even the often used Poisson ratio [20] for the as-quenched samples.

To exemplify the effect of disorder on toughness, we focus on the relaxed sample displaying a shear modulus of ~35 GPa and recovered enthalpy of ~110 J/mol, as these values roughly compare to the G and ΔH values of the as-quenched samples (excluding the outlying as-quenched data). The near equivalent shear modulus of ~35 GPa and recovered enthalpy of ~110 J/mol between the relaxed and as-quenched samples implies a near equivalent fictive temperature for all samples, which appears to be ~345 °C from figures 3.1(a) and 3.1(b). One would reasonably expect that since all samples, as-quenched or relaxed, have about the same glass configurational state, as evidenced by the near equivalent average configurational properties, they should exhibit about the same fracture toughness. However, fracture toughness varies enormously between these samples. The as-quenched samples demonstrate a fracture toughness ranging between 31 and 110 MPa·m$^{1/2}$, with an average of 75 MPa·m$^{1/2}$ and variance of 35 MPa·m$^{1/2}$. The relaxed sample demonstrates a fracture toughness of 74 MPa·m$^{1/2}$, which is very close to the average value of the as-quenched specimens. The very large variance in the toughness between samples cannot be explained by the presence of oxygen, impurities, or inclusions in some of the samples and absence in others, or by compositional variance or any kind of gradients along the centerline of the cast rods. The as-quenched samples with K_Q of 31, 62 and 96 MPa·m$^{1/2}$ were extracted from the same cast rod (top, bottom and middle segments of the rod respectively), while the as-quenched sample with K_Q of 110 MPa·m$^{1/2}$ and the relaxed sample with K_Q of 74 MPa·m$^{1/2}$ were each extracted from a different rod (bottom and top segments of the rods respectively). Moreover, the EDS analysis verifies a chemical homogeneity across samples, while the absence of any visible cleavage fracture region in the fractography of the samples (particularly the brittle ones) precludes any significant influence by inclusions.

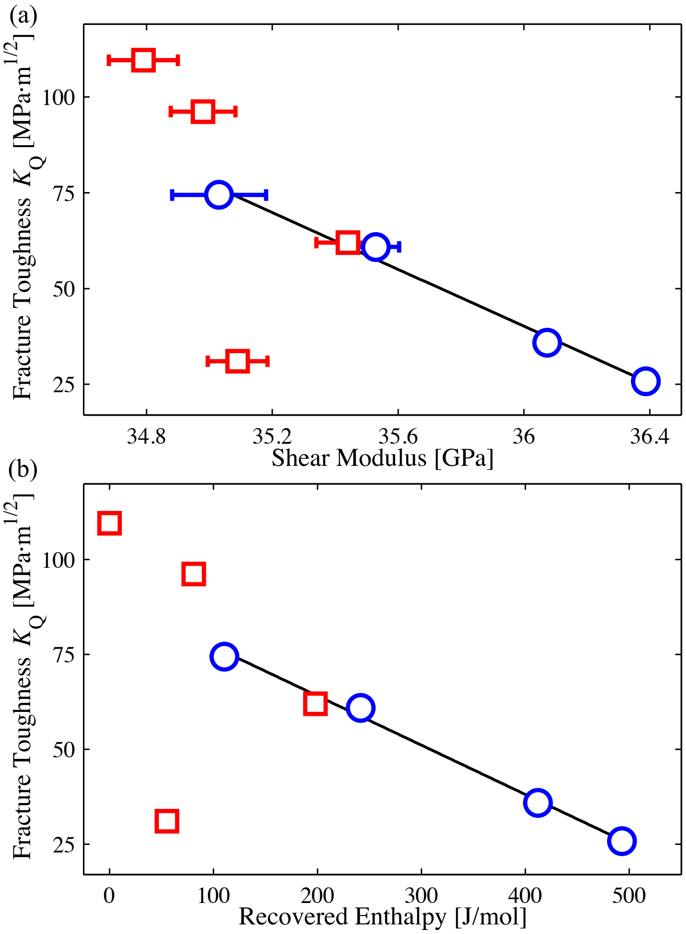

Figure 3.4 (a) Fracture toughness K_{Q} vs. shear modulus G (with associated measurement error) and (b) fracture toughness K_{Q} vs. recovered enthalpy ΔH for equilibrated (blue circles) and as-quenched (red circles) $Zr_{35}Ti_{30}Cu_{8.25}Be_{26.75}$ samples. The lines are linear fits through the data for the equilibrated samples.

The broad toughness variance in that as-quenched state and the lack of any correlating tendency between K_Q and G or ΔH lends support to the concept that a large configurational disorder dominates the fracture process in the as-quenched state. Fracture is not a global process but a local one, and can be sensitive to length scales that could be as small as the glass short-range order. Specifically, the rate of extension of a pre-existing crack, whose tip is essentially atomically sharp, could be heavily influenced by the compliance of the local shear transformation zones (STZs) in the immediate vicinity of the crack tip. As recently revealed by means of acoustic force atomic microscopy, the variance in the STZ moduli in the as-quenched state is expected to be rather large [21]. A large configurational disorder increases the probability that the majority of configurational fluctuations in the immediate vicinity of an existing precrack could either be highly susceptible to shear transformation, or highly resistant to it, giving rise to a non-unique fracture resistance associated with a given average glass configuration. This is because the crack tip is essentially a one dimensional line traversing the sample across its width, and the distribution of the STZ environment ahead of the crack tip would not necessarily be representative of the bulk sample. If the distribution in the bulk sample is rather broad, the local distribution in the crack tip environment can be skewed either towards softer or harder STZs. Soft and highly compliant STZs would encourage plastic rearrangement ahead of the crack tip, suppressing fracture instability and promoting stable crack growth. Hard and stiff STZs would give rise to large and highly localized stresses ahead of the crack tip, promoting fracture instability and leading to unstable crack growth. Therefore, the large variance in STZ modulus in the as-quenched state could produce a fracture toughness that may be considerably higher or considerably lower than the mean. By equilibrating the glass to a well-defined configurational state, the frozen-in STZ configurations that are largely responsible for the large configurational disorder are allowed to relax, thereby narrowing the modulus variance. The resistance to crack propagation is then influenced by a local STZ environment that is likely representative of the bulk material, and as such, the fracture toughness is determined by the mean configurational properties rather than dominated by their variance. Accordingly, the toughness of a relaxed glass correlates strongly with the average configurational state variables (i.e., G and ΔH), and the fracture process becomes more deterministic and more predictable.

In addition, it would be instructive to focus on the origin of the large configurational disorder in an as-quenched glass as compared to a glass relaxed at an equivalent fictive temperature. From an equilibrium thermodynamics consideration, two glasses that fall out of equilibrium at the same temperature and pressure should exhibit essentially identical configurational properties distributed over approximately the same mean and variance. However, by considering kinetics, which are dominant during dynamic vitrification of a glass, and recognizing that the glass vitrification process evolves over a spectrum of fluctuations rather than by a single fluctuational event, one can reasonably expect a rather large degree of disorder in an as-quenched glass. A relaxation map of a typical metallic glass is shown in figure 3.5 [22,23]. A schematic exemplifying the spectrum of relaxations over a range of frequencies at constant temperature is presented in figure 3.5(a), and one showing the spectrum of relaxations over a range of temperatures at constant frequency is presented in figure 3.5(b). The quenching of a high temperature melt is a highly dynamic process occurring over a range of temperatures and frequencies, instead of a unique temperature and frequency. Hence, it is conceivable that a spectrum of unrelaxed modes would be captured during such a dynamic process, including fast modes (some of which may be β modes) captured at lower temperatures and higher frequencies, and slow modes captured at higher temperatures and lower frequencies. Ahead of a stressed crack tip, those fast modes would act as the more compliant modes that encourage plastic rearrangement and stable crack growth, while the slow modes would act as the stiffer modes that promote fracture instability and unstable crack growth. In contrast, when

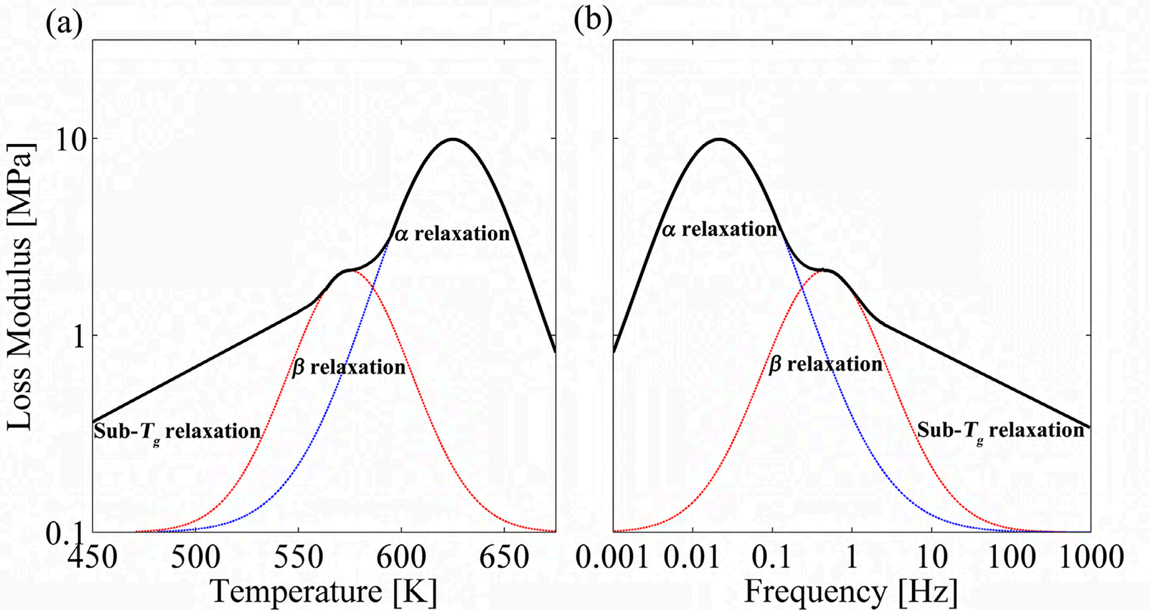

Figure 3.5 Relaxation map of a typical metallic glass [22,23]. (a) Loss modulus vs. frequency at constant temperature; (b) Loss modulus vs. temperature at constant frequency. Approximate distributions for the slow α modes, fast β modes, and ultra-fast sub-T_g modes are designated.

relaxing an as-quenched glass to an equilibrium state of equivalent potential energy, the relaxation process occurs at a well-defined temperature and essentially zero frequency. As such, the slower modes captured at higher temperatures and the faster modes captured at higher frequencies would relax, leading to a significantly narrower equilibrium distribution of unrelaxed modes captured in the relaxed glass. Consequently, a relaxed glass would be spatially more homogeneous at the length scale of its short-range order, such that it would exhibit a more deterministic and more predictable fracture resistance.

Aside from demonstrating that relaxation of the metallic glass to a well-defined configurational state leads to a predictable and reliable toughness, the present results further elucidate the underlying thermodynamics controlling toughness and point to interesting technological implications. As we noted earlier, figure 3.4(b) reveals that increasing the configurational enthalpy of a relaxed sample linearly increases toughness at a ratio of 13 $\mathrm{MPa \cdot m^{1/2}}$ per 100 J/mol. Although it is not evident from figure 3.4(b) that the increase in toughness with configurational enthalpy will remain linear at very high ΔH values rather than saturating at some limiting value, one can envision increasing the configurational enthalpy of a metallic glass by many kJ/mol and gaining substantial toughness on the order of hundreds of $\mathrm{MPa \cdot m^{1/2}}$. Conventional thermal annealing treatments are limited by an inability to freeze in the high temperature configurational state because of either intervening crystallization or the relaxation rate becoming higher than the quench rate. However, if large increases in the configurational enthalpy of a relaxed sample can be translated into large gains in toughness, as figure 3.4(b) suggests, the technological implications could be of great engineering interest. In figure 3.6 we present a performance map of toughness vs. strength (Ashby map) showing the strength and toughness relationship of metallic glasses alongside conventional engineering metals. The toughness and strength data obtained for the four relaxed states in this work are superimposed on the plot (the arrow points in the direction of increasing configurational enthalpy). As seen in the plot, a potential for very high toughness exists for metallic glasses that could attain very high configurational enthalpies, perhaps far surpassing the benchmark toughness values achieved by the toughest engineering metals known.

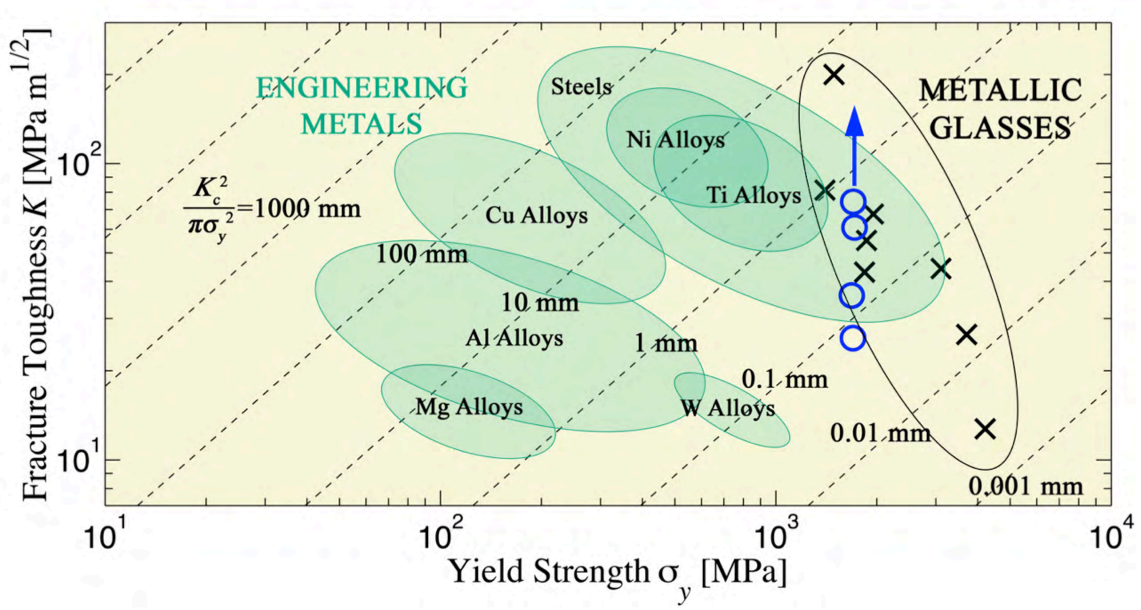

Figure 3.6 Ashby map of fracture toughness K_Q vs. yield strength σ_y in the damage tolerance range of engineering alloys. The green shaded ovals represent common crystalline engineering metals [24] and the black oval represents metallic glasses. The black crosses are metallic glasses taken from Demetriou et al. [1]. The blue circles are the annealed $Zr_{35}Ti_{30}Cu_{8.25}Be_{26.75}$ samples from this letter. The blue arrow indicates the increase in damage tolerance made possible by further increasing the configurational enthalpy of the metallic glass.

BIBLIOGRAPHY

[1] M. D. Demetriou, M. E. Launey, G. Garrett, J. P. Schramm, D. C. Hofmann, W. L. Johnson, and R. O. Ritchie, Nat Mater **10**, 123 (2011).

[2] R. O. Ritchie, Nat Mater **10**, 817 (2011).

[3] X. J. Gu, S. J. Poon, G. J. Shiflet, and J. J. Lewandowski, Acta Mater **58**, 1708 (2010).

[4] P. A. Hess, S. J. Poon, G. J. Shiflet, and R. H. Dauskardt, Journal of Materials Research **20**, 783 (2005).

[5] A. Kawashima, H. Kurishita, H. Kimura, and T. Zhang, Materials Transactions **46**, 1725 (2005).

[6] J. H. Schneibel, J. A. Horton, and P. R. Munroe, Metall and Mat Trans A **32**, 2819 (2001).

[7] A. Shamimi Nouri, X. J. Gu, S. J. Poon, G. J. Shiflet, and J. J. Lewandowski, Philosophical Magazine Letters **88**, 853 (2008).

[8] S. V. Madge, D. V. Louzguine-Luzgin, J. J. Lewandowski, and A. L. Greer, Acta Mater **60**, 4800 (2012).

[9] J.-Y. Suh, R. D. Conner, C. P. Kim, M. D. Demetriou, and W. L. Johnson, Journal of Materials Research **25**, 982 (2010).

[10] H. Kimura and T. Masumoto, Acta Metallurgica **28**, 1677 (1980).

[11] J. J. Lewandowski, Materials Transactions **42**, 633 (2001).

[12] M. D. Demetriou, J. S. Harmon, M. Tao, G. Duan, K. Samwer, and W. L. Johnson, Phys Rev Lett **97**, (2006).

[13] C. Rycroft and E. Bouchbinder, Phys Rev Lett **109**, 194301 (2012).

[14] *ASTM Standard E399* (ASTM International, West Conshohocken, PA, 2012).

[15] *ASTM Standard C693*, 2008 ed. (ASTM International, West Conshohocken, PA, 2008).

[16] G. Duan, A. Wiest, M. L. Lind, J. Li, W.-K. Rhim, and W. L. Johnson, Adv Mater **19**, 4272 (2007).

[17] M. L. Lind, G. Duan, and W. L. Johnson, Phys Rev Lett **97**, 015501 (2006).

[18] W. L. Johnson, M. D. Demetriou, J. S. Harmon, M. L. Lind, and K. Samwer, Mrs Bull **32**, 644 (2007).

[19] J. S. Harmon, M. D. Demetriou, W. L. Johnson, and K. Samwer, Phys Rev Lett **99**, (2007).

[20] J. J. Lewandowski, W. H. Wang, and A. L. Greer, Philosophical Magazine Letters **85**, 77 (2005).

[21] H. Wagner, D. Bedorf, S. Kuechemann, M. Schwabe, B. Zhang, W. Arnold, and K. Samwer, Nat Mater **10**, 439 (2011).

[22] K. L. Ngai, *Relaxation and Diffusion in Complex Systems* (Springer New York, New York, NY, 2011).

[23] H. B. Yu, K. Samwer, Y. Wu, and W. H. Wang, Phys Rev Lett **109**, 095508 (2012).

[24] M. F. Ashby, *Materials Selection in Mechanical Design* (Pergamon Press, Oxford; New York, 1992).

Chapter 4

EFFECT OF MICROALLOYING ON THE TOUGHNESS OF METALLIC GLASSES

ABSTRACT

The effect of microalloying on the toughness of Cu-Ti-based metallic glasses is explored. Minor additions of Si and Sn in glass former $Cu_{47}Ti_{34}Zr_{11}Ni_8$ known to improve glass-forming ability are found here to sharply decrease toughness. The drop in toughness is associated with a small but meaningful increase in shear modulus, glass transition temperature, yield strength, and a decrease in Poisson's ratio; implying a negative correlation between toughness and shear flow barrier. The strong influence of minor additions on the glass properties could be a useful tool for simultaneously tuning both the glass-forming ability and toughness of metallic glasses.

INTRODUCTION

The addition of minority elements, or microalloying, has a long history in metallurgical applications and is well practiced in the field of metallic glass research [1]. Minor additions are used to increase strength, thermal stability, glass-forming ability (GFA), corrosion resistance, magnetic properties, and plasticity [2]. Dramatic changes in properties can be achieved with additions of 1% to 2%, but significant changes are not uncommon with additions of less than 1% [3,4]. Such minute changes in alloy composition are not enough to change the chemistry or electronic structure of the glass-forming liquid, but leads to a dramatic change in global properties nonetheless. Recent work suggests that these large changes from minor additions occur because of an alteration in the medium-range order of the liquid that affects the elastic stress distribution [5]. In the present study, we investigate the effects of microalloying on the toughness of metallic glass and the glass properties that influence fracture resistance.

The GFA of $Cu_{47}Ti_{34}Zr_{11}Ni_8$, first reported by Lin and Johnson [6] as a marginal glass former, has been improved through various microalloying additions [7-14]. Motivated by recent work on the amorphous $Fe_{80}P_{12.5}C_{7.5}$ system [15], which revealed that toughness degraded as GFA improved through alloying additions of 2% to 5%, we investigate here the effects of microalloying (additions of 1% to 2%) on the toughness of fully amorphous $Cu_{47}Ti_{34}Zr_{11}Ni_8$. The microalloying compositions considered here were $Cu_{47}Ti_{33}Zr_{11}Ni_8Si_1$ [7] and $Cu_{47}Ti_{33}Zr_{11}Ni_6Si_1Sn_2$ [8]. The effect of microalloying on fracture resistance is assessed by measuring the thermodynamic properties, elastic constants, yield strength, hardness, and notch toughness of fully amorphous 3 mm diameter rods of $Cu_{47}Ti_{34}Zr_{11}Ni_8$, $Cu_{47}Ti_{33}Zr_{11}Ni_8Si_1$, and $Cu_{47}Ti_{33}Zr_{11}Ni_6Si_1Sn_2$.

SAMPLE PREPARATION AND CHARACTERIZATION

Ingots of $Cu_{47}Ti_{34}Zr_{11}Ni_8$, $Cu_{47}Ti_{33}Zr_{11}Ni_8Si_1$, and $Cu_{47}Ti_{33}Zr_{11}Ni_6Si_1Sn_2$ were prepared using appropriate amounts of Cu (99.999%), Ti (99.99%), Zr (99.92%), Ni (99.995%), Si (99.9999%), and Sn (99.99%). Each ingot was arc melted in a Ti-gettered Argon atmosphere on a water-cooled copper hearth, and flipped at least four times to ensure chemical homogeneity. For the two alloys containing Si, the Si was prealloyed with Cu prior to alloying the rest of the elements [7]. Rods of 3 mm diameter and 35 mm length were cast in a copper mold by injecting from the molten liquid state under a high purity Argon atmosphere using radio frequency induction power for heating. The temperature of the melt prior to injection, monitored with a LAND System 4 pyrometer, was ~1150 °C. Rods of 3 mm in diameter and 30 mm in length were also produced by suction casting in a copper mold using an Edmund Bühler compact arc melter.

The amorphous structure of the rods was verified by X-ray diffraction (XRD) with a Panalytical X'Pert Pro X-ray diffractometer using Cu K_α radiation. The XRD scans, which are shown in figure 4.1, display the archetypal amorphous hump. We also performed differential scanning calorimetry (DSC) from room temperature through the end of crystallization using a Netzsch Pegasus 404C DSC at a scanning rate of $0.33\ °C\cdot s^{-1}$. The DSC scans are shown in figure 4.2, where the arrows denote the glass transition temperature T_g and the crystallization temperature T_x. As minorities of Si and Sn are substituted in to the original composition $Cu_{47}Ti_{34}Zr_{11}Ni_8$, T_g increases from 408 °C to 414 °C to 424 °C, T_x from 451 °C to 468 °C to 487 °C, and ΔT, the difference between T_g and T_x, increases from 43 °C to 54 °C to 63 °C. The ΔT quantity is a measure of the stability against crystallization for the supercooled liquid, and in certain systems was found to correlate well with glass-forming ability.

The elastic constants were calculated from the shear sound speed, longitudinal sound speed, and the density ρ. The sound speeds were collected using the pulse-echo overlap technique with 25 MHz piezoelectric transducers, and ρ was measured via the American Society for Testing and Materials ASTM C693 Archimedes method [16]. The 0.5 kgf HV scale Vickers hardness was measured with a Wilson Instruments 402MVD Microhardness Tester. The compressive yield strength was determined using 3 mm diameter and 6 mm tall plane parallel cylinders in an Instron 5500R load frame at a 10^{-3} s^{-1} strain rate. The values for all measured properties are listed in table 4.1. As seen in table 4.1, the increase in d_c promoted by minority substitutions of Si and Sn is associated with an increase in the density ρ, shear modulus G, yield strength σ_y, and Vickers hardness $HV0.5$.

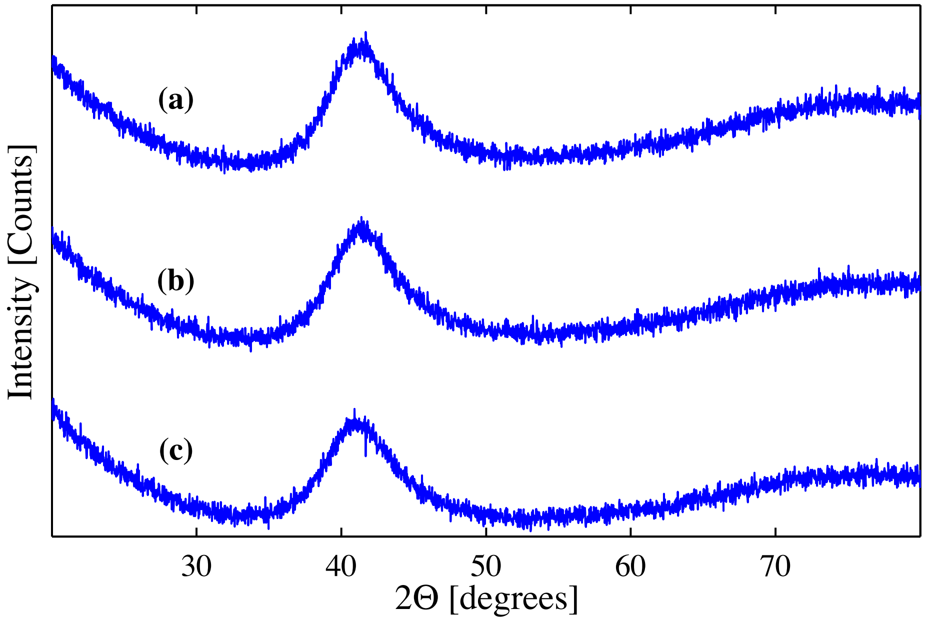

Figure 4.1 X-ray diffraction patterns from the cross-sections of 3 mm diameter rods of (a) $Cu_{47}Ti_{34}Zr_{11}Ni_8$, (b) $Cu_{47}Ti_{33}Zr_{11}Ni_8Si_1$, and (c) $Cu_{47}Ti_{33}Zr_{11}Ni_6Si_1Sn_2$.

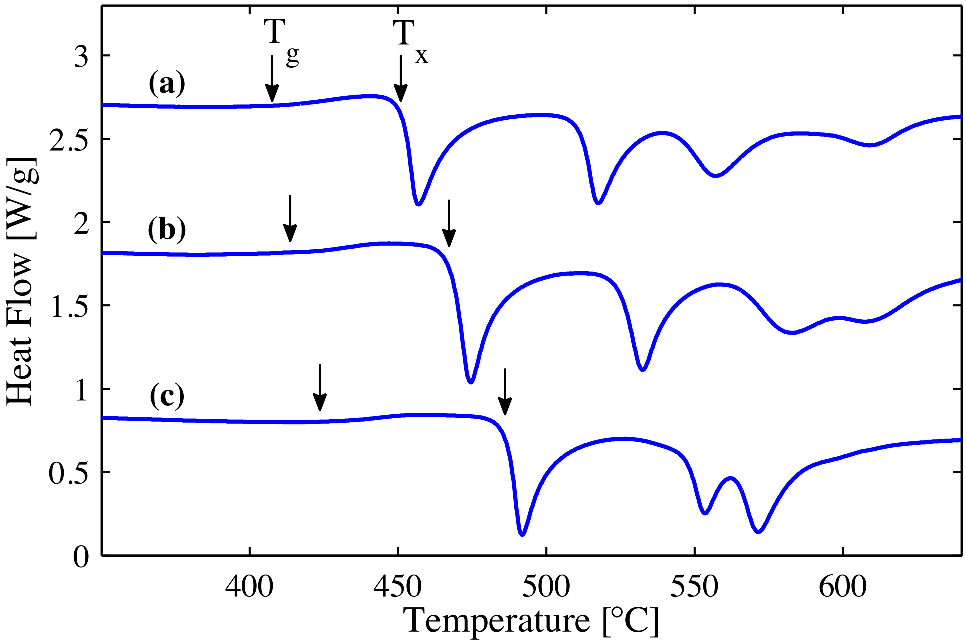

Figure 4.2 Differential calorimetry scans at a rate of 20 °C min^{-1} for (a) $Cu_{47}Ti_{34}Zr_{11}Ni_8$, (b) $Cu_{47}Ti_{33}Zr_{11}Ni_8Si_1$, and (c) $Cu_{47}Ti_{33}Zr_{11}Ni_6Si_1Sn_2$. Arrows designate T_g and T_x.

NOTCH TOUGHNESS TESTING

Cast rods were prepared for notch toughness by cutting a notch through a third of the diameter with a wire saw of 120 μm notch root radius. The notched rods were placed in a three-point bending setup with a span distance of 12.7 mm and loaded at a constant crosshead displacement rate of 0.001 $\mathrm{mm \cdot s^{-1}}$. The critical fracture load was recorded and used to calculate the stress intensity factor K_Q. The analysis by Murakami for the bending of a cylinder with a straight line notch was employed to accommodate the sample geometry [17]. At least five and up to nine conditional K_Q measurements were performed for each alloy; the averages and standard deviations are shown in table 4.1. In contrast to the glass-forming ability, the toughness K_Q decreases as Si and Sn are introduced in to the alloy. We note that ASTM E399 states that for a linear-elastic fracture toughness value to be plane strain $K_{IC,}$ the out-of-plane thickness dimension B must be greater than or equal to $2.5(K_Q/\sigma_y)^2$ [18]. If this specimen thickness constraint is not met, the fracture might take place under partial or full plane stress conditions that can result in an overestimation of the fracture toughness [18]. The effect of plane-stress conditions on the measured toughness of metallic glasses was studied in detail by Kawashima et al. [19]. Due to a relatively high toughness and moderate yield strength of the present alloys, only the more brittle $Cu_{47}Ti_{33}Zr_{11}Ni_6Si_1Sn_2$ alloy meets this plane-strain constraint. The sample thickness required for linear-elastic plane-strain measurements of $Cu_{47}Ti_{34}Zr_{11}Ni_8$ and $Cu_{47}Ti_{33}Zr_{11}Ni_8Si_1$ is 7.4 mm and 5.4 mm, respectively, both above the critical casting diameter of the alloys, thereby necessitating the use of different measuring techniques [4]. Nonetheless, the transition to plane-stress conditions on going from $Cu_{47}Ti_{33}Zr_{11}Ni_6Si_1Sn_2$

to $Cu_{47}Ti_{33}Zr_{11}Ni_8Si_1$ and $Cu_{47}Ti_{34}Zr_{11}Ni_8$ is a direct consequence of increasing alloy toughness, which in essence corroborates the toughness trend between the alloys. The plastic zone radius r_p can be estimated from $r_p = K_Q^2/(\pi\sigma_y^2)$, which starts at 940 μm for $Cu_{47}Ti_{34}Zr_{11}Ni_8$, decreases to 690 μm for $Cu_{47}Ti_{33}Zr_{11}Ni_8Si_1$, and drops to 240 μm for $Cu_{47}Ti_{33}Zr_{11}Ni_6Si_1Sn_2$.

FRACTURE SURFACES AND TOUGHNESS CORRELATIONS

Images of the fracture surface were taken with a LEO 1550VP field emission scanning electron microscope. Each fracture surface can be broken down in to four regions, listed in the direction of fracture propagation, from the top of the image to the bottom: (1) the notch made by the wire saw, (2) the smooth "shear lip" surface associated with the sliding of the initiating shear band, (3) the jagged "rough zone" associated with the proliferation of plasticity by shear band networking, and (4) the smooth fast-fracture region associated with cavitation and catastrophic crack opening. The length of the notch is required to be between one third and one half of the cylinder diameter; the proportions of the other three zones vary with the alloy's resistance to fracture. The mechanism of toughness in metallic glasses arises from blunting propagating cracks by plastic shear-band sliding at the crack tip, and is generally reflected by the roughness of the fracture surface [20]. As shear bands multiply in number and grow in length from the notch, they produce

Table 4.1 The atomic composition, critical rod diameter d_c, glass transition temperature T_g, density ρ, yield strength σ_y, 0.5 kgf scale Vickers hardness *HV*0.5, bulk modulus *B*, shear modulus *G*, Poisson's ratio *ν*, and notch toughness K_Q for $Cu_{47}Ti_{34}Zr_{11}Ni_8$, $Cu_{47}Ti_{33}Zr_{11}Ni_8Si_1$, and $Cu_{47}Ti_{33}Zr_{11}Ni_6Si_1Sn_2$.

Composition [at%]	d_c [mm]	T_g [°C]	ρ [g/cm^3]	σ_y [MPa]	$HV0.5$ [kgf · mm^2]	B [GPa]	G [GPa]	ν [–]	K_Q [MPa · m$^{1/2}$]
$Cu_{47}Ti_{34}Zr_{11}Ni_8$	4[a]	408	6.818 ± 0.015	1902	581.4 ± 5.5	126.4 ± 0.04	37.21 ± 0.09	0.3660 ± 0.0005	103.4 ± 8.2
$Cu_{47}Ti_{33}Zr_{11}Ni_8Si_1$	7[b],4[c,d]	414	6.838 ± 0.014	1960	585.3 ± 4.4	127.6 ± 0.04	38.66 ± 0.08	0.3624 ± 0.0006	90.92 ± 5.42
$Cu_{47}Ti_{33}Zr_{11}Ni_6Si_1Sn_2$	6[c,e]	424	6.867 ± 0.010	2000	592.2 ± 4.3	126.1 ± 0.03	39.39 ± 0.06	0.3585 ± 0.0004	54.84 ± 4.67

[a] Reference [6]

[b] Reference [7]

[c] Reference [8]

[d] Reference [14]

[e] Reference [13]

multiple shear offsets that result in the jagged surface of the plasticity regime that follows the initial sliding regime. Once shear bands reach a critical sliding strain, cavitation and crack opening take over, transforming the shear band in to an emerging crack. If the emerging crack cannot be arrested by continued shear banding ahead of the propagating crack tip, as happens in most metallic glasses, catastrophic dimpled fracture is promoted. Thus, the longer the initial shear bands at the notch root and the longer the rough zone, the tougher the glass would be. Comparing the fracture surface of the tougher $Cu_{47}Ti_{34}Zr_{11}Ni_8$ figure 4.3(a) with the increasingly less tough $Cu_{47}Ti_{33}Zr_{11}Ni_8Si_1$ figure 4.3(b) and $Cu_{47}Ti_{33}Zr_{11}Ni_6Si_1Sn_2$ figure 4.3(c), we see that the initial shear offset length decreases, the rough zone length decreases, and the fast fracture zone length increases as toughness decreases.

Inspection of the fracture surfaces suggests that toughness is a result of the interplay between the shear sliding process and the cavitation process. We can investigate this further and correlate the average properties of the glass structure with its toughness to see how microalloying can have such a dramatic influence on toughness. In figure 4.4 we plot the notch toughness K_Q vs. (a) T_g, (b) σ_y, (c) G, and (d) ν. The negative correlation of K_Q with T_g, σ_y, and G agrees with previous studies [15], and arises from the increase in the barrier height for shear flow [21]. The positive correlation between K_Q and ν also agrees with previous studies [22], and is explained by how ν quantitatively describes the ratio of the cavitation barrier to the shear flow barrier. From table 4.1, as Si and Sn are substituted in, the shear modulus is raised by just 2% to 4% with each substitution, while the bulk modulus remains roughly constant, resulting in a slight but meaningful drop in ν. These seemingly minor shifts in the elastic constants are indicative of significant structural rearrangements in the atomic structure of the glass that dramatically influence the fracture resistance.

Microalloying in the present work, as well as somewhat larger alloying additions in previous work [15], are shown to sharply decrease toughness by slightly increasing the shear flow barrier; reflected in the negative correlation between toughness and shear modulus, glass transition temperature, and yield strength (and the positive correlation with Poisson's ratio). However, as shown in another recent study [5], microalloying can improve glass-forming ability while also dramatically improving toughness. This has been accomplished by increasing the barrier for shear flow while also increasing the cavitation barrier even further, resulting in an overall larger shear sliding capacity prior to fracture. One may therefore conclude that microalloying is a powerful instrument that can strongly and positively influence not only the glass forming ability but also the toughness of metallic glasses. Hence, understanding and controlling microalloying, as attempted in this work, would be key in optimizing the design of future metallic glass alloys.

Authors would like to acknowledge the Caltech MURF program for undergraduate support.

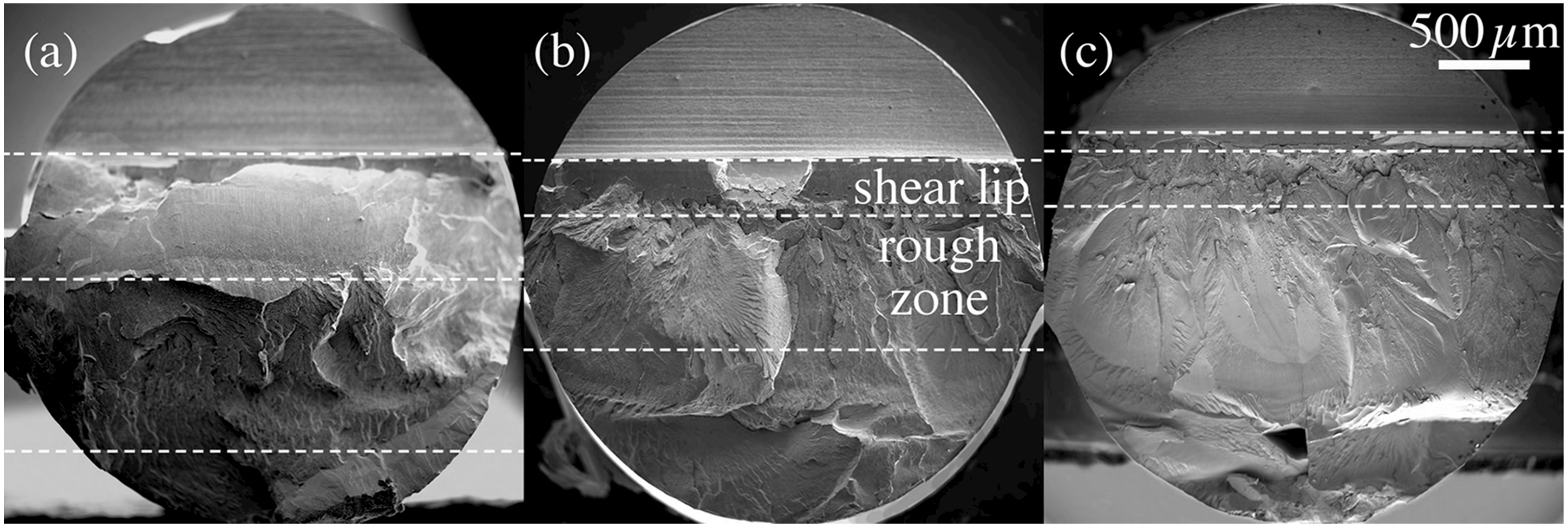

Figure 4.3 Scanning electron micrographs of the notch toughness fracture surfaces from 3 mm diameter rods of (a) $Cu_{47}Ti_{34}Zr_{11}Ni_8$, (b) $Cu_{47}Ti_{33}Zr_{11}Ni_8Si_1$, and (c) $Cu_{47}Ti_{33}Zr_{11}Ni_6Si_1Sn_2$. The separation between the notch, shear lip, rough zone, and fast-fracture regions are delineated by dashed lines for each specimen.

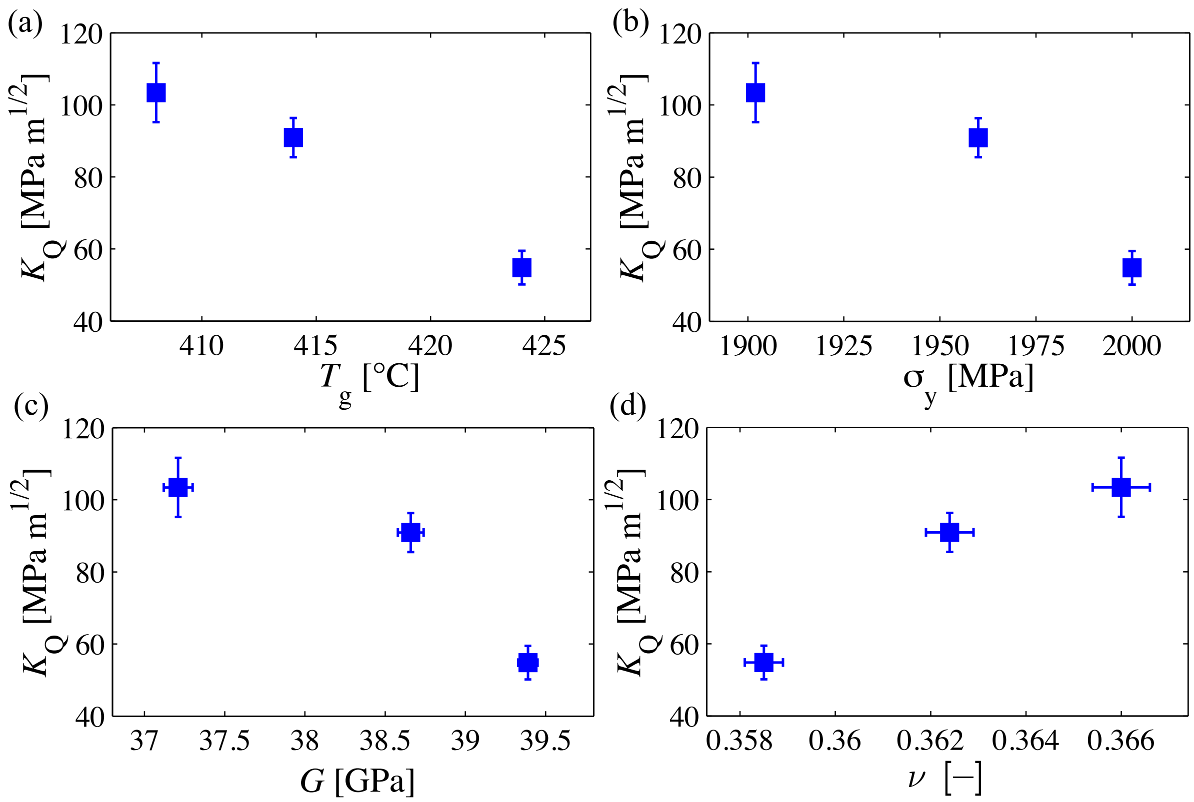

Figure 4.4 Notch toughness K_Q vs. (a) glass transition temperature T_g, (b) yield strength σ_y, (c) shear modulus G, and (d) Poisson's ratio ν for $Cu_{47}Ti_{34}Zr_{11}Ni_8$ (largest K_Q), $Cu_{47}Ti_{33}Zr_{11}Ni_8Si_1$ (middle K_Q), and $Cu_{47}Ti_{33}Zr_{11}Ni_6Si_1Sn_2$ (smallest K_Q).

BIBLIOGRAPHY

[1] Z. Lu and C. Liu, J Mater Sci **39**, 3965 (2004).

[2] W. H. Wang, Progress in Materials Science **52**, 540 (2007).

[3] M. D. Demetriou, M. Floyd, C. Crewdson, J. P. Schramm, G. Garrett, and W. L. Johnson, Scripta Materialia **65**, 799 (2011).

[4] M. D. Demetriou, M. E. Launey, G. Garrett, J. P. Schramm, D. C. Hofmann, W. L. Johnson, and R. O. Ritchie, Nat Mater **10**, 123 (2011).

[5] S. M. Chathoth, B. Damaschke, J. P. Embs, and K. Samwer, Appl Phys Lett **95**, 191907 (2009).

[6] X. Lin and W. Johnson, J Appl Phys **78**, 6514 (1995).

[7] H. Choi-Yim, R. Busch, and W. Johnson, J Appl Phys **83**, 7993 (1998).

[8] E. Park, H. Lim, W. Kim, and D. Kim, J Non-Cryst Solids **298**, 15 (2002).

[9] E. Park, D. Kim, T. Ohkubo, and K. Hono, J Non-Cryst Solids **351**, 1232 (2005).

[10] M. Calin and J. Eckert, Adv. Eng. Mater. **7**, 960 (2005).

[11] M. Calin, M. Stoica, J. Eckert, A. R. Yavari, and L. Schultz, Materials Science and Engineering: A **392**, 169 (2005).

[12] E. S. Park, H. J. Chang, J. S. Kyeong, and D. H. Kim, Journal of Materials Research **23**, 1995 (2008).

[13] E. S. Park, H. J. Chang, and D. H. Kim, Journal of Alloys and Compounds **504, Supplement 1**, S27 (2010).

[14] S. Venkataraman, M. Stoica, S. Scudino, T. Gemming, C. Mickel, U. Kunz, K. B. Kim, L. Schultz, and J. Eckert, Scripta Materialia **54**, 835 (2006).

[15] M. D. Demetriou, G. Kaltenboeck, J.-Y. Suh, G. Garrett, M. Floyd, C. Crewdson, D. C. Hofmann, H. Kozachkov, A. Wiest, J. P. Schramm, and W. L. Johnson, Appl Phys Lett **95**, 041907 (2009).

[16] *ASTM Standard C693*, 2008 ed. (ASTM International, West Conshohocken, PA, 2008).

[17] Y. Murakami, *Stress Intensity Factors Handbook*, 1st ed. (Pergamon, Oxford, United Kingdom, 1987).

[18] *ASTM Standard E399* (ASTM International, West Conshohocken, PA, 2012).

[19] A. Kawashima, H. Kurishita, H. Kimura, and T. Zhang, Materials Transactions **46**, 1725 (2005).

[20] J.-Y. Suh, R. D. Conner, C. P. Kim, M. D. Demetriou, and W. L. Johnson, Journal of Materials Research **25**, 982 (2010).

[21] W. L. Johnson, M. D. Demetriou, J. S. Harmon, M. L. Lind, and K. Samwer, Mrs Bull **32**, 644 (2007).

[22] J. J. Lewandowski, W. H. Wang, and A. L. Greer, Philosophical Magazine Letters **85**, 77 (2005).

Chapter 5

INVESTIGATION OF CAVITATION IN GLASS-FORMING LIQUIDS

ABSTRACT

In an effort to better understand the source of toughness in metallic glass, we have investigated cavitation in glass-forming liquids. When subjected to negative hydrostatic pressure, a liquid will reduce its energy through the formation of a cavity. This phenomenon is the competing process to shear band growth and the development of a large plastic zone, which we have identified as the crucial parameter for the wider adoption of metallic glass as an engineering material. We report the homogeneous and heterogeneous nucleation of cavities in $Zr_{41.2}Cu_{12.5}Ti_{13.8}Be_{22.5}Ni_{10}$ (Vitreloy 1) liquid by the application of a critical negative pressure. For homogeneous nucleation, we estimate a critical negative pressure of less than 500 MPa at a temperature of roughly 1000 ºC and a timescale of ~7 s. The heterogeneous nucleation of cavities is observed and is estimated to take place at much smaller negative pressures, thus an important finding as this easy pathway to cavitation represents a limiting factor for plastic zone development in metallic glass. When liquid Vitreloy 1 is subjected to a negative pressure less than the critical pressure for homogeneous nucleation on a laboratory timescale of 1 to 7 s and is free of heterogeneous nucleation sites, no cavities are formed. The liquid is thus “metastable” on laboratory timescales with respect to cavitation at these temperatures and estimated negative pressures.

INTRODUCTION

The role of shear banding has been discussed extensively in the shielding of the crack tip by the plastic zone when metallic glass is loaded in mode I fracture conditions [1,2]. This is the sole toughening mechanism in monolithic bulk metallic glass [3]. The Poisson's ratio has been recognized as an important parameter in determining the fracture toughness of a metallic glass [4] as it is a reasonable representation of a glass's ability to promote shear banding before cavitation in the shear band extends the crack further in to the material [1]. Dimpled fracture, a sign of cavitation, has been observed for amorphous metal in loaded both in tension and in bending [5,6]. The fact that a solid can fail by a phenomenon generally reserved for fluids is an important realization. The once-frozen glass inside the shear band is actually now moving in a state of plastic shear flow at an elevated temperature and potential energy [7,8]. Critically, the fluid inside the shear band is also subject to an opening tensile stress. This opening stress is the source of cavitation and crack propagation in metallic glass. Understanding this phenomenon in greater detail would shed light on a crucial aspect of toughness in metallic glass. If the negative pressure at which a cavity nucleates in the liquid could be determined as a function of the liquid temperature, one could predict where cavitation is expected to occur in an operating shear band of a deforming metallic glass. In turn, this would enable more accurate modeling of the fracture toughness of a solid metallic glass under mode I crack opening.

Cavitation cannot be avoided for any fluid that is placed in a state of triaxial tension (negative hydrodynamic pressure) as the liquid is always metastable to cavitation in this stretched state. The intermolecular forces of the fluid can keep it together for some pressure- and temperature-dependent time, but the fluid would always rather decompose in to some vapor and a less stretched fluid [9]. The chemical potential of the gas goes to negative infinity as the molar volume gets large, so the vapor phase is always favored. There is no such thing as gas at a negative pressure as at high molar volumes all gases behave as an ideal gas, which is already so sparse that it does not have the intermolecular forces to resist the pull of a negative pressure.

Molecular dynamics simulations by G. Duan in his thesis [10] established an equation of state for the $Zr_{54}Cu_{46}$ bulk glass-forming liquid. The equations of state established by G. Duan were used by An, Garrett, et al. to calculate the temperature-dependent spinodal pressure of the liquid (the pressure at which the bulk modulus vanishes and the barrier to nucleation of the vapor phase vanishes) [11]. The system was also stretched to various negative pressures and temperatures and allowed to sit for ~1 ns at each pressure and temperature. If the system cavitated within the timescale of the simulation, it was marked as the critical cavitation pressure for that temperature. In this fashion the temperature-dependent cavitation pressure was determined, which was about half the negative pressure of the spinodal pressure. While the strain and sample size are vastly different from the laboratory timescale, it is still interesting to see that the metallic liquid responds to negative pressure in a manner similar to other fluids. Our molecular dynamics work was started just before the experimental work was started, and the molecular dynamics study continued after the experimental work was discontinued. The paper by An, Garrett, et. al. [11] was actually received by its publisher one day before a molecular dynamics study of cavitation by Murali et al. [12] was received by their publisher! They also studied cavitation in binary metallic glasses, and they also find that cavitation is controlled by fluctuations in the glass that will form cavities once they reach a critical size. Their study shows how the fluctuations and their resulting cavitation behavior differ between a brittle and tough glass-forming liquid [12]. It is an interesting study that is motivated by the same curiosity about the origins of toughness in metallic glass as this work. For this chapter, we set out to explore cavitation in bulk glass-forming liquids by placing them in a pure state of negative hydrodynamic pressure (all cross terms in the stress tensor are zero and the trace of the stress tensor is negative). While our primary goal is bulk glass-forming metallic liquids, we also make a brief detour through organic glass formers.

EXPERIMENTAL METHODS

In the molecular dynamics simulations mentioned above, it is trivial to apply a negative hydrostatic pressure. However, in the laboratory, it is much more difficult to apply a pure negative hydrostatic pressure without any additional shear-stress components. Uniaxial tension and bending are the two main methods that apply some opening stress on a material, but none of these methods provides a pure triaxial negative stress on the material. We specifically wanted a pure negative hydrostatic stress placed on a metallic glass-forming liquid. M. L. Lind demonstrated homogeneous cavitation in the liquid of the glass-forming organic molecule glycerol by quenching a fused silica cylinder capped with a copper plug in to a liquid nitrogen bath [13]. This experimental setup creates negative pressure in the liquid inside the container by taking advantage of the difference in the coefficient of thermal expansion between the liquid glycerol and the glassy solid glycerol. The outside of the container is cooled below the glass transition temperature T_g which cools the liquid near the edges of the container first, which results in a solid glassy container with a liquid interior. As this container cools further, the volume of the solid shell shrinks at a rate much slower than the volume of the liquid interior. This difference in volumetric shrinkage puts the solid shell in compression and the liquid interior in triaxial tension without any shear components. The cylindrical container of Lind made it difficult to estimate the pressure at which the glycerol was cavitating, we experimented with different designs of fused silica containers that might allow for better estimation of the pressure. We settled on a spherical geometry that would allow for a near uniform cooling and simple estimation of pressure, we will discuss estimation of pressure later. The final design shown in figure 5.1(a) is a near perfect sphere attached by a thin (2 mm inner diameter) neck to a standard fused silica tube. The thin neck that connected the sphere to the quartz tube is a key design feature that was not well understood at the onset of the experiments. The original design had neck diameters that were much too large and thus the liquid inside the neck did not solidify early enough to prevent reflow of the hot liquid from the upper tube through the neck and in to the sphere. Once the neck diameter was reduced sufficiently, the liquid in the neck solidified quickly in the quench process and mechanically encapsulated the sphere, allowing for proper cavitation experiments with the buildup of negative hydrostatic pressure. The Caltech glass blower custom made each fused silica tube and was integral in the design process. The diameter of the ampule could be varied, but they were always attached with a similarly thin neck to a 10 mm inner diameter and 12 mm outer diameter fused silica tube about 18 inches long. The dimensions of the neck were kept constant at an inner diameter of ~2 mm, an outer diameter of ~4 mm, and a wall thickness of 1 mm to ensure reproducible freezing in the neck.

We unwittingly reinvented a modified Bertholet tube [14]. While the original design operates on the same principle of hot liquid shrinking inside a rigid container, the Bertholet tube was sealed shut at high temperature and then cooled slowly to apply negative pressure. Our design relies on the freezing of the hot liquid inside the neck of the tube to form a solid metallic glass plug that becomes part of the rigid container that mechanically encapsulates the hot liquid center of the sphere. In contrast to the Bertholet method, we are unable to cool our design slowly as our glass-forming liquid would crystallize before cavitation could take place. If the cooling were roughly quasi-static, we could perfectly predict the volume strain and negative pressure from the thermal shrinkage. Since the quenching process is dynamic we can't determine exactly what the negative pressure on the liquid inside the sphere is, but we know that as long as there is liquid above T_g inside a solid sphere, there will be some amount negative pressure built up in the liquid. We employ different diameter ampules and vary the initial temperature T_o to induce different levels of thermal volume strain in the hot liquid. The details of estimating the volume strain and pressure will be handled in the discussion section.

The general guideline for how these cavitation experiments were conducted is as follows. Start by measuring the volume of the fused silica sphere. It is useful to graphically measure the inner and outer diameter of the sphere to estimate volume, but I found that I trusted a direct volumetric measurement much more. Using a fluid that has a low enough surface tension so that it can easily traverse the 2 mm inner diameter neck, it was easy to simply fill the sphere and measure the volume of the fluid directly with a graduated cylinder. Once the volume of the sphere is known, the appropriate mass of metallic glass can be calculated for the experiment. It is best to overfill the sphere by at least 10 to 20% so that the neck between the tube and ampule is completely filled. For both the metallic glass and the organic glass-former, we typically used two heat sources, a hot furnace for preparing the material and filling the sphere, and sometimes a cooler one for equilibrating the filled sphere at the desired temperature for quenching. A high temperature, well above the liquidus temperature, is necessary to obtain a homogeneous melt and bring the liquid to a low enough viscosity to infiltrate the neck of the sphere. The organic glass-formers must only be heated ~100 ºC above its glass transition temperature, or to the boiling point of water (to remove absorbed water that could act as heterogeneous nucleation sites), whichever temperature is higher.

Once the tube has been filled with cleaned and weighed material it can be placed in the hotter furnace. Vacuum can be applied to aid with degassing or dehydrating. When the material has stopped bubbling, the vacuum is removed and the sphere is given a moderate overpressure of 5 to 20 psi. Gently tapping the tube can help the process, but it is common to repeat the vacuum and overpressure cycle four or more times to completely fill the sphere. The full sphere is then allowed to sit under vacuum for two minutes to make sure any small bubble can rise up through the neck and our of the sphere. When complete, the sphere is brought to atmospheric pressure or slight overpressure of a few psi before it is transferred to the cooler furnace or bath (if using). After the sphere has equilibrated at the appropriate temperature, the sphere is quickly plunged in to the quench bath to cool the sphere as quickly and evenly as possible below the glass transition temperature of the glass-forming liquid inside. Information about specific intermediate temperature heat sources and quench baths will be included in the results section for each glass-former utilized. Also, during or after quenching, the negative pressure built up on the inside of the sphere is often enough large enough to exceed the compressive strength of the fused silica tube. The fused silica tube would always break gently when quenching the metallic liquids, which did not cause a safety issue, but required one tube for each experiment. The fused silica tube would sometimes survive the quenching of the molecular glass-formers, which could then be reheated and quenched again. However, when the ampules containing the molecular glass-formers did break, they would rupture violently and send glass everywhere; safety was a must.

EARLY RESULTS WITH $Pd_{43}Cu_{27}P_{20}Ni_{10}$, GLYCEROL, AND BORON OXIDE

The $Pd_{43}Cu_{27}P_{20}Ni_{10}$ alloy was the first liquid used in this work. Pd-based glass is an attractive candidate for this experiment because it is an excellent glass former with >1 cm critical casting diameter, and it does not chemically react with our fused silica container. That means it could be recycled and used for many experiments, avoiding the hassle of producing new material for each experiment. Unfortunately, $Pd_{43}Cu_{27}P_{20}Ni_{10}$ also does not wet fused silica, meaning that it prefers to stay closer to itself than the wall of the fused silica container. All cavitation experiments with this Pd-based alloy were quenched from 1000ºC and ended up with samples that closely resembled figure 5.1(b).

We found that if the liquid does not wet the quartz there is no way to evenly remove heat from the outer shell of the liquid on the top of the sphere. The direction of quenching, bottom first, results in the liquid at the bottom of the sphere cooling faster than the liquid at the top of the sphere. Since the liquid does not wet the fused silica, the liquid in the top of the sphere pulls away from the fused silica wall as the liquid in the bottom of the sphere shrinks from cooling. Once any part of the liquid has pulled away from the fused silica wall, that liquid is not in contact with the quench bath and will not vitrify in to a glass. This also prevents the sphere from being mechanically encapsulated. Instead of generating negative pressure in the sphere, the thermal volume strain is expended on growing arge cone-shaped divots that run toward the center of the sphere. These cones are liquid reflow of the last hot liquid left to cool in the sphere; they effectively absorb all the volume strain that should have been produced in the center of the sphere. Because of this we had to abandon Pd-based glasses and explore liquids that wet fused silica.

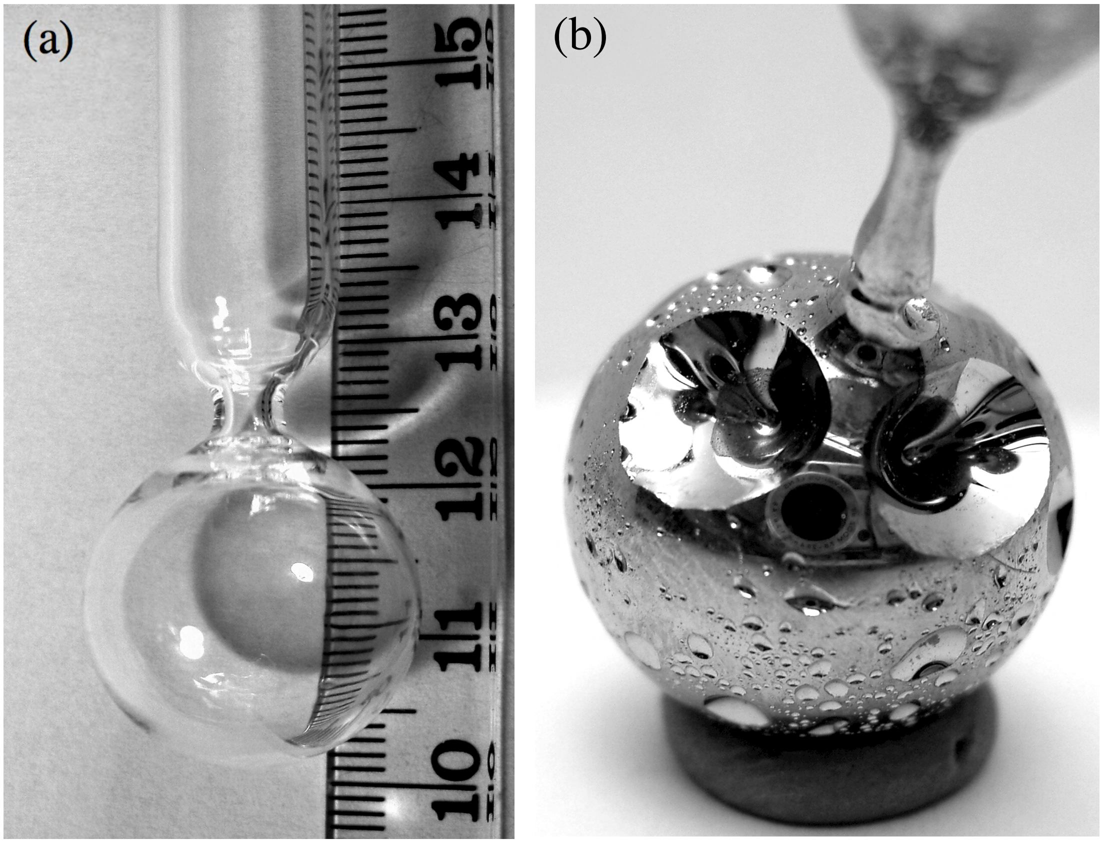

Figure 5.1 (a) The final shape design of fused silica ampule that was used for all experiments in this work. The ampule diameter can be varied but the neck and tube were kept constant. (b) A representative cavitation experiment sample of $Pd_{43}Cu_{27}P_{20}Ni_{10}$ glass displaying how all the volume strain from quenching the hot liquid is absorbed at the top surface of the sphere because the liquid does not wet the fused silica.

While the Pd-based glass did not work out as we hoped, we did experiment with different liquids for thermal transfer in the heat bath. The original quench bath for the Pd-based glass experiments was water, and we though that perhaps the boiling of water during the initial quench from 1000 ºC was preventing effective cooling of the top hemisphere. This initiated a search for an effective heat transfer liquid with a high thermal diffusivity and high boiling point. We eventually decided on a low melting point metal alloy of $Bi_{50}Pb_{26.7}Sn_{13.3}Cd_{10}$ (Wood's metal / Cerrobend) that has a eutectic melting point of 70 ºC, a large density of 9.4 g/cm^3, and a boiling point and thermal diffusivity much higher than that of water. We continued to use this alloy for all metallic glass quench baths as it provided an even and robust quenching.

Once we proved that this container design could produce a thermal volume strain but were continuously frustrated with the performance of the Pd-based glass, we thought it would be fruitful to test molecular glass-formers. Since Dr. M. L. Lind had already demonstrated cavitation in glycerol quenched in liquid nitrogen [13], we attempted to replicate her results. The T_g of glycerol is an extremely low -83 ºC (190 K), necessitating the use of liquid nitrogen as a quench bath, which boils at −196 °C (77 K). The glycerol was brought above 100 ºC for degassing and dehydrating under vacuum, from there it was quenched into a liquid nitrogen bath inside of a double-walled vacuum Dewar with a window so that the cavitation could be viewed *in-situ*. A representative picture from one of these experiments is shown in figure 5.2(a). The initial temperature for the glycerol experiments was varied from 25 ºC to 100 ºC. Every attempt with glycerol resulted in cavitation, preventing us from establishing a critical cavitation pressure. Also, the fused silica tubes did not survive more than a handful of quenches to liquid nitrogen temperatures, prompting the search for a different molecular glass former.

Boron oxide B_2O_3 was being used as a flux for the Pd-based glass, but it is also a strong glass-former that is highly resistant to crystallization. It has a moderate T_g of 263 ºC (563 K) and a melting temperature of 477 ºC (750 K). For boron oxide, the main worry was properly degassing and dehydrating the melt while simultaneously preventing the melt from blowing out of the top of the tube from the massive amounts of bubbling when vacuum was applied. The positive trade-off is that boron oxide is so resistant to crystallization that it can be cooled in air at room temperature instead of quenched in a bath. This was particularly nice as it allowed for video recording of the entire cooling process. To aid in the freezing of the neck, compressed gas was directed at the neck of the tube for an increased cooling rate. Figure 5.2(b) shows a sphere of boron oxide recovered after cavitation. Both the fused silica ampule and boron oxide sphere sample shattered during the experiment. The cavity is filled with modeling clay to better visualize the size of the cavity, which is about 16% of the sphere volume.

Both boron oxide and glycerol were never quenched in a manner where they did not cavitate, so we were unable to establish a critical cavitation pressure. Only a modest amount of time was spent experimenting with the organics, as we really wanted results for a metallic glass-former. However, it was an instructive exercise and a proof of concept for the experiment. We could watch as the cavities form in situ inside the optically transparent organic glass-formers. We confirmed that cavities can nucleate homogeneously in our experimental setup, and that they mainly nucleate in the center of the top hemisphere. This effect is likely caused by the reduced cooling rate in the top of the sphere. Another important observation is that only a single cavity nucleates in any of the spheres. Once one cavity reaches the critical size, it grows and relieves all the mechanical energy stored in the rest of the liquid. This single cavity can relieve all the negative pressure in the sphere by growing to a larger size, preventing any other cavities from forming as the rate of cavity formation is highly dependent on the negative pressure and temperature of the liquid [11].

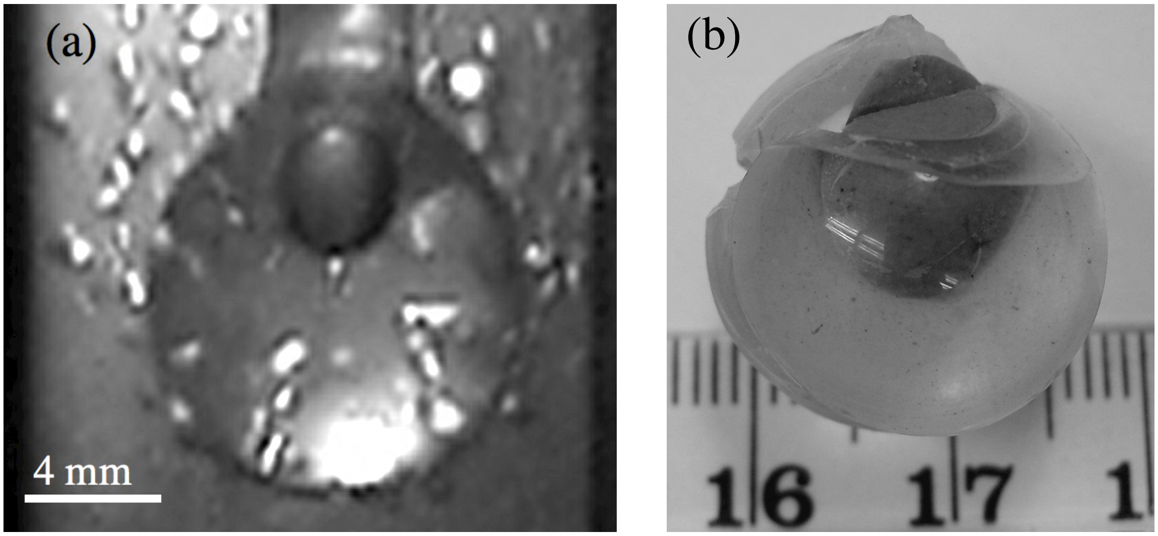

Figure 5.2 (a) An in situ picture of the molecular glass-former glycerol $C_3H_8O_3$ inside a fused silica ampule with a homogeneously nucleated cavity when quenched from room temperature 300 K into liquid nitrogen at 77 K. (b) A sphere of boron oxide B_2O_3 with a homogeneously nucleated cavity that has been filled with clay to elucidate the volume of the cavity inside the translucent boron oxide.

RESULTS AND DISCUSSION FOR $Zr_{41.2}Cu_{12.5}Ti_{13.8}Be_{22.5}Ni_{10}$

The well-studied family of Zr-based alloys relies on elements with a strong affinity for oxygen that will aggressively chemically react with a fused silica tube. This reaction creates a strong interphase layer of mixed intermetallics that act as a glue to hold the liquid to the surface of the fused silica. This allows for even heat transfer out of the shell of the sphere so that as much thermal strain as possible can be transferred to the hot liquid in the center of the sphere. The $Zr_{41.2}Cu_{12.5}Ti_{13.8}Be_{22.5}Ni_{10}$ (Vitreloy 1 or Vit1) liquid was always brought to at least an initial temperature of 1000 ºC to exceed the liquidus temperature of ~915 ºC. This high temperature was also necessary to lower the viscosity of the liquid enough to allow for complete filling of the fused silica ampule. An intermediate heat source was often used to change the temperature of the ampule before the quench. If the desired temperature was well above 580 ºC, the "nose" temperature of the time-temperature-transformation (TTT) diagram, a second furnace was sufficient to radiatively cool the sample to the new moderate temperature. However, for temperatures close to 580 ºC, it was necessary to utilize the rapid heat conduction provided by a tin bath to quickly equilibrate the ampule to the new temperature, typically 650 ºC or 700 ºC. The T_g of Vit1 is 345 ºC and was routinely quenched from 1000 ºC in to an ~80 °C quench bath of the fusible alloy Wood's metal. After quenching, the fused silica shell always spalls off the frozen Vit1 sphere by a mode II crack that propagates parallel to the quartz/glass interface, halfway through the thickness of the quartz. This left about a half millimeter of fused silica covering the glassy sphere, shown in the rough specular surface of the Vit1 sphere shown in figure 5.3. To facilitate more accurate measurements of the final sphere diameter, a dremel tool was used to mechanically remove any remaining quartz. After the density of the sphere is measured by the Archimedes technique, the sphere is sectioned with a 0.5 mm thick diamond impregnated blade. If there is a cavity, the cavity volume can be estimated with either graphical methods or by weighing the amount of clay (of a known density) it takes to fill the cavity. With both methods, one must remember to include the volume removed by the cut. If there is no cavity apparent on the cut surface, we check for other cavities in the sphere by measuring the density of both sphere halves to see if they are in agreement with each other and the original density of the entire sphere. We only witnessed cavities forming on the centerline of the top hemisphere, just like the cavities found in the molecular glass-formers.

Notice in figure 5.3 that the exterior of the sphere is particularly dark in color, especially when compared to the shiny exterior of the Pd-based glass, and is the intermetallic layer that kept the liquid wetted to the fused silica during the quenching. Unlike the molecular glass-formers, we observed heterogeneous nucleation of cavities in the Vit1 samples, such as the cross section of the sphere in figure 5.4. The heterogeneously nucleated cavity forms off the top wall of the fused silica container and then grows inward as the sphere cools. These cavities grow to a large volume of ~1% of the sphere volume. To contrast the heterogeneous formation of cavities, in figure 5.5 we present the cross sections of a sphere with a homogeneously nucleated cavity and a sphere without any cavities. Both spheres have a volume of approximately 0.75 cm^3, but were quenched from different temperatures. The sphere quenched from 1000 ºC cavitated homogeneously in the center of the sphere, and the sphere quenched from 700 ºC did not cavitate heterogeneously or homogeneously. The sphere quenched from 700 C avoided heterogeneous nucleation of cavities from the wall of the container, but did not have enough thermal volume strain to generate a negative pressure that exceeds the critical pressure for homogeneous cavitation at that temperature. Alternatively, it could be that the amount of time the negative pressure was applied was not long enough for a cavity to nucleate, as a liquid is always metastable at any negative pressure [11,15]. Now that all three types of experimental results have been presented, we will discuss the results of all the Vit1 cavitation experiments.

Figure 5.3 A representative example of $Zr_{41.2}Cu_{12.5}Ti_{13.8}Be_{22.5}Ni_{10}$ liquid after quenching in the fused silica container shown in figure 5.1(a). Fused silica remains attached to the dark-colored intermetallic on the exterior of the sphere formed by the chemical reaction between the Vit1 liquid and the fused silica container.

Figure 5.4 The cross section of the $Zr_{41.2}Cu_{12.5}Ti_{13.8}Be_{22.5}Ni_{10}$ sphere shown in figure 5.3, this sample was quenched from 650 ºC. A cavity formed during quenching but it appears to have nucleated heterogeneously at the top wall of the fused silica container near the neck of the ampule. As the interior liquid cooled, the cavity grew from the container wall toward the center of the sphere, resulting in a highly elongated cavity that is ~1% the volume of the sphere.

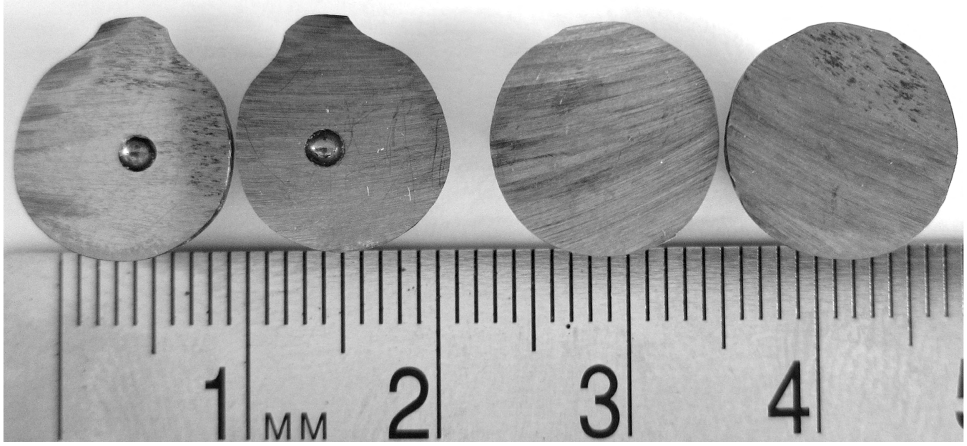

Figure 5.5 Cross-sectioned spheres of $Zr_{41.2}Cu_{12.5}Ti_{13.8}Be_{22.5}Ni_{10}$ liquid that were quenched in fused silica from different temperatures. Both spheres have a volume of ~0.75 cm^3. The sphere with the cavity was quenched from 1000 ºC, and the sphere with no cavity formation was quenched from 700 ºC. The central placement of the cavity in the sphere quenched from 1000 ºC and its uniform diameter suggest homogeneous cavitation of the liquid upon reaching a critical negative pressure on the order of seconds. The sphere quenched from 700 ºC supported some amount of negative pressure in its liquid during cooling, but the critical negative pressure for laboratory timescale homogeneous cavitation was not reached.

Table 5.1 contains the sphere volume, initial temperature T_o, ΔT (the difference between T_o and T_g, where T_g = ~345 ºC [16]), temperature-dependent bulk modulus $B(T_o)$ (estimated from the highly similar liquid $Zr_{46.75}Ti_{8.25}Cu_{7.5}Ni_{10}Be_{27.5}$ [17]), cavity nucleation type, and the cavity volume as the percentage of sphere volume for all of the Vit1 liquid cavitation experiments. We also include in table 5.1 our estimations of the maximum potential volume strain and maximum potential negative pressure. We call this the "maximum potential" because it relies on the assumption that the sphere quenches quasistatically and is fully encapsulated at the beginning of the quench (our samples require that the liquid inside the neck to the ampule solidify before negative pressure can build). This simple model also assumes that the container is infinitely rigid and would not contract in response to the negative pressure building in the center of the sphere. We note that the Young's modulus of glassy Vit1 is about 30 GPa greater than fused silica, so any solid Vit1 formed during the quench is a much stiffer container than the fused silica, reducing the overall compliance of the container. Between the delay in the freezing of the neck, the compliance of the solid shell, and the time-dependent development of negative pressure from volume contraction, the amount of negative pressure that is actually experienced by the liquid is some unknown percent of the quasistatically quenched upper bound. However, we do expect that as the sphere diameter increases, the time that it takes for the liquid inside the neck to solidify decreases as compared to the total quenching time.

The upper bound of thermal volume strain can be estimated from

$$\varepsilon_{\max} = \Delta\alpha_{l-(q,g)}\Delta T, \tag{1}$$

where $\Delta\alpha$ is the difference between the volume coefficient of thermal expansion of the Vit1 liquid $\alpha_l = 53 \cdot 10^{-6}\ K^{-1}$ [18] and the volume coefficient of thermal expansion of the solid container, which could either primarily be fused silica SiO_2 $\alpha_q = 1.5 \cdot 10^{-6}\ K^{-1}$ or glassy Vit1 $\alpha_g = 34 \cdot 10^{-6}\ K^{-1}$ [18]. Fused silica has a remarkably low α, if SiO_2 is the main container, it will act as a near constant volume container. The Vit1 shell would shrink considerably by comparison. From simple arithmetic we see that $\Delta\alpha_{l\text{-}q} \approx 51 \cdot 10^{-6}\ K^{-1}$ and

$\Delta\alpha_{\text{l-g}} \approx 19\cdot10^{-6}\ \text{K}^{-1}$. We calculate the upper bound of negative hydrostatic pressure $P_{\max}$ in a small amount of liquid that we assume remains at the initial temperature T_{o}, by

$$P_{\max(q,g)} = -B_{liq}(T_o)\varepsilon_{\max} = -B_{liq}(T_o)(\alpha_l - \alpha_g)(T_o - T_g)\,. \qquad (2)$$

We list these $P_{\max}$ values for both a Vit1 and SiO_2 shell in table 5.1. Figure 5.6 shows $P_{\max,g}$ vs. sphere volume for all the cavitation experiments. The blue crosses represent samples that cavitated heterogeneously, the red circles represent samples that cavitated homogeneously, and the green triangles represent samples that did not cavitate at all. The smallest spheres had a tendency to avoid heterogeneous nucleation, while the larger spheres all cavitated heterogeneously, regardless of their $P_{\max}$. To get a better understanding of how this happened we can inspect the ratio of the cavity volume to sphere volume ε_{cav}. The quantity ε_{cav} is the value of strain that is actually realized in the experiment by the cavity, so we can compare this realized strain ε_{cav} to $\varepsilon_{\max}$ for a Vit1 and SiO_2 shell. We express this quantity as a percentage in table 5.1; a quick look shows that the volume strain of the heterogeneously nucleated cavities ε_{cav} is generally 1%. This can also be seen in figure 5.7, where the sphere volume is plotted against the ratio of cavity volume to sphere volume. The 1% strain is almost 2 times larger than the maximum strain predicted from having a Vit1 shell, but only a little over half the strain predicted from a SiO_2 shell. Thus, it is impossible for a Vit1 glassy shell to have provided the containment of the liquid. Apparently, the liquid in the neck solidified too quickly for a glassy Vit1 shell to uniformly coat the inside the fused silica ampule. We see in both figure 5.6 and 5.7 that all of the heterogeneous cavitation occurred in the spheres with volumes larger than ~1 cm^3. It appears that as soon as the liquid in the neck solidified, the liquid supported only a small

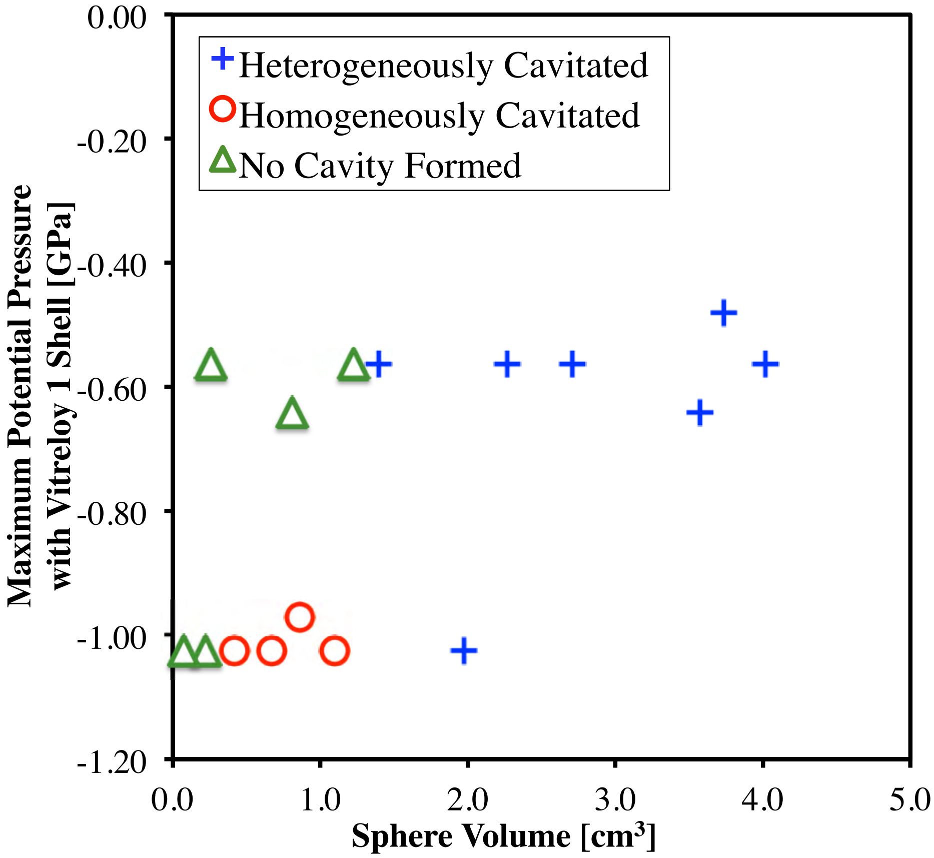

Figure 5.6 The maximum potential negative pressure that could be generated inside a sphere of liquid Vit1 if it was encapsulated inside an infinitely rigid container of glassy Vit1 and quenched quasistatically. This maximum negative pressure is estimated by $P_{\max,g} = -B_{liq}(T_o)(\alpha_l - \alpha_g)(T_o - T_g)$, where $B_{liq}(T_o)$ is the bulk modulus of the liquid at the initial temperature T_o, T_g is the glass transition temperature, α_l is the volume coefficient of thermal expansion of the liquid, and α_g is the volume coefficient of thermal expansion of the glass.

amount of negative pressure before a cavity would nucleate heterogeneously from the fused silica wall. From this point on, the fused silica sphere essentially acts as a rigid container during the remaining cooling of the liquid. The barrier to heterogeneous nucleation is lower than the barrier to homogeneous nucleation, and the rate of nucleation is higher for liquids at high temperatures, thus yielding cavities that form early and grow to be very large and highly elongated. This heterogeneous nucleation process is an important factor when considering metallic glasses as real world engineering materials. It is often possible for inclusions, amorphous or crystalline, to make their way in to the melt of a metallic glass and then be trapped in the glass during vitrification. If this same glass is then plastically deformed and has shear bands developing in the material, these inhomogeneities could act as heterogeneous nucleation sites for the formation of cavities inside the shear bands. This cavitation creates voids in the shear band that could then gather and open the shear band in to a crack, which limits the resistance to fracture of the material. Therefore, the careful control of impurities and inclusions in metallic glass will likely play a crucial role in ensuring the safety and reliability of metallic glass when it is used in an application where catastrophic failure must be avoided.

For spheres with volume strains of ~1% and lower, we observed zero heterogeneously nucleated cavities. A protective glassy shell of Vit1 must have covered the inside of the fused silica ampule before any significant negative pressure was generated in the liquid. This means that we lost some portion of our some thermal volume strain potential before the liquid was mechanically encapsulated. However, we still witnessed homogeneously nucleated cavities that were centrally located with uniform diameter cavities in four different experiments. The location and shape of these cavities leads us to believe that they nucleated homogeneously from the liquid after a critical pressure and waiting time was reached in the liquid. This cavitation rate is highly pressure- and temperature-dependent [11], but we unfortunately do not know what the exact temperature or pressure was when our Vit1 liquid cavitated. However, we do know that it nucleated homogeneously in a sample size of ~0.5 cm^3 to ~1 cm^3 on the order of 7 s. If we look at figure 5.6, we see that spheres below 0.4 cm^3 in volume with a P_{max} of 1 GPa did not cavitate at all. We also see that spheres of any volume with a P_{max} of ~0.6 GPa either did not cavitate or cavitated heterogeneously, which has a lower critical pressure than homogeneous cavitation. In particular, if you inspect the 0.75 cm^3 spheres of figure 5.5, they are of similar diameter but the one quenched from 1000 ºC cavitated homogeneously and the sphere quenched from 700 ºC did not. The sphere quenched from 700 ºC had to have some amount of negative pressure trapped in its frozen state as the entirety of its –0.6 GPa P_{max} could not have dissipated before the liquid was fully encapsulated. In addition, if we look back to figure 5.6 and inspect slightly larger spheres of ~1 cm^3 with a P_{max} of ~0.6 GPa (T_o ~650 ºC), there is a transition from no cavity to heterogeneous nucleation for two spheres that are similar in volume. Again, the sphere without a cavity must have supported some amount of negative pressure that contributed to the heterogeneous cavitation of the similarly sized sphere. Thus, we have established that the Vit1 liquid is "metastable" on laboratory timescales, temperatures, and negative pressures. At some critical negative pressure the liquid will decompose in to a Vit1 liquid and a cavity, but at some negative pressure that does not reach a critical value, the Vit1 liquid remains a single phase and solidifies into a cavity-free glass.

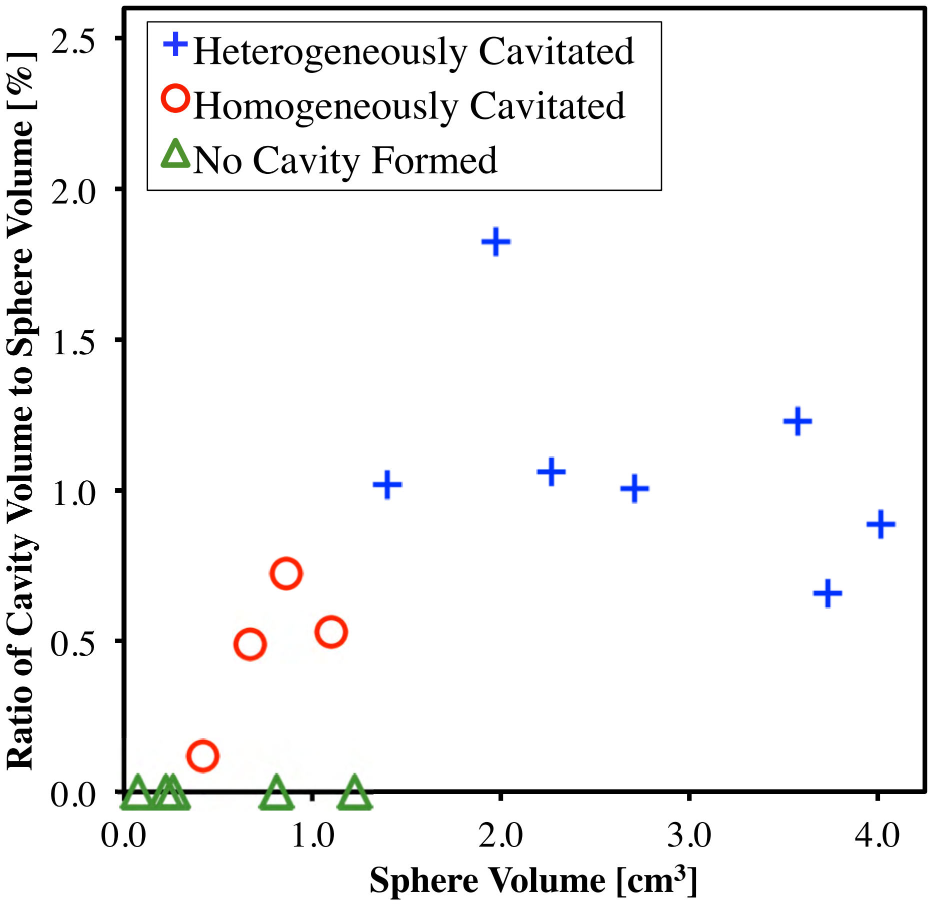

Figure 5.7 Cavity volume as a percentage of the sphere volume versus the sphere volume. Spheres with volumes much larger than 1 cm^3 always heterogeneously nucleated cavities from the wall of the fused silica container. These large volume spheres were unable to form a protective shell of glassy Vit1 on the inside of the fused silica container before significant negative pressure was generated in the liquid. The smaller diameter spheres with homogeneously nucleated cavities were able to grow a protective shell of glassy Vit1 before negative pressure was generated. This enabled the liquid to support a much greater amount of negative pressure upon subsequent cooling, as the barrier for homogeneous nucleation is higher than for heterogeneous nucleation.

To inspect the actual pressures more closely, we can use ε_{cav} to estimate the negative pressure P_{cav} that was present in the sphere at the point the cavity began to grow. We multiply this strain by the bulk modulus of appropriate temperature and estimate this strain as a negative pressure, listed in table 5.1 and overlaid on figure 5.8, the plot of ε_{cav} versus sphere volume. Note that we focus figure 5.8 on the experimental range that did not produce any heterogeneously nucleated cavities. The blue squares, red circle, purple diamond, and green triangles are the spheres quenched from 1000 ºC, 950 ºC, 700 ºC, and 650 ºC, respectively. Since none of these spheres cavitated heterogeneously, they were likely encapsulated in a glassy shell of Vit1. Because of this, the maximum negative pressure should be estimated with the assumption of a solid Vit1 shell, instead of a solid fused silica shell. The Vit1 solid shell P_{max} is shown in the legend of figure 5.8 for each T_o, it descends from –1.02 GPa to –0.56 GPa. All of the samples quenched from 700 ºC and below did not cavitate. All of the samples quenched from 950 ºC and above cavitated as long as the sphere volume was greater than 0.4 cm^3. The average P_{cav} for spheres that were larger than 0.5 cm^3 was roughly –500 MPa. A notable exception is the one sphere that was quenched from 1000 ºC with a P_{cav} of only –100 MPa. This sphere was the smallest sphere to cavitate at a volume of 0.42 cm^3. Since it had the same nominal starting temperature (same cavitation rate and critical pressure associated with that temperature) as its larger siblings, it is a curiosity that its cavity grew to be one fifth of their cavity sizes. This is probably due to the dynamic nature of the quenching in this experiment and represents a size, critical pressure, or time cutoff necessary for the nucleation and growth of a cavity. It is also possible that all of the cavities nucleated homogeneously at –100 MPa and then continued to grow because the larger spheres had extra thermal volume strain to continue cavity growth. If this is true it informs us that a sphere of 0.5 cm^3 to 1 cm^3 loses approximately –500 MPa of its equivalent thermal volume strain before the liquid is fully encapsulated. Thus, a 0.5 cm^3 to 1 cm^3 volume sphere with a P_{max} of –600 MPa might barely cross the critical negative pressure threshold of –100 MPa or it might solidify with the negative pressure as a residual stress. A detailed finite element model that included all the fine details of this experiment would be of great use in analyzing the negative pressures, temperatures, and timescales necessary to homogeneously nucleate cavities in the $Zr_{41.2}Cu_{12.5}Ti_{13.8}Be_{22.5}Ni_{10}$ liquid.

Table 5.1 Results summary for the cavitation experiments on the $Zr_{41.2}Cu_{12.5}Ti_{13.8}Be_{22.5}Ni_{10}$ (Vit1) liquid. The sphere volume, initial temperature T_o, ΔT (difference between T_o and T_g), estimated thermal volume strain for a Vit1 or fused silica shell, temperature-dependent bulk modulus of Vit1 B(T_o) [17], maximum potential negative pressure for a sphere with a Vit1 or fused silica shell, cavity nucleation type, cavity volume as the ratio of sphere volume, cavity strain as a percentage of the maximum thermal strain for a Vit1 or fused silica shell, and the negative pressure estimated from the volume strain of the cavity for every cavitation experiment of the Vit1 liquid.

Sphere Diameter [mm]	Sphere Volume [cm^3]	Initial Temperature (T_o) [°C]	ΔT (T_o-T_g) [°C]	Maximum Potential Volume Strain $\Delta T \cdot \Delta\alpha_{l\text{-}g}$ (Vit1 shell) [–]	Maximum Potential Volume Strain $\Delta T \cdot \Delta\alpha_{l\text{-}q}$ (SiO_2 shell) [–]	Vit1 Bulk Modulus at T_o, B(T_o) [GPa]	Maximum Potential Pressure with a Vit1 Shell [GPa]	Maximum Potential Pressure with a Fused Silica Shell [GPa]	Cavity Nucleation Type	Cavity Volume as Ratio of Sphere Volume [%]	Potential Strain Realized in Cavity with Vit1 Shell [%]	Potential Strain Realized in Cavity with Fused Silica Shell [%]	Pressure from Cavity Volume Strain Ratio (P_{cav}) [GPa]
19.3	3.74	600	255	0.005	0.013	99.2	-0.48	-1.30	Heterogeneous	0.66	139	51	0.67
13.9	1.40	650	305	0.006	0.016	97.1	-0.56	-1.53	Heterogeneous	1.02	178	66	1.00
16.3	2.27	650	305	0.006	0.016	97.1	-0.56	-1.53	Heterogeneous	1.06	186	69	1.05
17.3	2.71	650	305	0.006	0.016	97.1	-0.56	-1.53	Heterogeneous	1.01	177	65	1.00
19.7	4.02	650	305	0.006	0.016	97.1	-0.56	-1.53	Heterogeneous	0.89	156	58	0.88
19.0	3.57	700	355	0.007	0.018	95.0	-0.64	-1.74	Heterogeneous	1.23	185	68	1.19
15.6	1.97	1000	655	0.012	0.034	82.4	-1.02	-2.78	Heterogeneous	1.82	145	53	1.49
11.6	0.81	700	355	0.007	0.018	95.0	-0.64	-1.74	None	0	0	0	0
7.9	0.26	650	305	0.006	0.016	97.1	-0.56	-1.53	None	0	0	0	0
13.3	1.23	650	305	0.006	0.016	97.1	-0.56	-1.53	None	0	0	0	0
7.5	0.22	1000	655	0.012	0.034	82.4	-1.02	-2.78	None	0	0	0	0
5.2	0.07	1000	655	0.012	0.034	82.4	-1.02	-2.78	None	0	0	0	0
10.9	0.67	1000	655	0.012	0.034	82.4	-1.02	-2.78	Homogeneous	0.49	41	15	0.42
12.8	1.10	1000	655	0.012	0.034	82.4	-1.02	-2.78	Homogeneous	0.53	43	16	0.44
9.3	0.42	1000	655	0.012	0.034	82.4	-1.02	-2.78	Homogeneous	0.12	10	4	0.10
11.8	0.86	950	605	0.011	0.031	84.5	-0.97	-2.63	Homogeneous	0.72	63	23	0.62

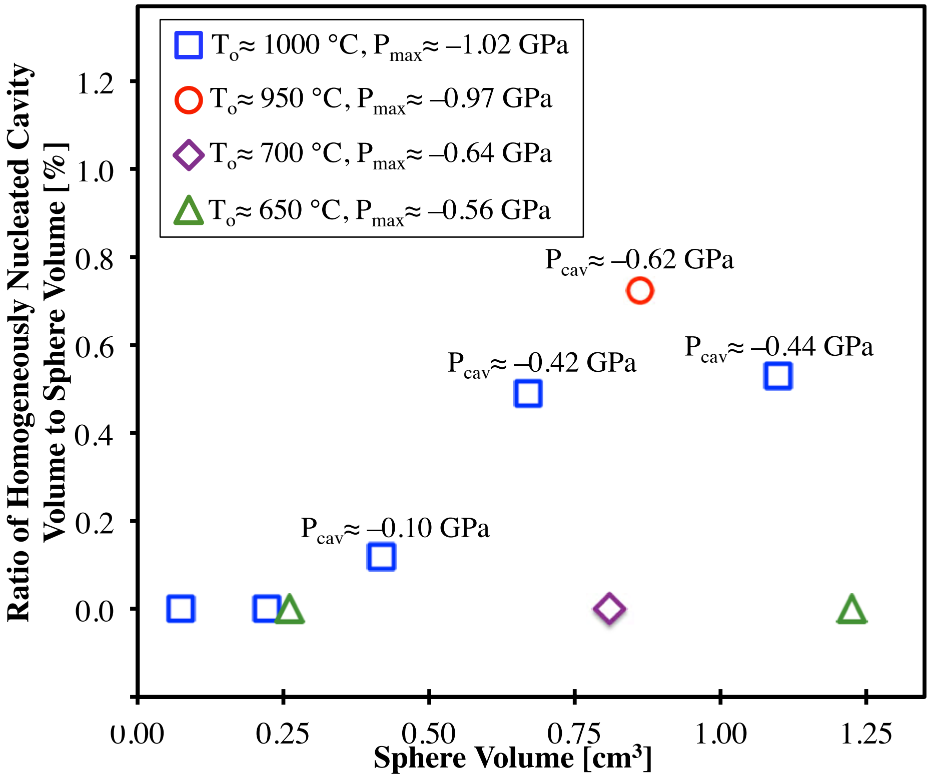

Figure 5.8 The volume strain of the homogeneously nucleated cavities vs. the sphere volume. The blue squares, red circle, purple diamond, and green triangles are the spheres quenched from $T_o = 1000$ ºC, 950 ºC, 700 ºC, and 650 ºC, respectively. The maximum negative pressure P_{max} that can be achieved inside an infinitely rigid shell of Vit1 glass is shown in the legend for each T_o. For the spheres that did cavitate, the pressure in the sphere at the point of cavitation P_{cav} is estimated from the volume strain of the cavity ε_{cav} and is displayed next to the markers. No sphere quenched from ~700 ºC or with a volume smaller than 0.4 cm^3 formed cavities. The spheres that did homogeneously cavitate had –100 to –600 MPa of available thermal volume strain in the sphere. The smallest value, –100 MPa may represent the critical cavitation pressure of the Vit1 liquid at 1000 ºC on the laboratory timescale of 1 to 7 s.

Preliminary results from the Vit1 experiments were used by An, Garrett, et al. [11] to provide a real, even if tenuous, experimental underpinning to the determination of the MD cavitation rate in a CuZr liquid. The MD simulations showed that cavitation in the liquid is a stochastic waiting process characterized by Poisson statistics. The 54,000 atom system cavitated with a mean waiting time of 97 ps for a pressure of –3.16 GPa and temperature of 1200 K. The waiting time was then determined at three different pressures also at 1200 K. When the waiting time vs. negative pressure was fit quadratically, we found that at laboratory timescale of 7 s and system size of 10^{22} atoms we extrapolated that would occur at –500 MPa. This is a very reasonable prediction that is supported by the current experimental results, especially given the 27 orders of magnitude covered by the extrapolation.

In conclusion, we used the experimental data combined with simple analytic modeling to estimate the critical pressure for cavitation as a function of temperature in liquid Vit1. We estimate that centimeter diameter spheres of Vit1 at ~1000 ºC homogeneously cavitate with less than –500 MPa of pressure at laboratory timescales of 1 to 7 s. We also find that cavitation does not occur in a ~700ºC Vit1 liquid with a laboratory timescale of 1 to 7 s and some fraction of the –500 MPa pressure that caused cavitation in the ~1000 ºC liquid. The Vit1 liquid is thus “metastable” on laboratory timescales with respect to cavitation at these temperatures and estimated negative pressures. Heterogeneous nucleation was promoted whenever liquid Vit1 is subjected to negative pressures while in contact with fused silica, an important consideration as this shortcut to cavitation could severely limit the damage tolerance of metallic glasses.

BIBLIOGRAPHY

[1] M. D. Demetriou, M. E. Launey, G. Garrett, J. P. Schramm, D. C. Hofmann, W. L. Johnson, and R. O. Ritchie, Nat Mater **10**, 123 (2011).

[2] M. E. Launey, D. C. Hofmann, J. Y. Suh, H. Kozachkov, W. L. Johnson, and R. O. Ritchie, Appl Phys Lett **94**, 241910 (2009).

[3] R. O. Ritchie, Nat Mater **10**, 817 (2011).

[4] J. J. Lewandowski, W. H. Wang, and A. L. Greer, Philosophical Magazine Letters **85**, 77 (2005).

[5] E. Bouchaud, D. Boivin, J. L. Pouchou, D. Bonamy, B. Poon, and G. Ravichandran, Epl-Europhys Lett **83**, (2008).

[6] J. Suh, R. Conner, C. Kim, and M. Demetriou, in *Proceedings of the SEM Annual Conference* (2009).

[7] J. J. Lewandowski and A. L. Greer, Nat Mater **5**, 15 (2005).

[8] W. L. Johnson, M. D. Demetriou, J. S. Harmon, M. L. Lind, and K. Samwer, Mrs Bull **32**, 644 (2007).

[9] C. E. Brennen, *Cavitation and Bubble Dynamics* (Oxford University Press, New York, 1995).

[10] G. Duan, Simulations, Modeling, and Designs of Bulk Metallic Glasses, California Institute of Technology, 2008.

[11] Q. An, G. Garrett, K. Samwer, Y. Liu, S. V. Zybin, S.-N. Luo, M. D. Demetriou, W. L. Johnson, and W. A. Goddard, J Phys Chem Lett **2**, 1320 (2012).

[12] P. Murali, T. Guo, Y. Zhang, R. Narasimhan, Y. Li, and H. Gao, Phys Rev Lett **107**, (2011).

[13] M. L. Lind, Ultrasonic Investigation of the Elastic Properties and Liquid Fragility of Bulk Metallic Glasses in the Supercooled Liquid Region, California Institute of Technology, 2008.

[14] M. Bertholet, Ann. Chim. Phys. **30**, 232 (1850).

[15] A. R. Imre, AIP Conf. Proc. **1349**, 33 (2011).

[16] W. Johnson and K. Samwer, Phys Rev Lett **95**, 195501 (2005).

[17] M. L. Lind, G. Duan, and W. L. Johnson, Phys Rev Lett **97**, 015501 (2006).

[18] K. Ohsaka, S. K. Chung, W. K. Rhim, A. Peker, D. Scruggs, and W. L. Johnson, Appl Phys Lett **70**, 726 (1997).

Chapter 6

SUMMARY AND FUTURE DIRECTIONS

SUMMARY

This thesis has attempted to elucidate the origins of toughness in bulk metallic glass from a few different angles, reflected in the titles of its four subject chapters: an exceptionally damage-tolerant glass, influence of configurational disorder on the intrinsic fracture toughness of metallic glasses, the dependence of fracture toughness on the configurational state of metallic glass, effect of microalloying on the toughness of metallic glass, and investigation of cavitation in glass-forming liquids. The multiple approaches taken were a necessity, as we do not have the knowledge to perfectly explain any of the fracture toughness phenomena that we have observed. The common thread between the chapters is the fundamental competition between the mechanisms of shear banding/toughening and cavitation/cracking. We hope that this central issue and the physical observations surrounding it in this thesis serve as experimental guideposts for the research to follow. It is clear that we still have much more to learn about this interesting class of materials. We will discuss some of the open questions of toughness in the future directions section that follows, but will continue here to summarize the main findings of this thesis.

In chapter 2, an exceptionally damage tolerant glass, we introduce a Pd-based glass that displays a level of damage tolerance, the combination of strength and toughness, that is unprecedented for monolithic bulk metallic glass and is in fact one of the most damage tolerant materials known. From observing the fracture of this very tough glass we see the intrinsic mechanisms of toughening at work: shielding and blunting of the crack tip by extensive shear banding, crack deflection, and perhaps interactions between shear bands ahead of the crack tip. The intrinsic toughening mechanisms allow for this alloy to tolerate significant stable growth of a subcritical crack, and exhibit a rising R-curve, a phenomenon not seen in any monolithic metallic glass at that time. The majority of monolithic bulk metallic glasses fail catastrophically as soon as a crack is initiated, which we believe is due to cavitation in the sliding shear bands ahead of the crack tip. We also note that the measurement of this tough glass was enabled only through the employment of nonlinear fracture mechanics, specifically the crack-tip opening displacement method. This technique will be critical in metallic glass fracture toughness as it may be impossible to form any of these tough glasses at thicknesses large enough to satisfy linear-elastic fracture mechanics specimen size constraints.

In chapter 3 we explore the fracture toughness of a moderately tough Zr-based glass by linear-elastic fracture mechanics, in hopes of establishing a valid K_{Ic} for the material. Our results were surprising, and not simple to interpret. We found that the frequency- and temperature-dependent relaxation modes of a dynamically vitrifying glass cannot be ignored as part of the processing history of the glass. If the glass is relaxed to an equilibrium well-defined configurational state, we find that the fracture toughness is consistent and correlates strongly with the average configurational properties of the glass, such as the shear modulus G. For as-quenched specimens, with a complex configurational state consisting of a broad spectrum of unrelaxed modes and thus more configurational disorder, they exhibit a large variance in their fracture toughness that cannot be correlated with the measured average configurational properties of the glass. This implies that the fracture process of a specimen with an atomically sharp crack tip is a local process that is sensitive to the local configurational environment of the crack tip. Relaxing the configurational modes of the glass reduces the variability in fracture toughness by reducing the configurational disorder at the crack tip.

In chapter 4 we investigate the effect of minor alloying additions (≤2%) on the configurational state and notch toughness of a Cu-based glass. In the previous chapter we manipulated the configurational state of the glass through its processing history, but in this chapter we take a close look at the how changing the chemical composition of the glass affects toughness. The same general trend of toughness correlating with the shear modulus is found to hold for minor additions of substitute elements. In fact, the combination of minor additions and tightly controlled processing could be used to fine-tune the absolute value and variance in the fracture toughness of metallic glass.

In chapter 5 we present a study on the nucleation of cavities in glass-forming liquids due to the dynamic application of negative hydrostatic pressure. This work was born out of the desire to understand the mechanism that competes with shear banding to limit the toughness of metallic glass, the cavitation (or opening) of the liquid inside a shear band into a crack. Shear banding during mode I fracture toughness tests is abundantly clear, but the only proof of a cavitation mechanism is seen in the veined and dimpled patterns seen on the fracture surfaces after failure [1]. If we could measure the barrier to cavitation in a glass-forming liquid, perhaps it would correlate strongly with fracture toughness. We found that a variety of glass-forming liquids are all metastable to negative pressure on laboratory timescales. Cavities can nucleate heterogeneously in the liquid at low negative pressures, or homogeneously at greater negatives pressures. The heterogeneous nucleation of cavities from trapped inclusions in the glass could play an important role in limiting fracture toughness. Ultimately, we found that Vitreloy 1 liquid is metastable on laboratory timescales at negative pressures, and nucleates homogeneously on laboratory timescales at pressures of –100 to –500 MPa.

Essentially, the fracture toughness of metallic glass shows a strong dependence on its composition and processing history, a complex blend of issues. If that wasn't enough to worry about, one cannot ignore the influence of any inhomogeneities in the production of the glassy samples. Shrinkage cavities, entrained gas bubbles, atmosphere contaminants, and hard inclusions are a sure shortcut to brittle, inaccurate results. The successful commercialization of metallic glasses will depend on accurately controlling for all of these factors, and those that are yet to be discovered.

FUTURE DIRECTIONS

The direction of future research on the toughness of bulk metallic glass should aim for a description of toughness that successfully incorporates both the toughest and most brittle metallic glasses, as well as the composition and processing history effects observed in the previous chapters. At this point we have a general understanding of some of the factors that can increase or decrease toughness, but we cannot accurately predict the toughness of any given alloy. We show in chapter 2 that the fracture toughness of an alloy can be related to the ratio of B to G and T_g, and that it may be a better way to correlate the toughness than the Poisson ratio. However, in chapter 3 we present results for an as-quenched Zr-based glass where the Poisson ratio cannot explain the measured toughness. Just within the past year, a Zr-Cu-Al-Ti glass with a modest Poisson ratio of ~0.37 was found to exhibit a rising R-curve [2], like the ~0.42 Poisson ratio Pd-based glass of chapter 2 [3]. Clearly, the entire story of toughness cannot be contained in the macroscopic average of the elastic constants of the glass. We have proposed that there is sensitivity to the local configurational makeup at the point of the crack tip, but this doesn't directly address why a particular composition of metallic glass can have such an unprecedentedly large toughness, no matter what the Poisson ratio is. At this point, two monolithic bulk metallic glasses have the ability to prevent a catastrophic stress instability at the crack tip until a toughness of ~150 $\text{MPa}\cdot\text{m}^{1/2}$ is achieved. How is it that the shear bands in these two glasses grow and multiply with impunity while the liquid inside those shear bands experiences an opening force that would cause cavitation and crack growth in the vast majority of metallic glasses? These two glasses have an amazing insensitivity to flaws and configurational disorder, they easily shield any stress concentrators and do not display the large variation in toughness seen in the Zr-based glass of chapter 3. There is no particular descriptor of these two glasses that one could look at and predict their extreme toughness, yet they are incredibly tough.

Additionally, we showed in chapter 3 that the toughness of a glass relaxed to an equilibrium configurational state correlates strongly with the configurational enthalpy of that state. If this is carried to its logical conclusion, what is the limit of toughness in metallic glasses? Could it be determined solely by the amount of configurational enthalpy that can be stored in the glass? How much configurational enthalpy can even be successfully stored in a metallic glass such that it provides useful shear banding during fracture? Under these circumstances perhaps the barrier to cavitation and cracking will limit the upper bound of toughness, as opposed to the shear flow barrier. The work by Bouchaud et al. [1] shows the characteristic patterns of cavitation in the failure of metallic glass, and the recent molecular dynamics work in metallic glass-forming liquids by An et al. [4] and Murali et al. [5] show cavitation in action. Chapter 5 highlights the difficulty of studying cavitation directly in the laboratory, but we likely have a lot more to learn about cavitation that could be very helpful in understanding the variety of observed phenomena in metallic glass fracture toughness.

We have proposed that the toughness of a glass is dependent upon the local configurational disorder at the crack tip of a precracked specimen. If this proposal is true, we have not yet discussed an important consequence. When can one trust that their measurement of an as-quenched sample is the true intrinsic fracture toughness of the glass? Should we be discussing fracture toughness as more of a statistical quantity? Perhaps, one can only trust a measurement when the glass is relaxed to a well-defined configurational state at a known temperature. However, it is possible that the effect of configurational disorder only dominates the results for samples with sharp cracks; notched samples like those of chapter 4 could be exempt as the stress is distributed over a much larger volume and the crack must still be initiated. Recent computational works by Rycroft and Bouchbinder [6,7] have explored how the configurational modes of metallic glass can affect the fracture toughness. We hope that a carefully selected combination of modeling and experiments will eventually reveal the origins and determination of fracture toughness in metallic glasses.

BIBLIOGRAPHY

[1] E. Bouchaud, D. Boivin, J. L. Pouchou, D. Bonamy, B. Poon, and G. Ravichandran, Epl-Europhys Lett **83**, (2008).

[2] Q. He, J. K. Shang, E. Ma, and J. Xu, Acta Mater **60**, 4940 (2012).

[3] M. D. Demetriou, M. E. Launey, G. Garrett, J. P. Schramm, D. C. Hofmann, W. L. Johnson, and R. O. Ritchie, Nat Mater **10**, 123 (2011).

[4] Q. An, G. Garrett, K. Samwer, Y. Liu, S. V. Zybin, S.-N. Luo, M. D. Demetriou, W. L. Johnson, and W. A. Goddard, J Phys Chem Lett **2**, 1320 (2012).

[5] P. Murali, T. Guo, Y. Zhang, R. Narasimhan, Y. Li, and H. Gao, Phys Rev Lett **107**, (2011).

[6] C. Rycroft and E. Bouchbinder, Phys Rev Lett **109**, 194301 (2012).

[7] C. H. Rycroft and E. Bouchbinder, Pre-Print arXiv:1207.4216v1 (2012).

Appendix A

DEBYE-GRÜNEISEN THERMAL EXPANSION EFFECT OF $Zr_{35}Ti_{30}Cu_{8.25}Be_{26.75}$

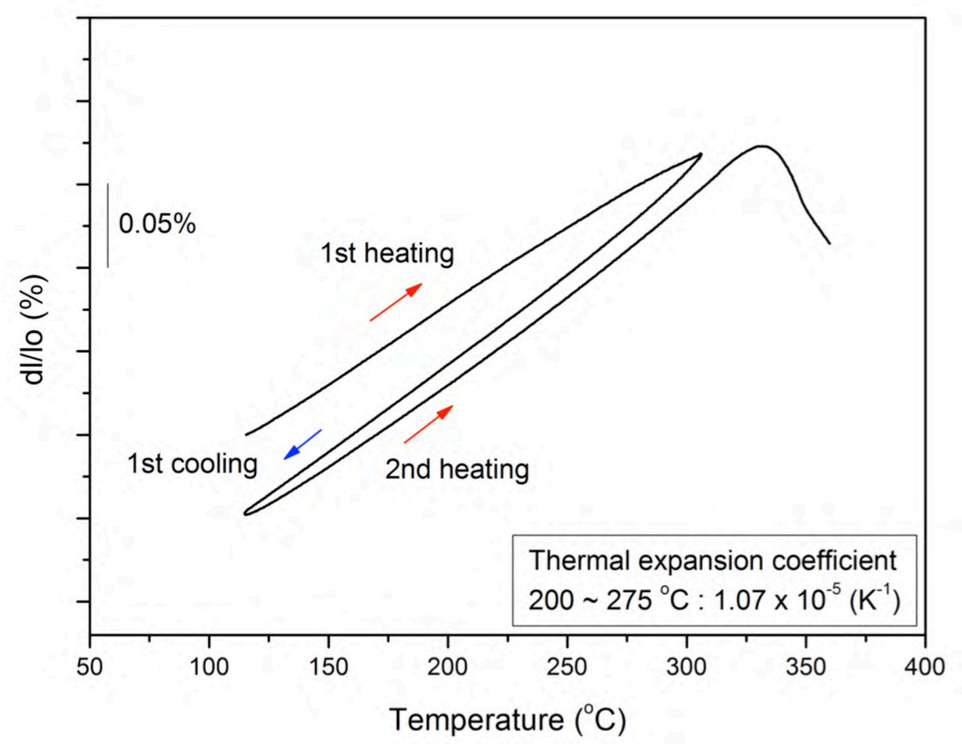

Figure A.1 The linear coefficient of thermal expansion α_{lin} of $Zr_{35}Ti_{30}Cu_{8.25}Be_{26.75}$ was determined to be 1.07×10^{-5} K^{-1} between 200 °C and 275 °C using a Perkin Elmer thermomechanical analyzer. The volumetric coefficient of thermal expansion α_{vol} is equal to $3 \cdot \alpha_{lin}$, which is 3.21×10^{-5} K^{-1}. We use α_{vol}, which is basically the change in the volume of the glass with change in temperature, to calculate a temperature-dependent density for the glass. This $\rho(T)$ is used in the calculation of the temperature-dependent elastic modulii, shown in figures A.2 and A.3. The change in density is small but gives a more accurate description of the change in vibrational modes with temperature.

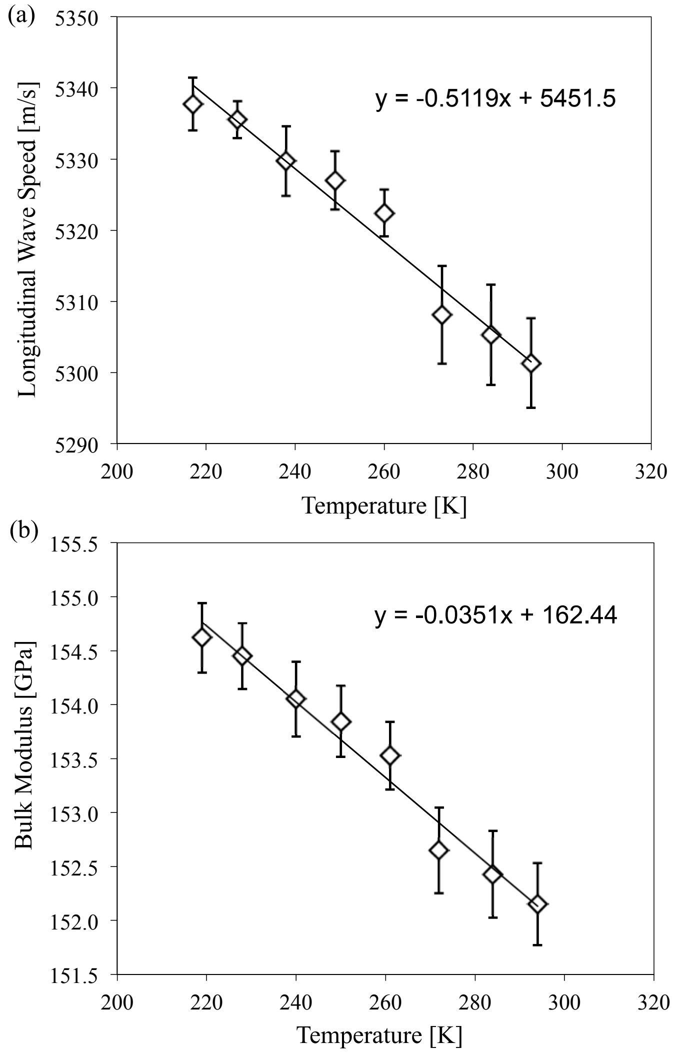

Figure A.2 The longitudinal wave speed (a) of $Zr_{35}Ti_{30}Cu_{8.25}Be_{26.75}$ was measured in-situ using a 25 MHz ultrasonic transducer with a long quartz delay line. The sample was cooled using a mixture of dry ice and ethanol between the temperatures of 220 K and 295 K. The bulk modulus (b) was calculated from the longitudinal wave speed and $\rho(T)$. The vibrational change in B with temperature for $Zr_{35}Ti_{30}Cu_{8.25}Be_{26.75}$ glass is –35.1 $\text{MPa}\cdot\text{K}^{-1}$, and the configurational change in G with temperature determined by ex-situ annealing in chapter 3 is –5.9 $\text{MPa}\cdot\text{K}^{-1}$. Thus, the Debye-Grüneisen corrected configurational change in B with T is –41.0 $\text{MPa}\cdot\text{K}^{-1}$.

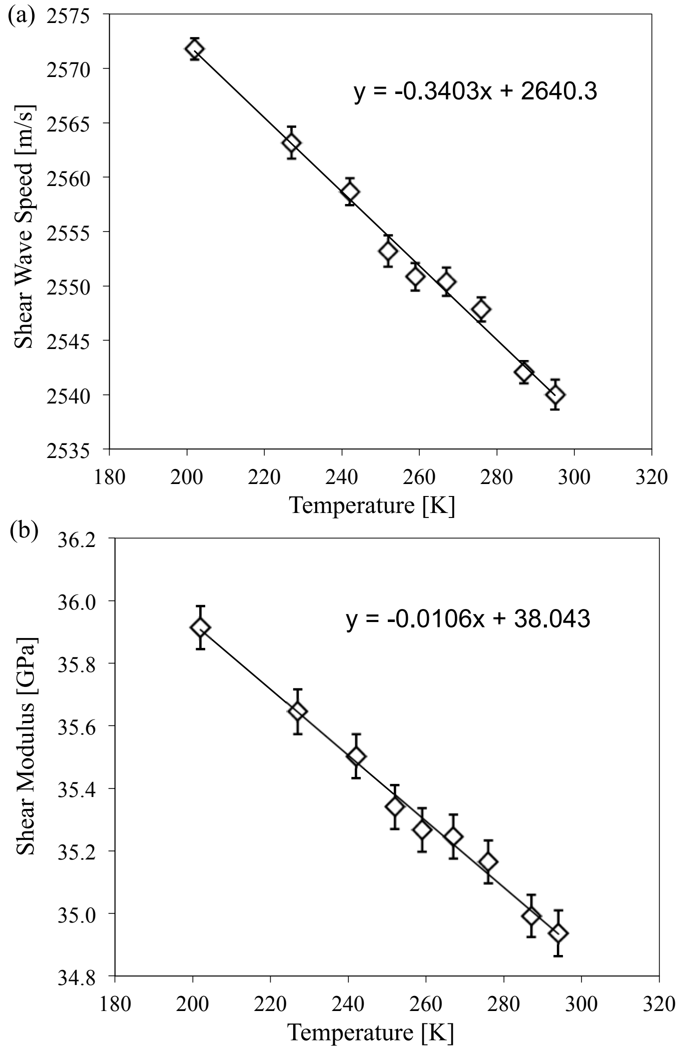

Figure A.3 The shear wave speed (a) of $Zr_{35}Ti_{30}Cu_{8.25}Be_{26.75}$ was measured in-situ using a 25 MHz ultrasonic transducer with a long quartz delay line. The sample was cooled using a mixture of dry ice and ethanol between the temperatures of 220 K and 295 K, liquid nitrogen was used for the measurement at 200 K. The shear modulus (b) was calculated from the shear wave speed and $\rho(T)$. The vibrational change in G with temperature for $Zr_{35}Ti_{30}Cu_{8.25}Be_{26.75}$ glass is –10.6 MPa·K^{-}1, and the configurational change in G with temperature determined by ex-situ annealing in chapter 3 is –23.1 MPa·K^{-1}. Thus, the Debye-Grüneisen corrected configurational change in G with T is –33.7 MPa·K^{-1}.

Appendix B

BULK MODULUS, POISSON RATIO, AND FRACTURE TOUGHNESS OF $Zr_{35}Ti_{30}Cu_{8.25}Be_{26.75}$

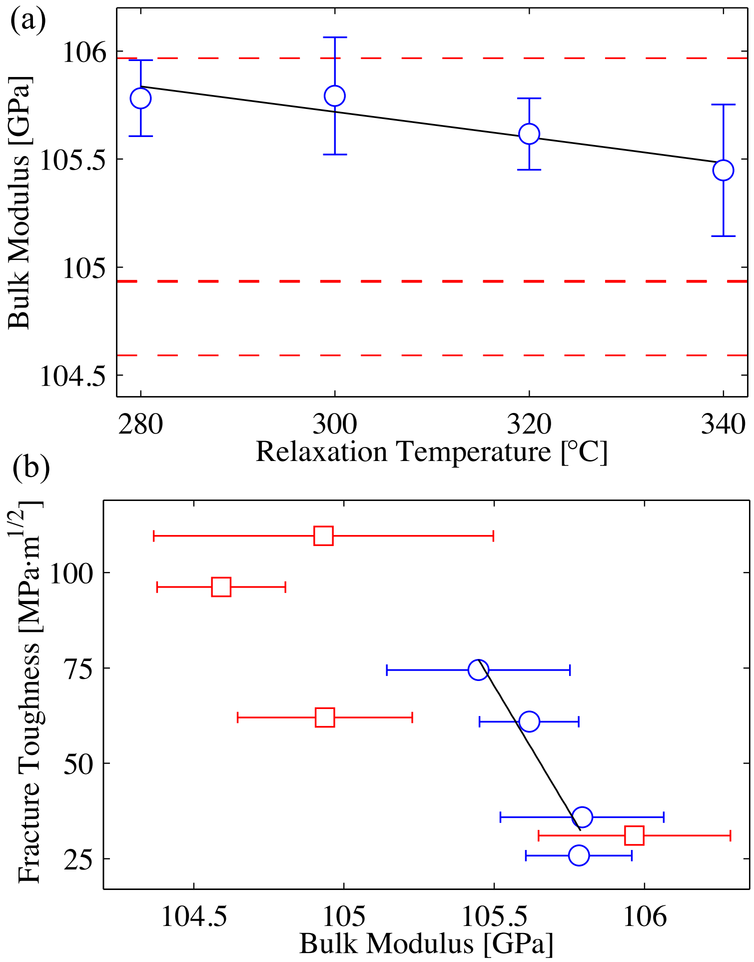

Figure B.1 The bulk modulus of the $Zr_{35}Ti_{30}Cu_{8.25}Be_{26.75}$ fracture toughness specimens is plotted against the (a) relaxation temperature and the (b) fracture toughness. The red dashed lines in (a) are the *B* values for the as-quenched samples and the blue circles are for the relaxed samples. The linear fit to *B* vs. T_R for the relaxed samples is –5.9 MPa·K^{-1}. The red squares in (b) are for the as-quenched samples and the blue circles are for the relaxed samples. The linear fit to K_Q vs. B for the relaxed samples is –132 MPa·m$^{1/2}$·GPa^{-1}, but we must note that the error bars for all of the B measurements are quite large compared to the change in B seen between samples.

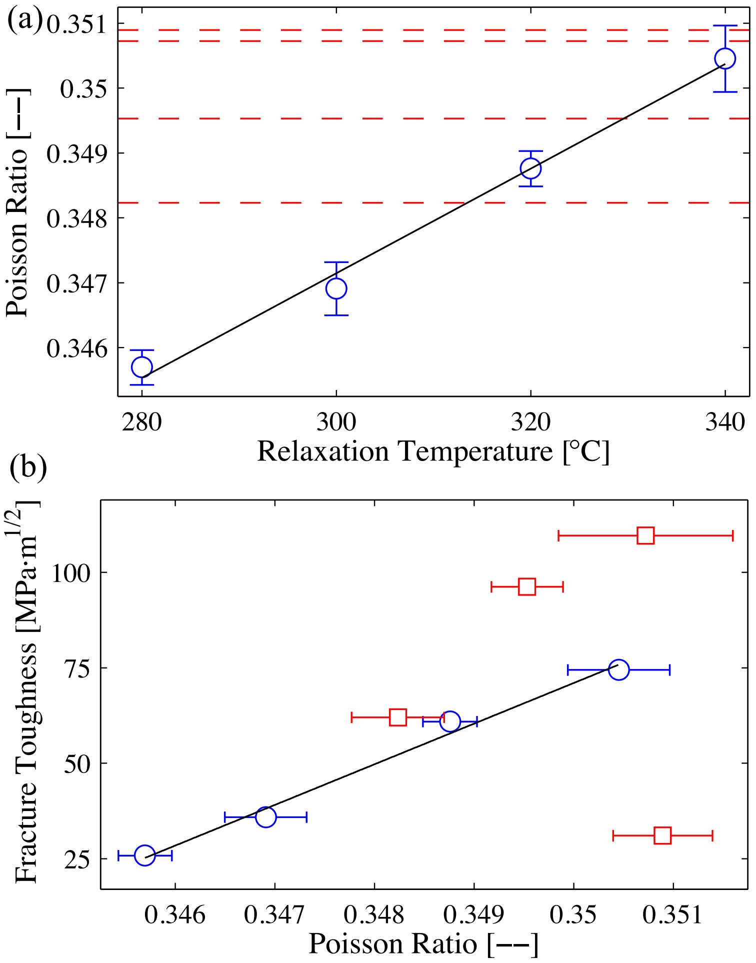

Figure B.2 The Poisson ratio of the $Zr_{35}Ti_{30}Cu_{8.25}Be_{26.75}$ fracture toughness specimens is plotted against the (a) relaxation temperature and the (b) fracture toughness. The red dashed lines in (a) are the υ values for the as-quenched samples and the blue circles are for the relaxed samples. The linear fit to υ vs. T_R for the relaxed samples is 0.000081 K^{-1}. The red squares in (b) are for the as-quenched samples and the blue circles are for the relaxed samples. The linear fit to K_Q vs. υ for the relaxed samples is 10,644 MPa·m$^{1/2}$, which is easier to understand as a 10.6 MPa·m$^{1/2}$ improvement in toughness for every 0.001 the Poisson ratio is raised. This 0.001 increase in the Poisson ratio corresponds to an increase in the relaxation temperature of 12.3 K, and if we compare this to the fracture toughness we see that for every 10 K the relaxation temperature is increased we raise the fracture toughness by 8.6 MPa·m$^{1/2}$.

Appendix C

DETERMINATION OF ENTHALPY RECOVERY BY DIFFERENTIAL SCANNING CALORIMETRY FOR $Zr_{35}Ti_{30}Cu_{8.25}Be_{26.75}$

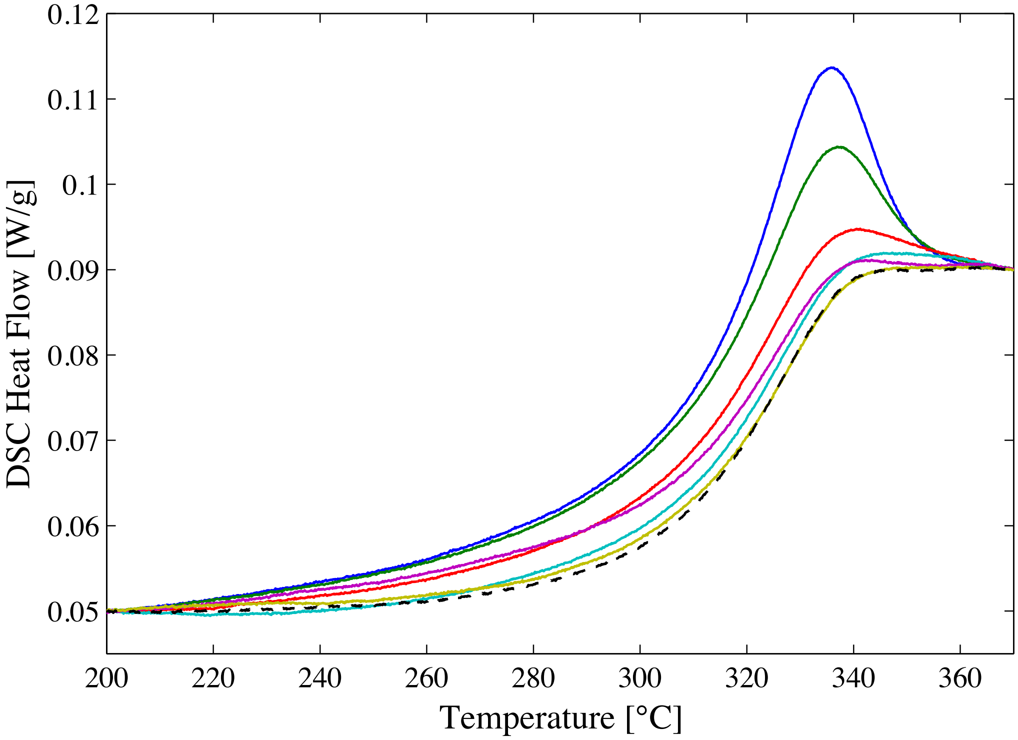

Figure C.1 The differential scanning calorimetry (DSC) scans for all of the fracture toughness specimens are shown above. The scans were performed using a Netzsch 404C calorimeter at a scan rate of 0.16 °C·s^{-1}. Each scan was performed with a baseline and sapphire standard, but the heat capacity of the low temperature glass and liquid above T_g do not line up perfectly for every run. A linear fit was used between 200 °C and 370 °C to normalize the data for comparison. The recovered enthalpies were calculated by integrating each DSC scan between 200 °C and 370 °C, dividing that integral quantity by the heating rate and molar mass to obtain a J/mol quantity. The recovered enthalpies were then subtracted by the sample that displayed the lowest recovered enthalpy (black dashed line) so that just the relative differences in the recovered enthalpy remain. The resulting ΔH values are listed in table 3.1 and shown vs. relaxation temperature in figure 3.1(b). The samples relaxed to 280 °C (blue line) and 300 °C (green line) have the greatest enthalpy recovered upon passing through T_g, and thus are easily spotted as the scans with tall peaks at ~330 °C in the figure above.